

AD-A247 554



2

PL-TR-91-2206

E 200 902

INVESTIGATION OF RING CURRENT / STORM DYNAMICS

H. L. Collin
J. B. Cladis
J. M. Quinn

Lockheed Palo Alto Research Laboratory
Space Sciences Laboratory
3251 Hanover Street
Palo Alto, CA 94304-1191

August 31 1991

reproduced in color
and in black and
white

Scientific Report No. 1

Approved for public release; distribution unlimited

DTIC
ELECTE
FEB 24 1992
S B D




PHILLIPS LABORATORY
AIR FORCE SYSTEMS COMMAND
HANSCom AIR FORCE BASE, MASSACHUSETTS 01731-5000

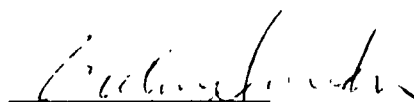
92-04155



"This technical report has been reviewed and is approved for publication"


MICHAEL D. VIOLET, LT, USAF
Contract Manager


E. G. MULLEN
Branch Chief


WILLIAM SWIDER
Deputy Director

This document has been reviewed by the ESD Public Affairs Office (PA) and is releasable to the National Technical Information Service (NTIS).

Qualified requestors may obtain additional copies from the Defense Technical Information Center. All others should apply to the National Technical Information Service.

If your address has changed, or if you wish to be removed from the mailing list, or if the addressee is no longer employed by your organization, please notify GL/IMA, Hanscom AFB, MA 01731. This will assist us in maintaining a current mailing list.

Do not return copies of this report unless contractual obligations or notices on a specific document requires that it be returned.

REPORT DOCUMENTATION PAGE			Form Approved OMB No 0704-0188	
Public reporting burden for this collection of information is estimated to average 1 hour per response, including the time for reviewing instructions, searching existing data sources, gathering and maintaining the data needed, and completing and reviewing the collection of information. Send comments regarding this burden estimate or any other aspect of this collection of information, including suggestions for reducing this burden, to Washington Headquarters Services, Directorate for Information Operations and Reports, 1215 Jefferson Davis Highway, Suite 1204, Arlington, VA 22202-4302, and to the Office of Management and Budget, Paperwork Reduction Project (0704-0188), Washington, DC 20503.				
1. AGENCY USE ONLY (Leave blank)	2. REPORT DATE 8/31/91	3. REPORT TYPE AND DATES COVERED Scientific No. 1		
4. TITLE AND SUBTITLE Investigation of Ring Current/Storm Dynamics		5. FUNDING NUMBERS F19628-90-C-0119 PE62101F PR7601 TA22 WVLC		
6. AUTHOR(S) H.L. Collin, J.B. Cladis, J.M. Quinn				
7. PERFORMING ORGANIZATION NAME(S) AND ADDRESS(ES) Lockheed Palo Alto Research Laboratory Space Sciences Laboratory 3251 Hanover Street Palo Alto, CA 94304-1191		8. PERFORMING ORGANIZATION REPORT NUMBER		
9. SPONSORING/MONITORING AGENCY NAME(S) AND ADDRESS(ES) Phillips Laboratory Hanscom AFB, MA 01731-5000 Contract Manager: Michael Violet Lt, USAF/PHP		10. SPONSORING/MONITORING AGENCY REPORT NUMBER PL-TR-91-2206		
11. SUPPLEMENTARY NOTES				
12a. DISTRIBUTION / AVAILABILITY STATEMENT Approved for public release; distribution unlimited			12b. DISTRIBUTION CODE	
13. ABSTRACT (Maximum 200 words) This report outlines the achievements of the first year of work on data acquired by the Lockheed Ion Mass Spectrometer (IMS-L0), one of the space radiation group of instruments on the Combined Release and Radiation Effects Satellite (CRRES). The purpose of IMS-L0 is to study the low energy (110eV-35 keV) ion component of the ring current plasma. The primary data processing is proceeding rapidly, as is the construction of databases of validated low energy ion data. A number of events have been selected for special study and one of these has been analysed in detail. A tentative identification has been made of a new mechanism which causes loss of ions.				
14. SUBJECT TERMS Geomagnetic Storms, Ring Current, Ions, Radiation Belts			15. NUMBER OF PAGES 86	
			16. PRICE CODE	
17. SECURITY CLASSIFICATION OF REPORT Unclassified	18. SECURITY CLASSIFICATION OF THIS PAGE Unclassified	19. SECURITY CLASSIFICATION OF ABSTRACT Unclassified	20. LIMITATION OF ABSTRACT SAR	

CONTENTS

	page
1. Introduction	1
2. Experiment Status and Operations	3
3. Progress and Current Activities	5
3.1 Generation of Lockheed IMS data base	5
3.2 Empirical model of ring current ion composition	9
3.3 Magnetospheric dynamics inferred from ion transport	9
3.3.1 Introduction	13
3.3.2 Dynamics of the Storm of 26 August 1990	14
3.3.2.1 Observations	14
3.3.2.2 Ion Pressures	23
3.3.2.3 Interpretation of Data	33
3.3.2.3.1 Ion Sources	33
3.3.2.3.2 Variations of Particle Pressures	34
3.3.2.3.3 A New Loss Mechanism	35
4. Future plans	38
References	39
Appendix 1: The Low Energy Ion Mass Spectrometer (ONR 307-8-1,2)	41
Appendix 2: Abstracts of Papers Presented	52
Appendix 3: Distribution in Magnetotail of O ⁺ Ions	56



Accession For	
NTIS GRA&I	<input checked="" type="checkbox"/>
DTIC TAB	<input type="checkbox"/>
Unannounced	<input type="checkbox"/>
Justification	
By _____	
Distribution/	
Availability Codes	
Dist	Avail and/or Special
A-1	

1. Introduction

The effort consists of three Tasks in support of one of the major goals of the Combined Release and Radiation Effects Satellite (CRRES) which is to develop a time-dependent model of the magnetospheric radiation environment that presents a hazard to the performance of spacecraft electronic systems. This effort will model the low energy ion species, H^+ , O^+ , He^+ , and He^{++} .

There is no question regarding the need for such modeling. These heavy-ion species – especially the ones in the ring current with energies extending to 300 keV/e range [Gloeckler et al., 1985] – contribute appreciably to the degradation of spacecraft thermal control surfaces, optical coatings and filters, and other sensitive surfaces. Moreover, these ions are fundamental to the dynamic modeling of the radiation belt: (1) the low energy ions strongly effect the dynamics of the magnetosphere at distances greater than about $7 R_E$ in the magnetotail, and they become strongly affected by the magnetospheric dynamics inward of about $6 R_E$ – Thereby offering a means of modeling the stormtime geoelectric and geomagnetic fields and their effects on all the trapped radiation; (2) these ions are the principal source which is eventually accelerated to become much higher energy particles in the inner radiation belt; and (3) these ions strongly affect the redistribution of inner belt ions – in species type as well as spacially and temporally – and loss through multiple charge-exchange processes and multi-species instabilities and wave-particle interactions.

For example, Wrenn [1989] has recently reported that the rate of recovery of magnetic storms is related to solar cycle. He attributed the change in recovery rate to changes in the ion composition which strongly influences the rate of charge exchange, one of the principal loss processes. Another important ring current loss process is pitch angle diffusion by ion-cyclotron waves. Kozyra et al. [1984] showed that the generation of these waves by the interaction of plasmaspheric plasmas with the ring current is strongly dependent on the composition, densities and temperatures of the interacting plasmas.

The development of a comprehensive and accurate model of the ring current and radiation belts requires a thorough understanding of ring current dynamics, which in turn requires detailed knowledge of the particle source contributions, transport phenomena, energization processes, and scattering and loss mechanisms.

The low energy plasma plays a major role in the dynamics of the inner magnetosphere. A critical component of this plasma is the composition of the ion component. These

low energy ions, which originate in the solar wind and the ionosphere serve as a source for the ring current and radiation belts. The principle tracers of plasma origin in the magnetosphere are measurements of ion flux ratios and charge state density ratios.

Because of limitations in available satellite instrumentation measurement of ion composition in the ring current and radiation belts has begun only fairly recently. The comprehensive data required for an environmental model were not available before CRRES [Williams, 1987] and earlier efforts at modeling the behavior of the low energy ions were imperfect, as evidenced by the number of unanswered question that they raised [Delcourt et al., 1989]. A principal objective of this experiment is to provide a data base suitable for modeling efforts.

Task 1 is to process the raw Lockheed ONR-307-8 Ion Mass Spectrometer (IMS) data from the agency tapes to provide the basic data base of quality controlled calibrated in situ measurements of ion composition upon which the scientific studies are based. The other two Tasks make use of this data base. Task 2 is to construct an empirical, statistical model of the plasma composition and distribution function as a function of magnetospheric location for quiet and disturbed magnetospheric conditions. During magnetic storms the model is to be organized by storm phase in order to reflect the development of the ring current plasma. Task 3 is to investigate aspects of magnetospheric dynamics by making a specialized study of magnetic storm events selected from the Lockheed IMS data base. For each event it will:

- 1) Determine time dependent models of geomagnetic and geoelectric fields consistent with the transport of the measured ions between observation points on successive legs of the CRRES orbit.
- 2) The transport of ions from typical sources of up-flowing ionospheric ions will be computed and compared with the CRRES in situ measurements of magnetospheric ions. The ion transport will also be compared with possible storm predictors.

We will make use of observations of ion species, principally H^+ , O^+ , He^{++} and He^+ , in the energy range 100 eV/e to about 100 keV/e. These ions become strongly affected by the magnetospheric dynamics thereby offering a means of modeling the stormtime geoelectric and geomagnetic fields and their effects on all the trapped radiation. They are the principal source of ions which are eventually accelerated to become much higher energy particles in the inner radiation belt and they strongly affect the redistribution and loss of inner belt ions through multiple charge-exchange processes and multi-species instabilities and wave-particle interactions.

To achieve these objectives ONR 307-8-1,2 (IMS-LO) is designed to measure plasmas

that are the sources of radiation belt particles, and to provide data on the origin and acceleration of these plasmas. To achieve these objectives IMS-LO measures energy and mass spectra covering the ranges of E/q from 0.1 to 35 keV/e and M/q from 1 to 32 AMU/e with good coverage of pitch angles throughout the orbit. A full description of this instrument is in Appendix 1

2. Experiment Status and Operations

CRRES was successfully launched on 25 July 1990 and initialization operations of the ONR 307-8 instruments, which provide data that are used for this contract, began shortly thereafter. Notable events in the initialization sequence are summarized in table 1.

Table 1 ONR 307-8-1,2 initialization events

Date	Time (UT)	Orbit	Event
28 July	21:40	8.1	Power on
29 July	07:40	9.1	Memory load and check
2 August	10:50	19.1	8-1 high voltage on
2 August	21:40	20.1	8-2 high voltage on
4 August	12:00	24.1	Configure for normal operations
26 August	17:10	78.1	Reconfigure for SWEEP-LOCK mode

Initialization proceeded smoothly. Following initialization, ONR 307-8-1 and ONR 307-8-2 were operated in SWEEP/LOCK mode to give good sensitivity and temporal and pitch-angle resolution of the major species H^+ , and O^+ , while retaining full mass resolution.

Both instruments continue to work perfectly. Almost the only non-scheduled loss of data occurs as a result of the loss of synchronization caused by the dropouts in the vehicle clock. When these occur the instruments lose synchronization but are able to recover within a couple of minutes.

The only other anomaly which has occurred to date, happened on 18 July 1991 when the CSTC controller reported that ONR 307-8-1 was cooling rapidly and its high voltage monitors were showing abnormally low values. The status of the instrument was examined

on the next available contact and it was ascertained that one of its control registers had become incorrectly set and that in consequence two of the high voltage generators had been dis-enabled. The fall of instrument temperature was the result of the reduction in power consumption. Commands were sent at once to reset the control register and restart the high voltage generators. The precise cause of the registers becoming unset is not clear. Geophysical conditions were very disturbed at the time and it is probable that a charging event or SEU was the ultimate cause.

The failure of battery 2, on 22 December 1990 led to duty cycling of the ONR 307-8 instruments during eclipses in order to conserve the limited battery power. The instrument temperatures were monitored and although they cooled considerably they did not reach dangerously low levels.

Data analysis has been proceeding steadily and all the scientists have taken part in CRRES science working groups. The American Geophysical Union devoted a special session to preliminary reports of CRRES data at its Spring Meeting in Baltimore. Two papers were presented; 'Low Energy Ring Current Ions during the Storm of 26 August 1990: Observations by IMS-LO on CRRES', by H. L. Collin, J. M. Quinn J. B. Cladis, J. B. Cladis, and 'Storm-Time Dynamics Implied by the CRRES Measurements of Ring-Current Ions', by J. B. Cladis, H. L. Collin, and W. E. Francis. Abstracts of these papers are in Appendix 2.

In addition to radiation studies an objective of the CRRES mission is a series of chemical release experiments. The releases were made in three very successful campaigns. At low altitude during September 1990, and July and August 1991, and at high altitude during January and February 1991. ONR 307-8-1,2 supported these chemical release campaigns under contracts from NASA. During the high altitude chemical release campaign ONR 307-8-2 was run in operating modes specially designed to enhance its sensitivity to Ba^+ or Li^+ and these modes were commanded in real time to match the release selected by the chemical release Principal Investigators. Support was also provided by supplying the Principal Investigators with real time data on the plasma conditions in the magnetosphere. This information was helpful in choosing the optimum release time. During the low altitude campaigns ONR 307-8-2 was run in a mode sensitive to Ba^+ . Some of this activity was reported in a paper presented at the Spring Meeting of the American Geophysical Union in Baltimore in the special session devoted to the chemical release portion of the CRRES mission; 'Real Time Monitoring of the Geophysical Parameters in Support of the

CRRES Chemical Releases', by S. B. Mende, H. L. Collin, W. K. Peterson, T. A. Fritz, G. Haerendel, R. R. Anderson, D. A. Hardy, H. J. Singer, J. C. Foster, and D. L. Reasoner. An abstract of this paper is included in Appendix 2.

3. Progress and Current Activities

3.1 Generation of Lockheed IMS data base

The first step in the analysis of the CRRES data involves processing the agency tapes provided by the Phillips Laboratory. The agency tapes for Lockheed contain data from each of the ONR 307 instruments together with ephemeris and magnetometer data. A schematic of the data processing sequence showing the relationship of analysis, databases and data products is in Figure 1. The first stage of processing is to unpack and decode the data on the agency tapes, and write the data from each orbit to a group of files corresponding to each instrument together with ephemeris and magnetometer data. At this stage all data is in the form of counts or engineering units at the full resolution of the instrument and is independent of possible drifts or revisions of detector calibrations. This forms the basic High Resolution Database which is used as the basis of all other analysis. It is held on a series of optical disks each of which holds data from 26 orbits.

The second stage of data processing is the production of the Survey Plot Library. This consists of full orbit survey plots for all orbits. This library forms an important intermediate data product which displays IMS-LO data in a form which is compact and also sufficiently detailed to enable periods of scientific interest to be selected for specialized study under Task 3 or for other purposes. The survey plots are also an important tool for the assessment of instrument performance. For all survey plots the data are averaged over 262s intervals. The examples shown in Figures 2 to 4 are taken from the storm of 26 August 1990 which is a period of special study by the CRRES Low Energy Plasma Field and Wave Working Group and is discussed in detail in section 3.3.2. Figure 2 shows a survey plot of mass spectra as a function of time from orbit 77, 26 August 1990. The upper group of three panels show mass spectra from the three heads of IMS-LO-1. Each panel contains horizontal bands near the bottom and top which correspond to H^+ and

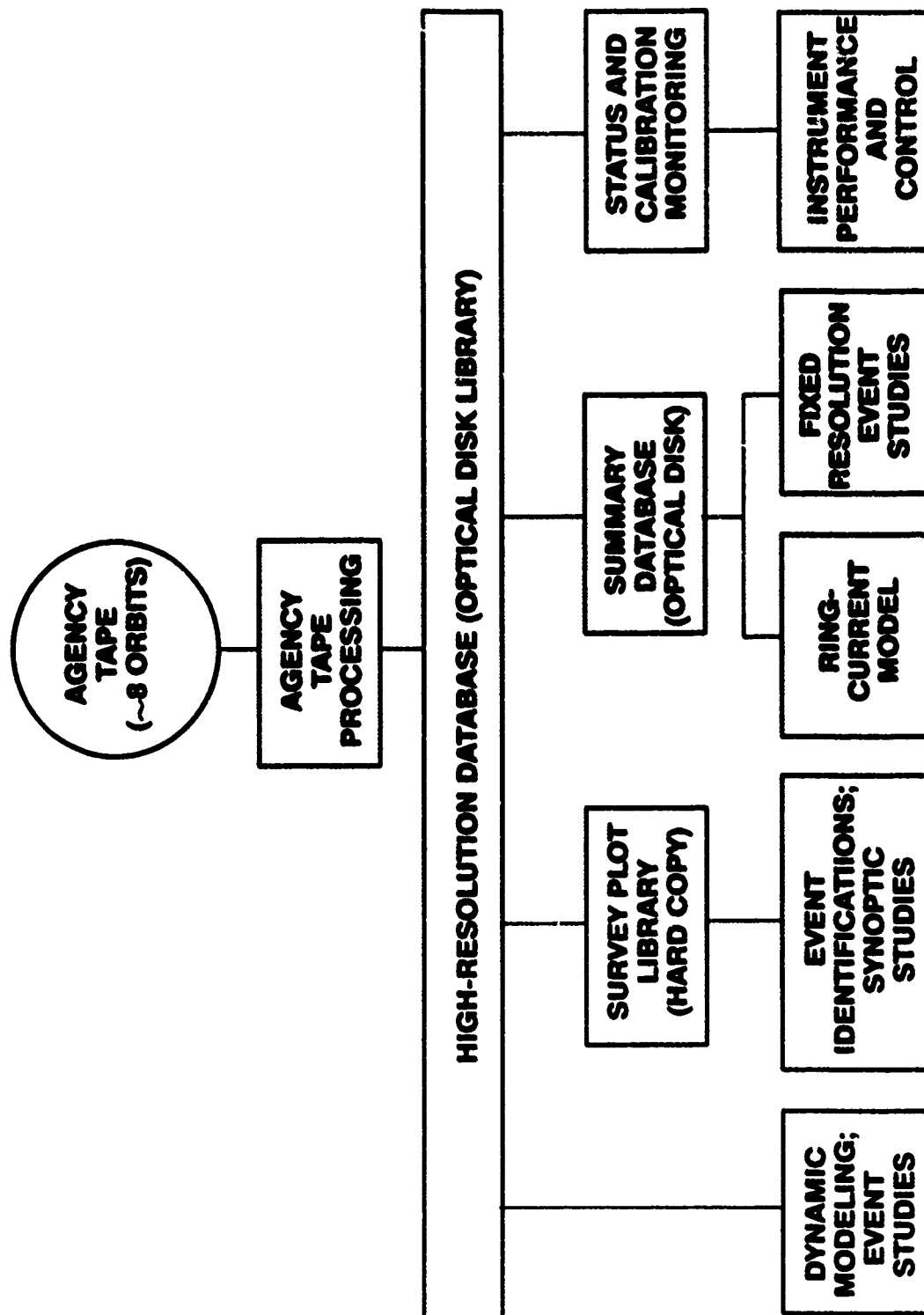


Figure 1. Data processing flow for IMS-L0

O^+ respectively. Fainter discontinuous bands between them correspond to He^+ and He^{++} . The lower group of three panels show similar mass spectra from IMS-LO-2. Survey plots of energy spectra and pitch-angle distributions for orbit 76 and orbit 77 are shown in Figure 3 and Figure 4 respectively. The upper group of four panels show energy spectra of H^+ , O^+ , He^+ , and He^{++} . For these plots the flux has been sorted into 15 logarithmically spaced energy bins. The lower two groups of three panels display the pitch-angle distributions of H^+ and O^+ in each of the three energy bands corresponding to the three heads which make up the IMS-LO spectrometer. For each of these the flux has been sorted into 15° pitch-angle bins.

Special event studies and dynamic modeling which need maximum resolution and flexibility make direct use of the High Resolution Database. Plots of energy spectra and pitch angle distributions for selected periods of data were produced as part of the study of storm of 26 August 1990 in order to permit more detailed examination than is possible with the survey plots. Examples are shown in Figure 5 the upper panel of which shows O^+ energy spectra at a series of pitch angles. The flux equivalents of the background count rate and the one count per sample are shown for comparison. In the lower panel the same O^+ data displayed as pitch-angle distributions at a series of energies. The O^+ is seen to be isotropic at energies above 0.5 keV while at lower energies it displays a pitch-angle distribution which is strongly asymmetric with a marked field aligned flow at pitch angles above 120° . These distributions are discussed further in section 3.3.2.

Other routine uses of the High Resolution Database are the production of the Summary Database, which is described in section 3.2, and the monitoring of instrument status and calibration. Reviews of in flight calibration has led to minor revisions of some of the mass settings used in the LOCK mode. These revisions resulted in a modest, but worthwhile, increase in sensitivity. We have made a provisional alignment of the calibration of the three heads which make up each of the ONR 307-8 instruments, and between the two instruments ONR 307-8-1 and ONR 307-8-2 which enables the slight differences between their geometry factors to be accounted for.

Initially the data processing was carried out on a VAX-780. Later, however, a SUN system was made available and the major part of the data processing and analysis has been transferred to this system. Eventually almost all analysis will be carried out on this new system. The transfer of software caused some temporary delay which was rapidly overcome due to the much greater computing power of the SUN system. All agency tapes

received to date have now been processed.

3.2 Empirical model of ring-current ion composition

The preliminary version of the Empirical Model of Low Energy Ring Current Ion Composition will consist of a set of average equatorial energy pitch-angle distributions of H^+ and O^+ . The precession of the CRRES orbit will eventually enable the model to cover all magnetic latitudes as well as L values up to about 7. These average distributions will be compiled from ion measurements taken along the CRRES orbit and mapped to the magnetic equator. The model can then be used to determine the average ion distributions away from the equator by mapping the equatorial distributions down the field lines to the location of interest. As data accumulates and understanding of the behaviour of the ring-current plasma improves the model will be expanded to include the effects of magnetic storms.

Increased understanding of the behaviour of the storm-time magnetosphere is likely to produce improvements in the models used to describe the geomagnetic field and so to require changes in the mapping of ion trajectories between CRRES and the equator and thus revision of the empirical model of ring-current ion composition. In order to avoid the computational burden of having to generate the model from the High Resolution Database each time a revision is needed an intermediate data base is being constructed. This IMS-LO Summary Data Base is a compact, partially processed data base consisting of averages, over 262 seconds, of IMS-LO ion and electron data sorted by energy and pitch angle. Data from both IMS-LO-1 and IMS-LO-2 is combined. Supporting data include time, background count rate, status information, measured magnetic field and ephemeris information. This Summary Data Base is also suitable for rapid retrieval of energy spectra, pitch angle distributions or survey plots when the full resolution is not required, and as a basis for statistical studies. The ion and electron data are recorded as count rates in order to make the data base independent of revisions to the instrument calibration which cross calibration studies are expected to indicate. Calibrations are applied to the count rates when the data base is accessed.

3.3 Magnetospheric dynamics inferred from ion transport

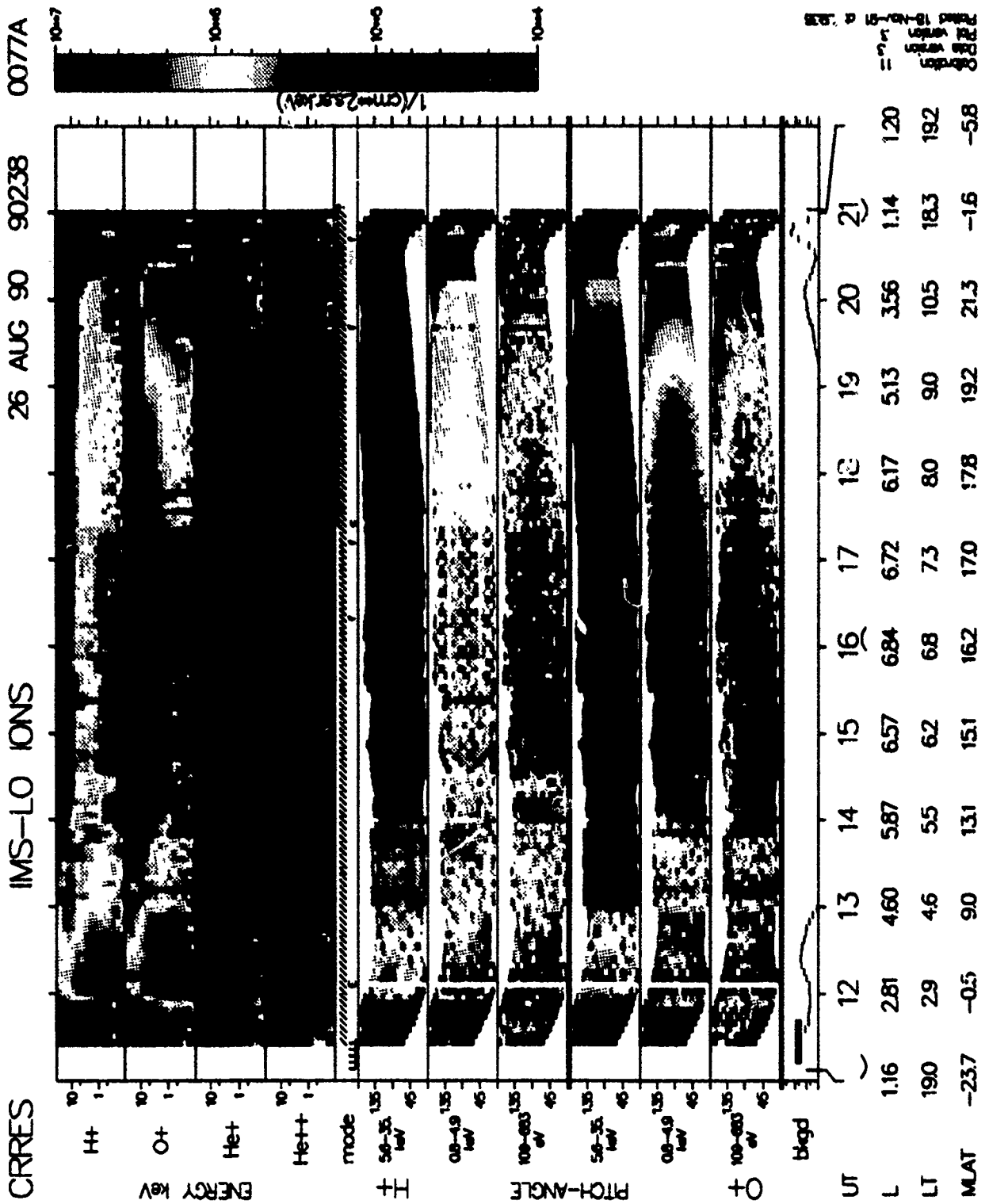


Figure 4. Survey plots of energy spectra and pitch-angle distributions for orbit 77.

L = 6.67-6.81

15:14:28-15:45:03 54868-56703

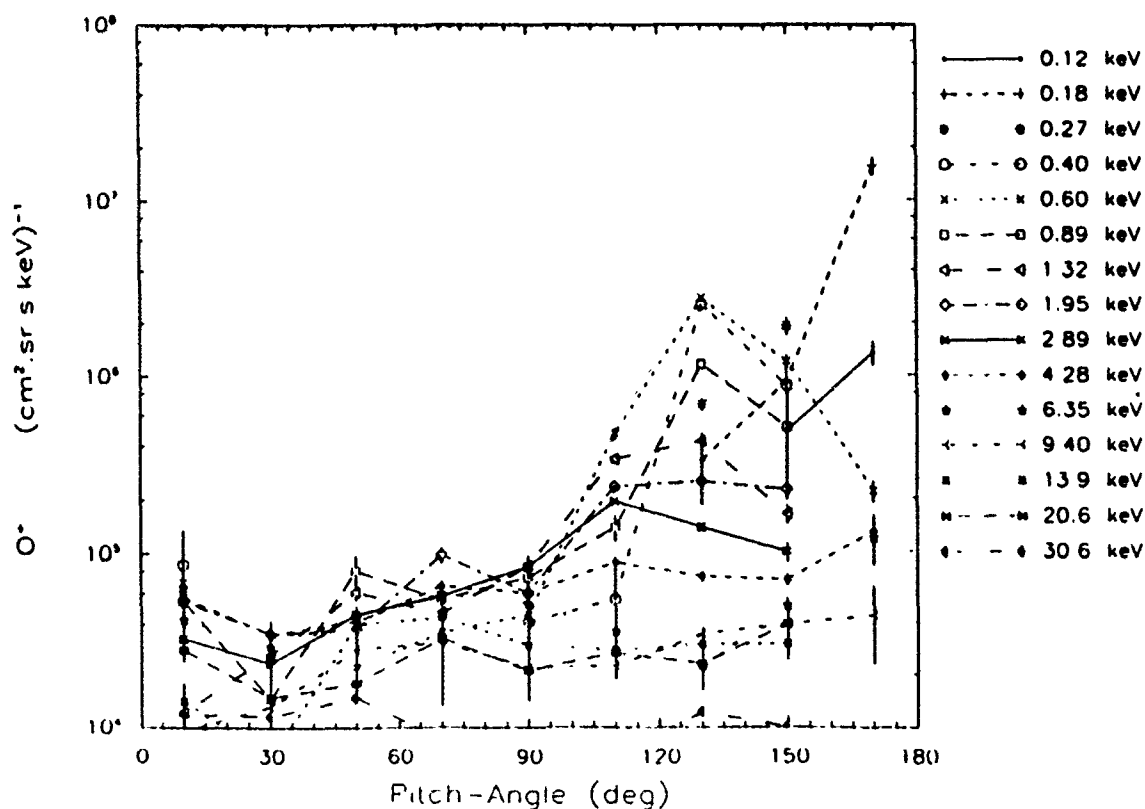
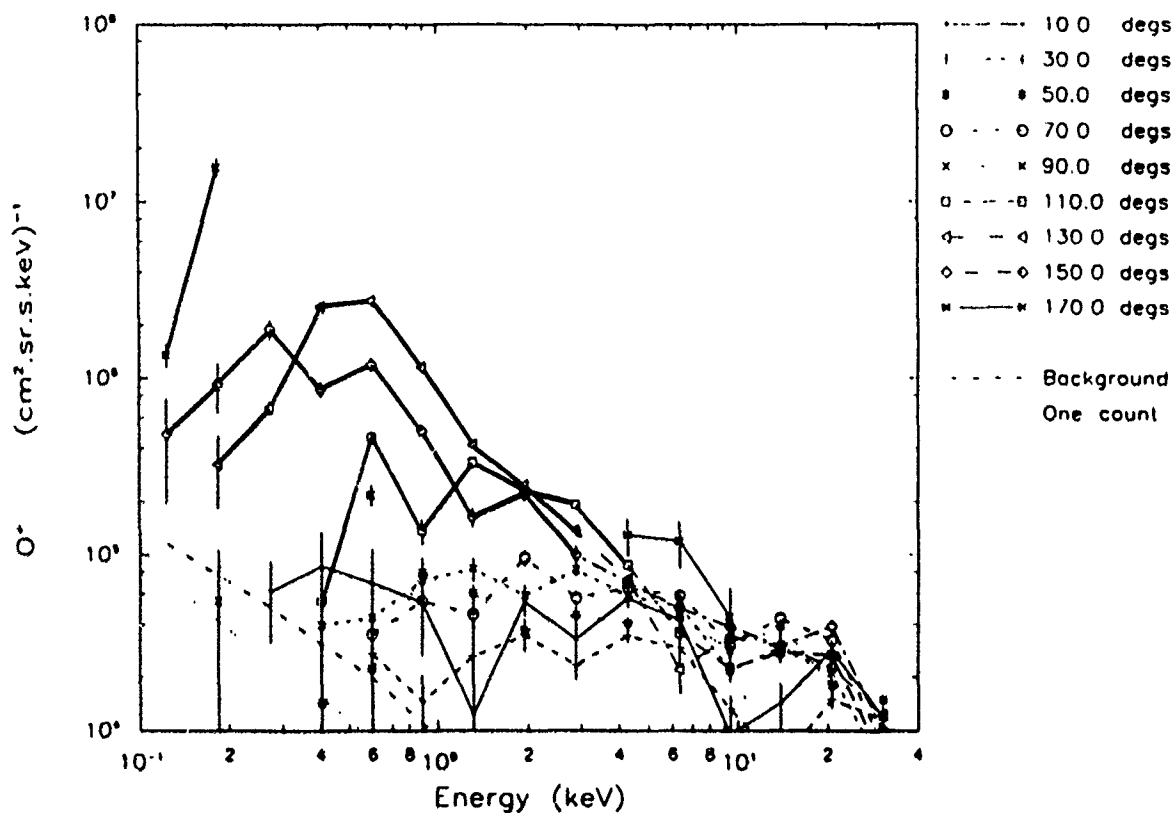


Figure 5. O⁺ energy spectra at a series of pitch angles and pitch-angle distributions at a series of energies.

3.3.1 Introduction

The objectives of this task are to use the ion data during disturbance events (substorms and magnetic storms) to infer the underlying dynamics of the magnetosphere, *e.g.* the time-dependent magnetic and electric fields, and sources of the ions injected into the trapping region of the magnetosphere. The ions measured with the IMS-LO and IMS-HI instruments, particularly the species H^+ , O^+ , He^{++} , and He^+ in the energy range 0.2 keV/e to about 300 keV/e, will be used in this study. Further information useful to this study include the onboard magnetic and electric field measurements, high energy proton and electron data, IMP-8 solar-wind measurements, geomagnetic indices, and available ion data from other spacecraft (*e.g.*, DMSP and Akebono).

The magnetic and electric fields will be studied by computing the drift paths (eastward and westward) of the ions in trial field models between one leg (inbound or outbound) of the CRRES orbit to the succeeding leg. Liouville's theorem will be used to assess the trial field models. That is, if the fields along the ion paths are correct, the phase space densities of the ions measured at the satellite at the two points will be the same. Corrections will be made for charge exchange losses. Additional ion-dependent redistributions or losses due to instabilities or wave-particle interactions will be inferred from the results obtained for the different species.

One of the complications of this study is that the ions are not only affected by the magnetic and electric fields, but they also affect the fields through their collective behaviour. During substorms, ions of energy less than about 50 keV appreciably affect the magnetic and electric fields in the near-earth magnetotail and nightside magnetosphere (*e.g.*, see the attached preprint by Cladis and Francis [1991] in Appendix 3). During magnetic storms, ions of energy to about 300 keV affect the fields throughout the magnetosphere. Also, during the initial phase of a magnetic storm, the fields may change so rapidly in time and space that it may not be possible to obtain reliable estimates of the variation of the fields along the ion drift paths. For these reasons the study will begin with quiet-time conditions and proceed toward more disturbed times as experience is gained on the evolution of the fields and the sources and losses of the ions.

Good data on the low-energy ion fluxes measured with the IMS-LO instruments are already available for the study, and approximate IMS-HI fluxes are expected to be available in a few months. The ion transport models and preliminary trial magnetic and convection

electric fields are already available. A model of the induced electric field resulting from compressions and rarefactions of the magnetosphere has not yet been developed.

To date, the principal effort on Task 3 has been devoted to the study of the dynamics of the magnetic storm of 26 August 1990. This effort is described below.

3.3.2 Dynamics of the Storm of 26 August 1990

3.3.2.1 Observations

The IMS-8 measurements of the interplanetary magnetic field (IMF) and the plasma in the solar wind were kindly sent to us by S. Gussenhoven of PL/GD. for day 238 (26 August 1990), Leppings measurements of the total magnetic field strength and its components are shown in Figures 6a - 6d, and Lazarus' measurements of the plasma density and speed are shown in Figure 7. The significance of the vertical lines in Figure 7 will be discussed later. Singer's magnetic field measurements on CRRES in VHD coordinates, which he designates as X,Y,Z, are shown in Figures 8a and 8b. In these Figures δB_x , δB_y , and δB_z are the differences of the measured components from the components given by the Olson-Pfizer magnetic field model. The total magnetic field strength is given in the bottom panel, and the broken-line curve in this panel is the model field strength.

Note from Figures 6 and 7 that the interplanetary shock is first observed by IMP-8 at about 05:40UT and, from Figure 8a, that the sudden commencement is observed on CRRES at 05:53UT. At the time of the sudden commencement, the B_z component suddenly increases by about 15 nT and long trains of ULF oscillations, particularly in the B_y component, are initiated. At about 06:15UT the interplanetary B_z component, as shown in Figure 6d turned southward, and the nose of the magnetosphere, as determined by equating the solar wind pressure $\frac{1}{2}n_{sw}m_p v_{sw}^2$ to the magnetic field pressure $B_D^2/2\mu_0$ at the subsolar point, moved inward to about $6.5 R_E$. Here, n_{sw} and v_{sw} are the number density (assumed to consist of H^+ alone) and the speed of the solar wind, respectively, taken from Figure 7; and B_D is the dipole magnetic field strength at the subsolar point, taking the dipole tilt angle at that time into account. The nose position, based on a smoothing of the available solar-wind data, for 25-26 August is shown in Figure 9.

YEAR = 1990, DAY = 238
B (Magnitude)

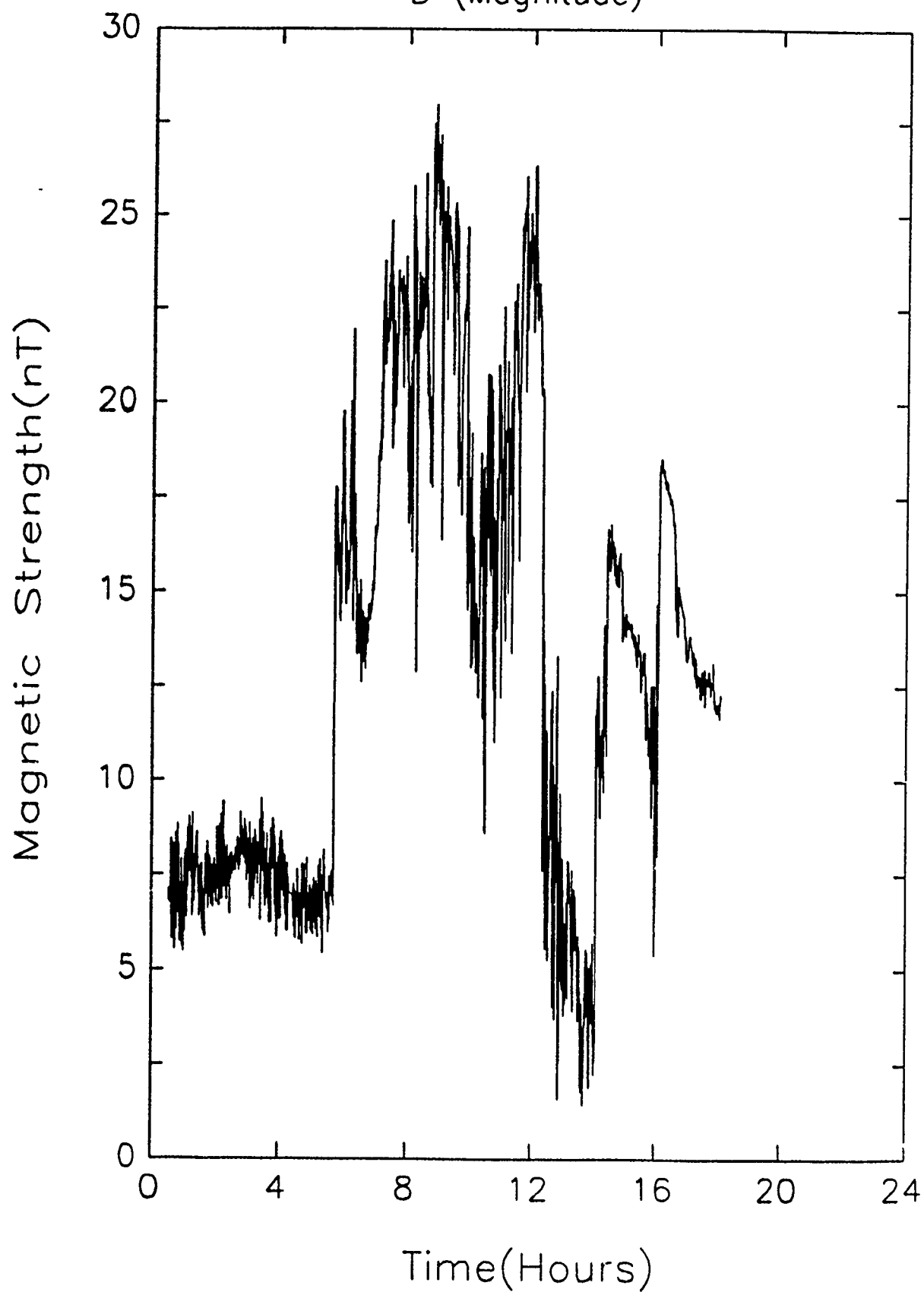


Figure 6a. IMP-8 IMF data. (Courtesy of R. Lepping)

YEAR = 1990, DAY = 238

Bx (X componet)

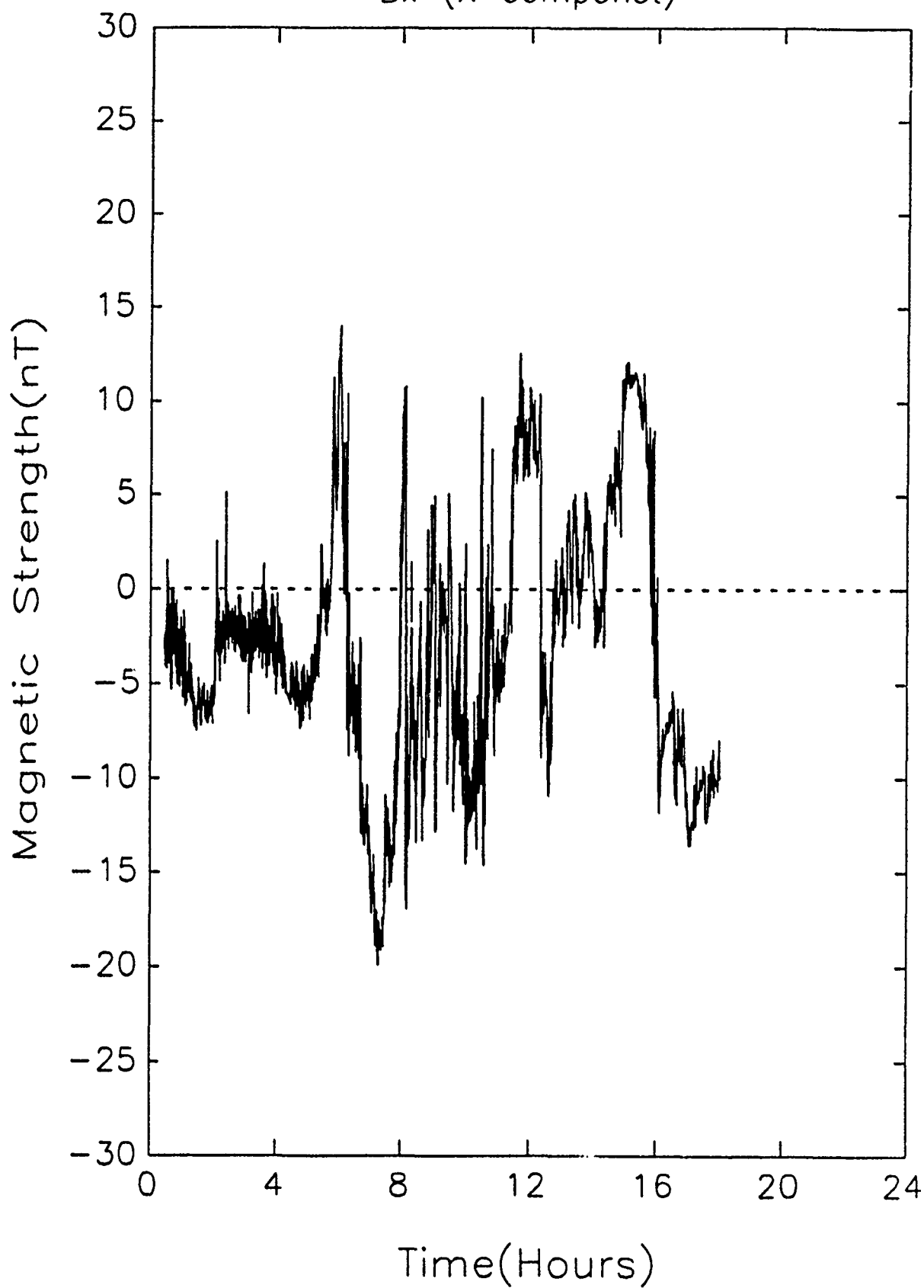


Figure 6b. IMP-8 IMF data. X component. (Courtesy of R. Lepping)

YEAR = 1990, DAY = 238

By (Y componet)

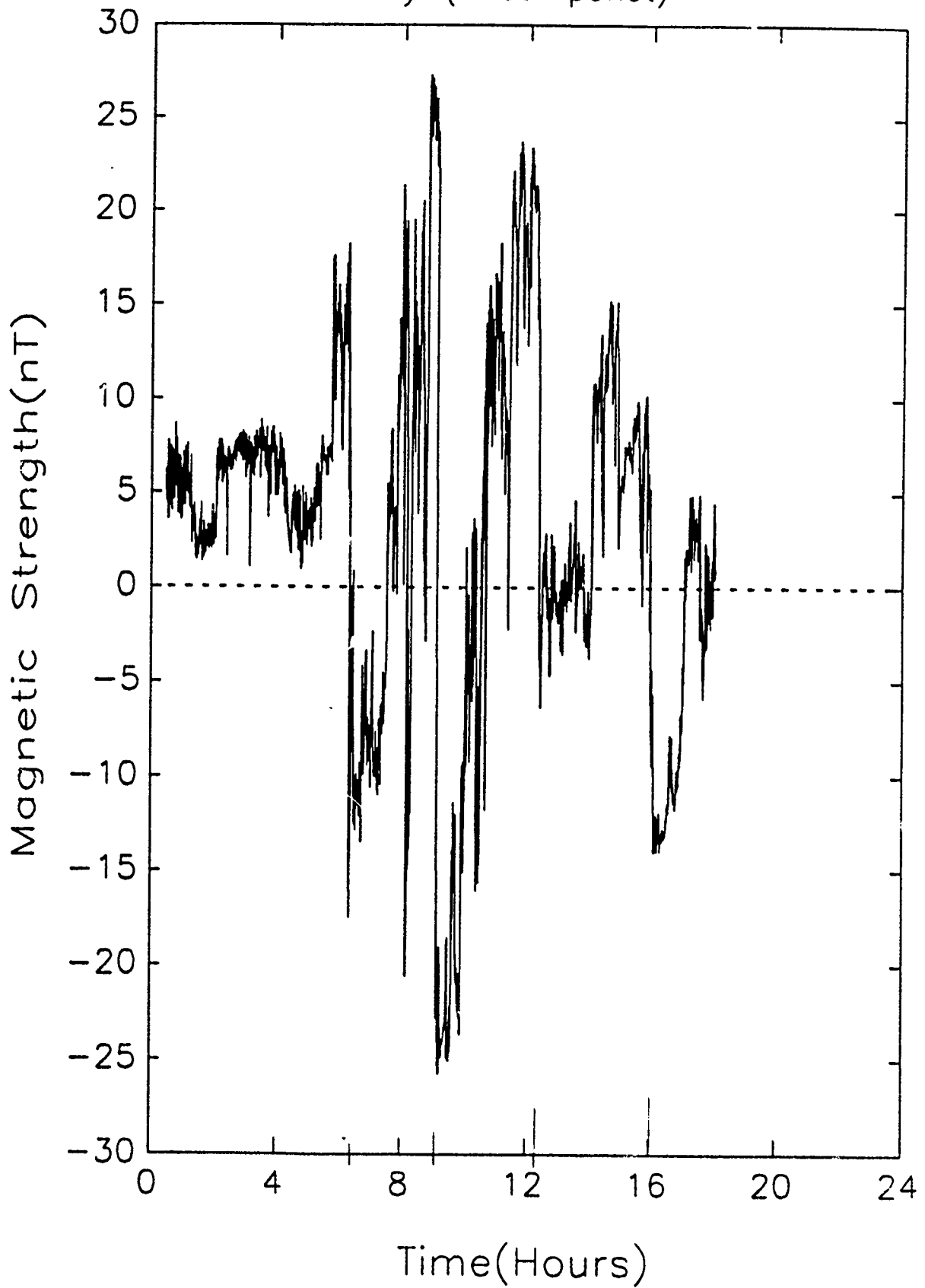


Figure 6c. IMP-8 IMF data. Y component. (Courtesy of R. Lepping)

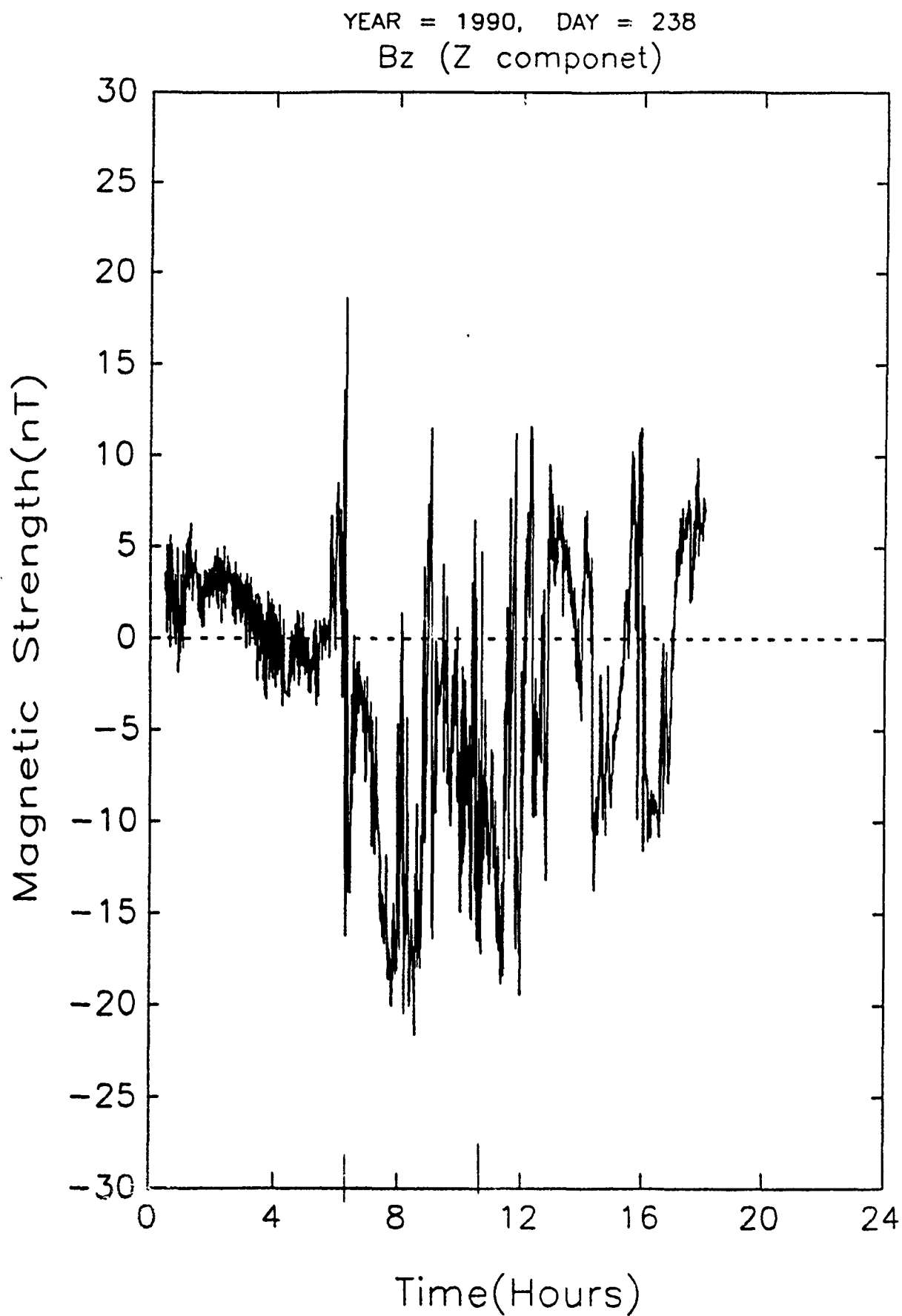


Figure 6d. IMP-8 IMF data. Z component. (Courtesy of R. Lepping)

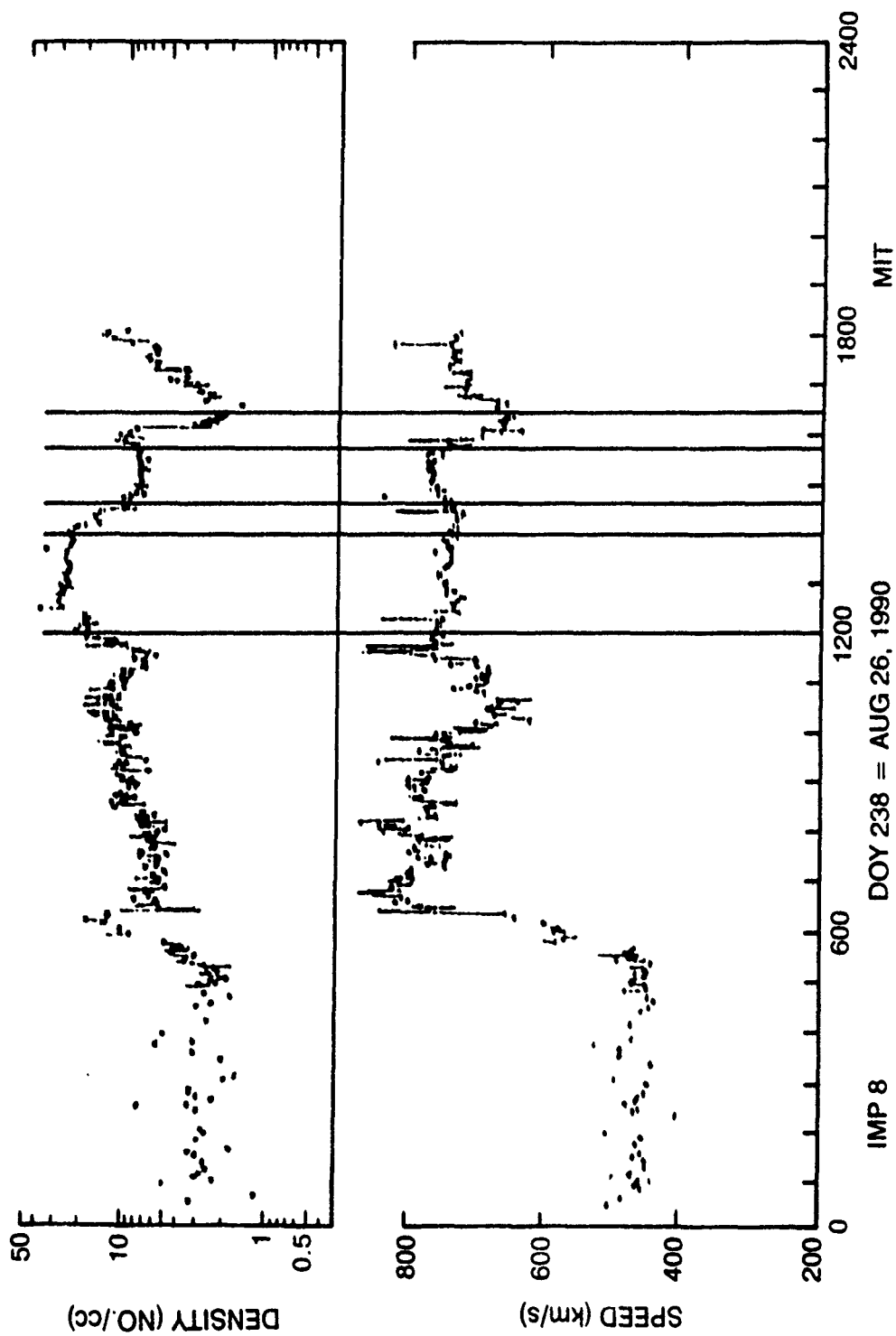


Figure 7. IMP-8 Solar-Plasma data (Courtesy of A. Lazarus)

1991-01-29 17:28:33 v.2

CRRES VDH Magnetic Fields Orbit 76 238/90 Aug 26

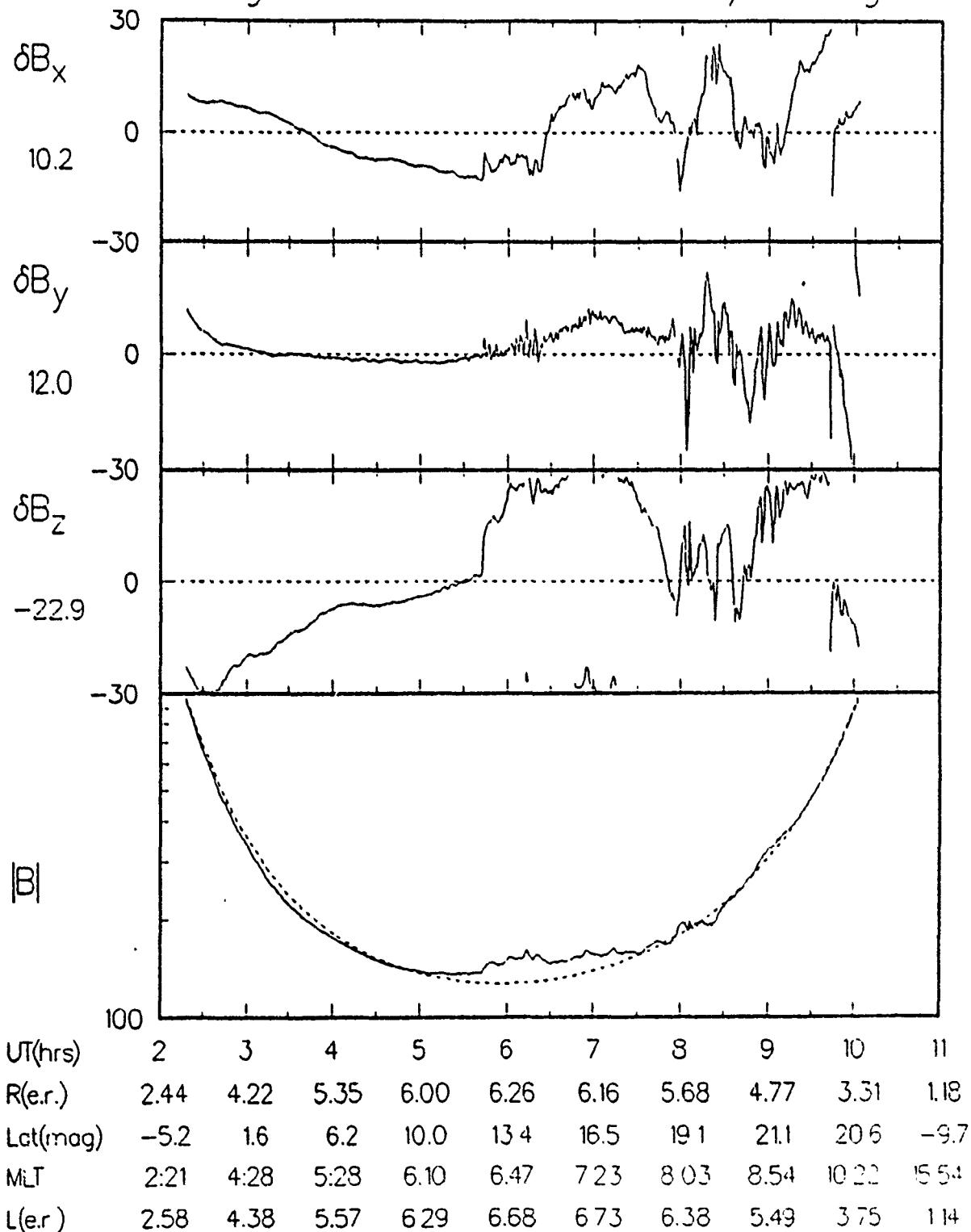
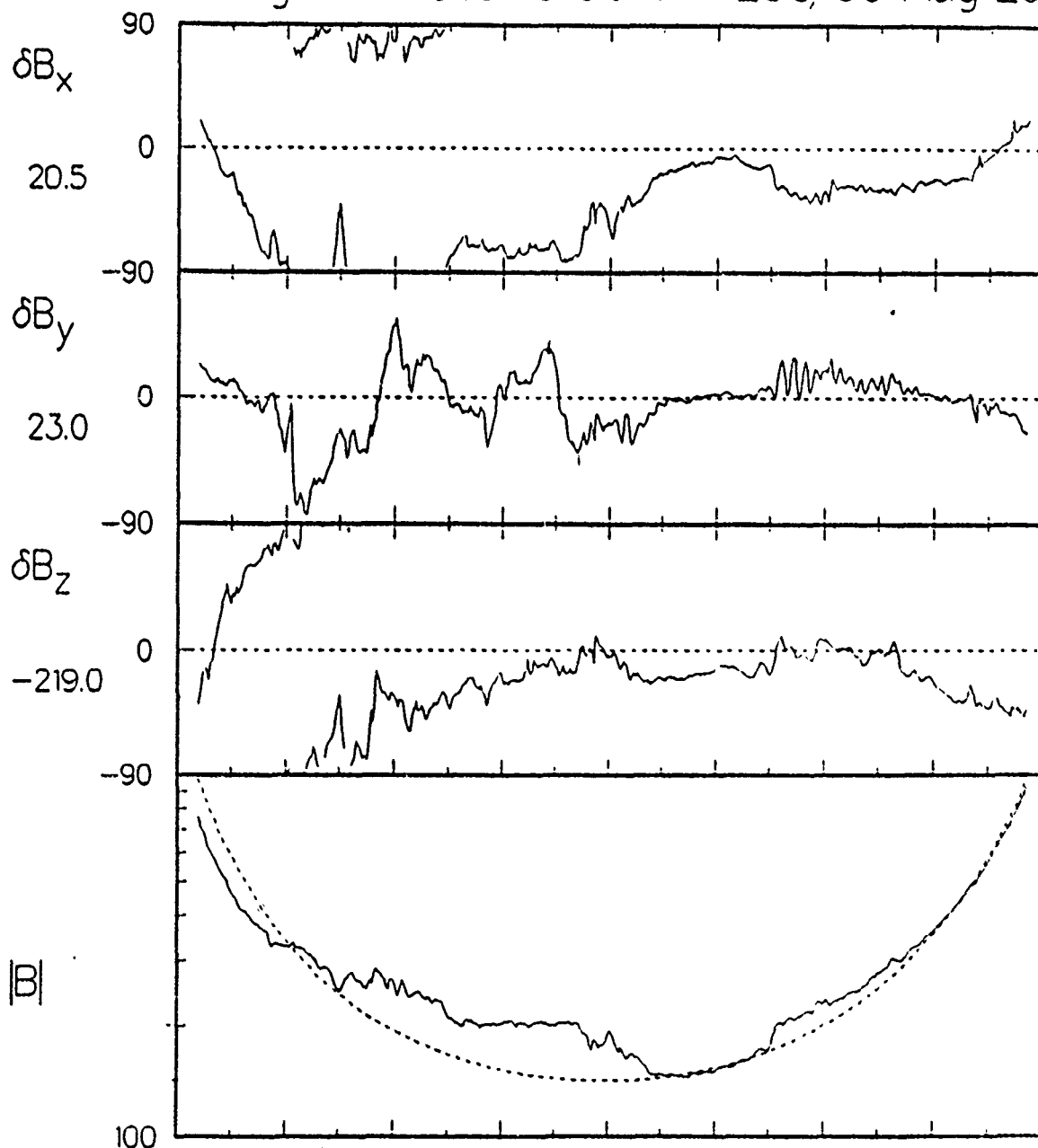


Figure 8a. CRRES magnetic field measurements on orbit 76. (Courtesy of H. Singer)

1991-01-29 17:34:37 v.2

CRRES VDH Magnetic Fields Orbit 77 238/90 Aug 26



UT(hrs)	12	13	14	15	16	17	18	19	20
R(er.)	2.74	4.41	5.46	6.06	6.27	6.11	5.58	4.61	3.05
Lat(mag)	-1.1	9.2	13.1	15.1	16.2	17.0	17.8	19.1	21.3
MLT	2:42	4:21	5:13	5:53	6:30	7:07	7:50	8:46	10:27
L(er.)	2.75	4.64	5.87	6.57	6.84	6.71	6.17	5.15	3.49

Figure 8b. CRRES magnetic field measurements on orbit 77. (Courtesy of H. Singer)

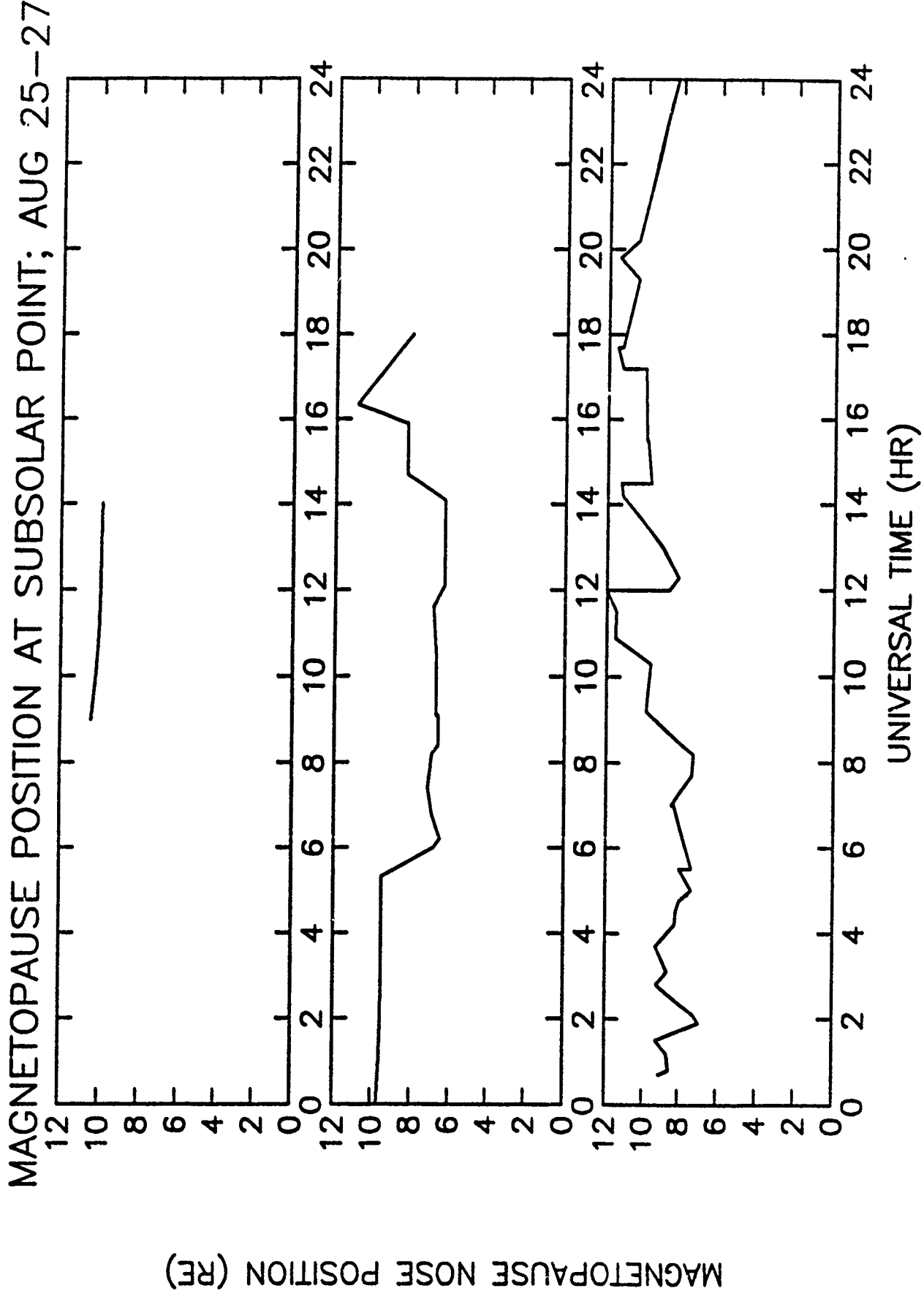


Figure 9. Nose position of the magnetosphere during the storm of 25-27 August 1990.

Sharply enhanced fluxes of H^+ , He^+ , and O^+ were detected with IMS-LO at 08:00 UT, when CRRES was at $L \approx 6.3$ and 07:30 LT, and these fluxes were repeatedly observed in the region $3.2 \leq L \leq 6.8$ and $03:00 \leq MLT \leq 10:30$. The time sequence of the pitch-angle and energy distributions of these ions are shown in Figures 3 and 4.

3.3.2.2 Ion Pressures

In order to describe the general characteristics of the ions that were injected and accelerated in the trapping region of the magnetosphere, the parallel and perpendicular pressures of the ions measured with IMS-LO were computed for the duration of the storm. When the IMS-HI ion fluxes will be available, their pressures too will be computed and added to the low energy ion pressures. Since most of the partial pressure is due to ions in the range 50 to 300 keV, the inclusion of the higher energy pressures will provide additional information on the dynamics of the magnetosphere in general and on the affect of the ions on the geomagnetic field in particular.

The partial pressure component perpendicular to the magnetic field is given by the perpendicular energy component, $\frac{1}{2}mv^2 \sin^2 \alpha$, weighted by the distribution function, $f(\vec{v})$, and integrated over velocity space. That is,

$$P_{\perp} = \int \frac{1}{2}mv^2 \sin^2 \alpha f(\vec{v}) d\vec{v}$$

Similarly, the parallel pressure is given by the equation

$$P_{\parallel} = \int mv^2 \cos^2 \alpha f(\vec{v}) d\vec{v}$$

In terms of the flux, $j(w, \alpha, T)$, that is plotted in Figures 3 and 4, the pressures as a function of time, T , are given by the equations

$$P_{\perp}(T) = 2\pi \sqrt{\frac{m}{2}} \int_{w_{min}}^{w_{max}} \sqrt{w} dw \int_{\alpha_{min}}^{\alpha_{max}} j(w, \alpha, T) \sin^3 \alpha d\alpha$$

$$P_{\parallel}(T) = 4\pi \sqrt{\frac{m}{2}} \int_{w_{min}}^{w_{max}} \sqrt{w} dw \int_{\alpha_{min}}^{\alpha_{max}} j(w, \alpha, T) \cos^2 \alpha \sin \alpha d\alpha$$

These equations were integrated from $w_{min} = 0.11$ keV to $w_{max} = 35$ keV. As shown in the pitch-angle distributions of the ions (Figures 3 and 4), the measurements are nearly over the full pitch-angle range $\alpha_{min} \geq 10^\circ$ to $\alpha_{max} \leq 170^\circ$.

In Figures 10a-10h the ion pressures, in units of keV/cm³, are plotted as a function of time (UT) in hours for orbits 75 through 82. The panels starting from the top of each figure give pressures of (1) H⁺, (2) He⁺, (3) O⁺, and (4) the sum of H⁺, He⁺, and O⁺. The next panel, (5) gives the plasma β ,

$$\beta(T) = 2\mu_0 \frac{P_{\perp}(T)}{B^2}$$

which is the ratio of the total perpendicular pressure of the ions to the magnetic-field energy density. The last panel (6), gives the L-shell of the measurements, as determined from the Olson-Pfizer magnetic field model. In the upper four panels, the solid and broken-line curves give the perpendicular and parallel pressure components respectively.

Note that during the orbit preceding the storm, i.e. Orbit 75 of Figure 10a, nearly the entire pressure is due to H⁺ and that its perpendicular pressure exceeds the parallel pressure at all times. The He⁺ and O⁺ pressures are significantly above background only at low L values; the rapid fluctuations of the pressures reflect the poor statistics of the measurements. Moreover, the plasma β is small, with its maximum value being about 0.6% over a broad region at L \geq 5.

On the next orbit (Figure 10b), all the ion pressures increase significantly near 08:00 UT. Note that the injected H⁺ is very nearly isotropic (the pressure components are equal), but the parallel pressure of O⁺ exceeds the perpendicular pressure. Transport calculations reveal that, in the outer magnetosphere, fluxes of ions that recently emerge from the ionosphere are anisotropic, with the parallel component exceeding the perpendicular component. The maximum value of β of the low energy ions is about 3% at L \approx 6.1 during the inbound pass of the satellite.

On orbit 77 (Figure 10c), quasiperiodic variations of the particle pressures, with periods of about one hour, occur between 12:00 and 16:00 UT. A tentative explanation of these variations is given in the following section. Note also in this figure that H⁺ is still isotropic and that the He⁺ and O⁺ have parallel pressure components that often exceed their perpendicular pressures. As revealed by the O⁺ pitch-angle distributions, the lower energy ions at high L values generally have the highest pitch-angle isotropies (butterfly distributions). These too are discussed in the following section. The maximum value of β in this orbit is about 2.3%.

During orbits 78 to 82, the H⁺ distributions evolve fairly rapidly toward normal distributions, with the perpendicular pressure exceeding the parallel pressure, especially

CRRES DATA FOR ORBIT = 76
Parallel Pressure(dashed), Perpendicular(solid)

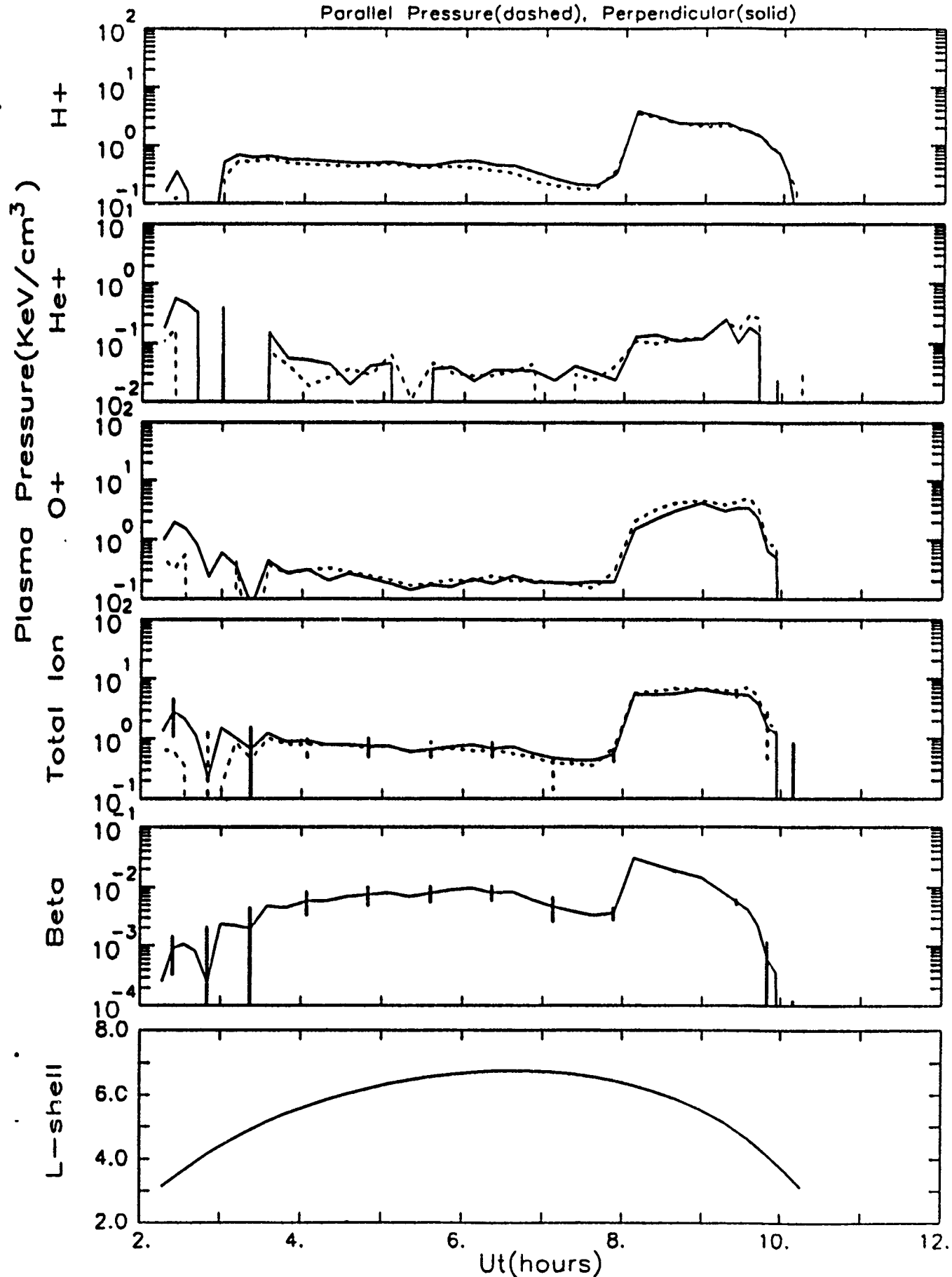


Figure 10b. Perpendicular and parallel pressures of H⁺, He⁺, and O⁺ during orbit 76.

CRRES DATA FOR ORBIT = 75
Parallel Pressure(dashed), Perpendicular(solid)

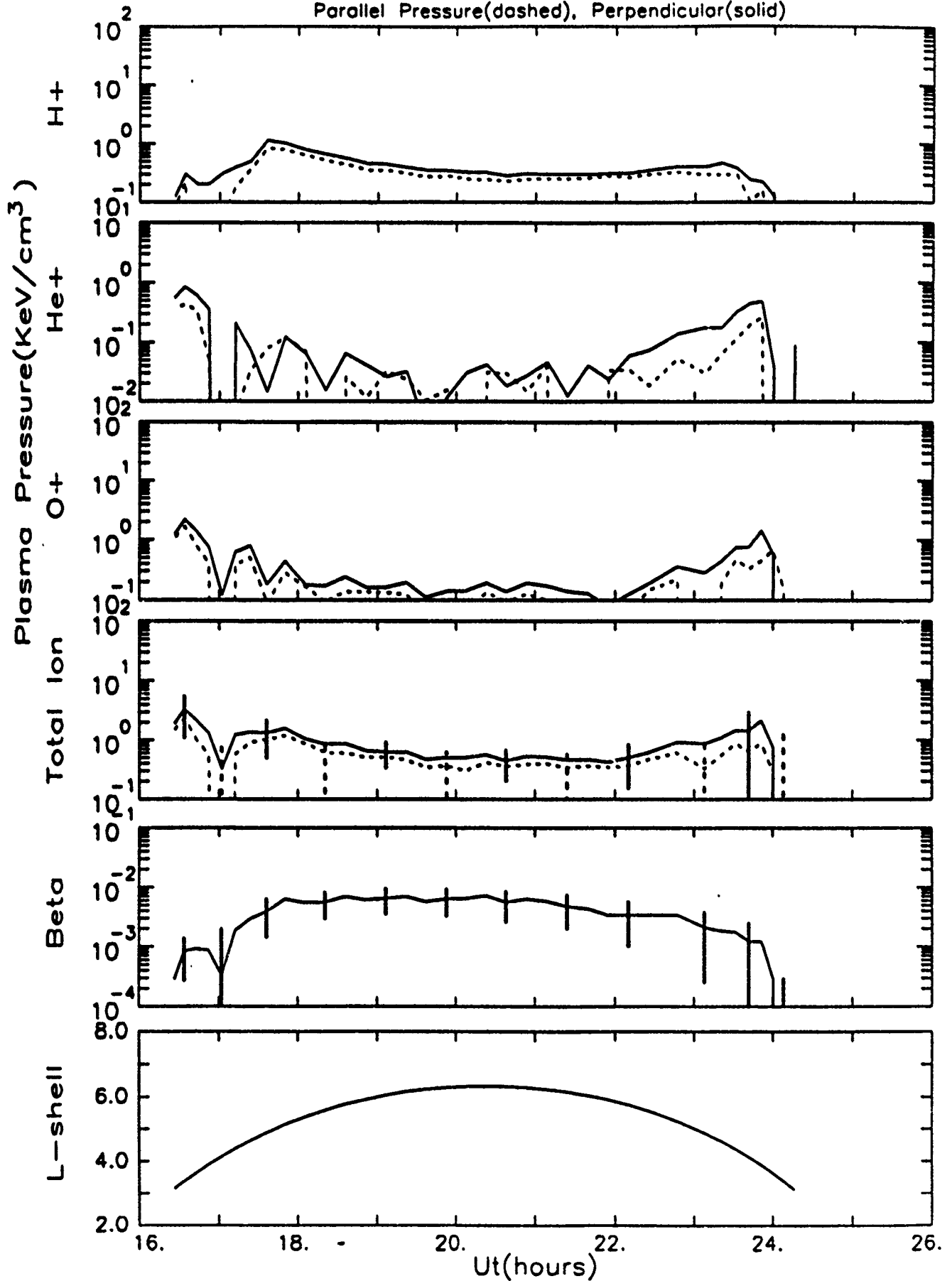


Figure 10a. Perpendicular and parallel pressures of H⁺, He⁺, and O⁺ during orbit 75.

CRRES DATA FOR ORBIT = 77
Parallel Pressure(dashed), Perpendicular(solid)

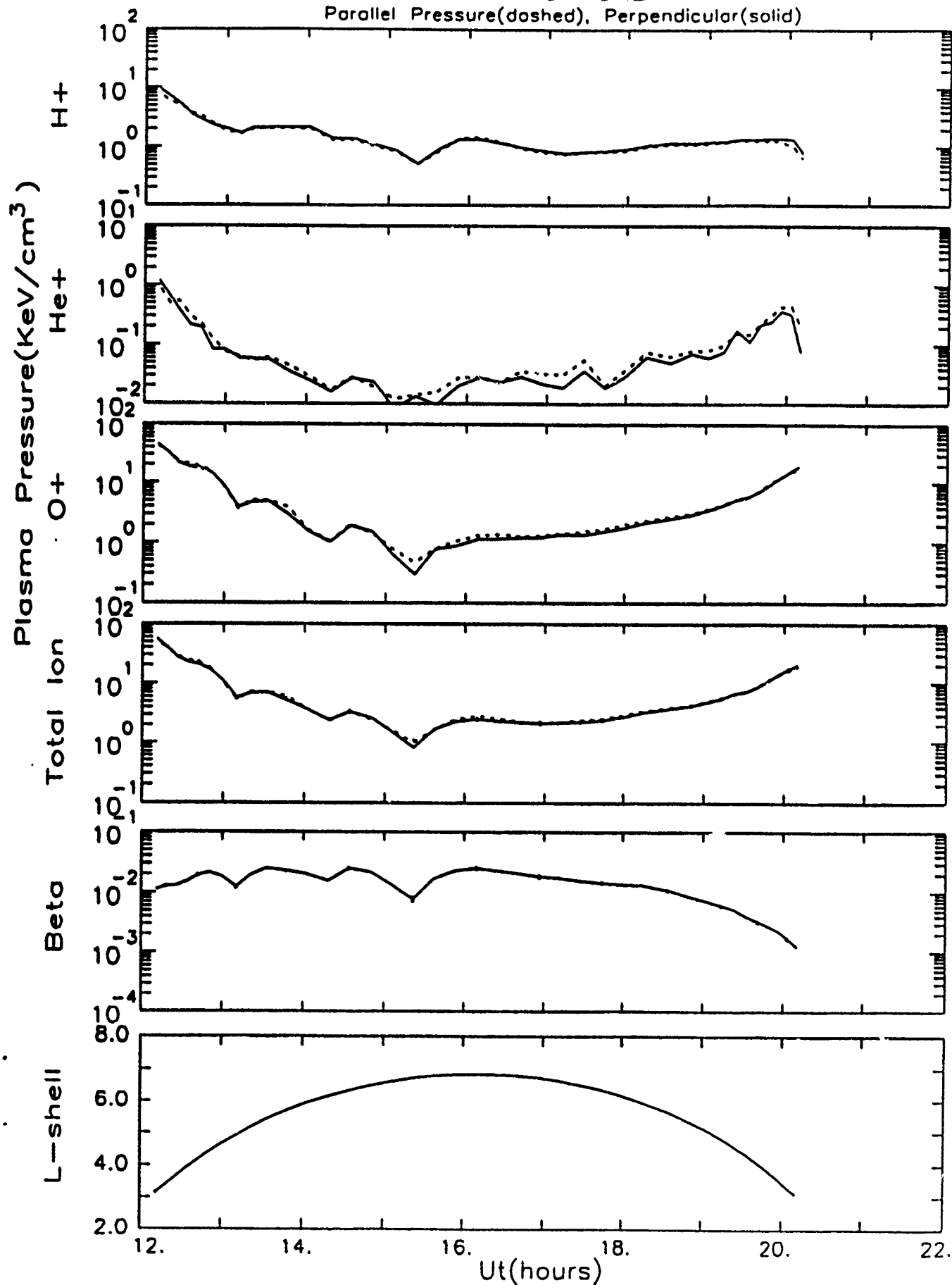


Figure 10c. Perpendicular and parallel pressures of H⁺, He⁺, and O⁺ during orbit 77.

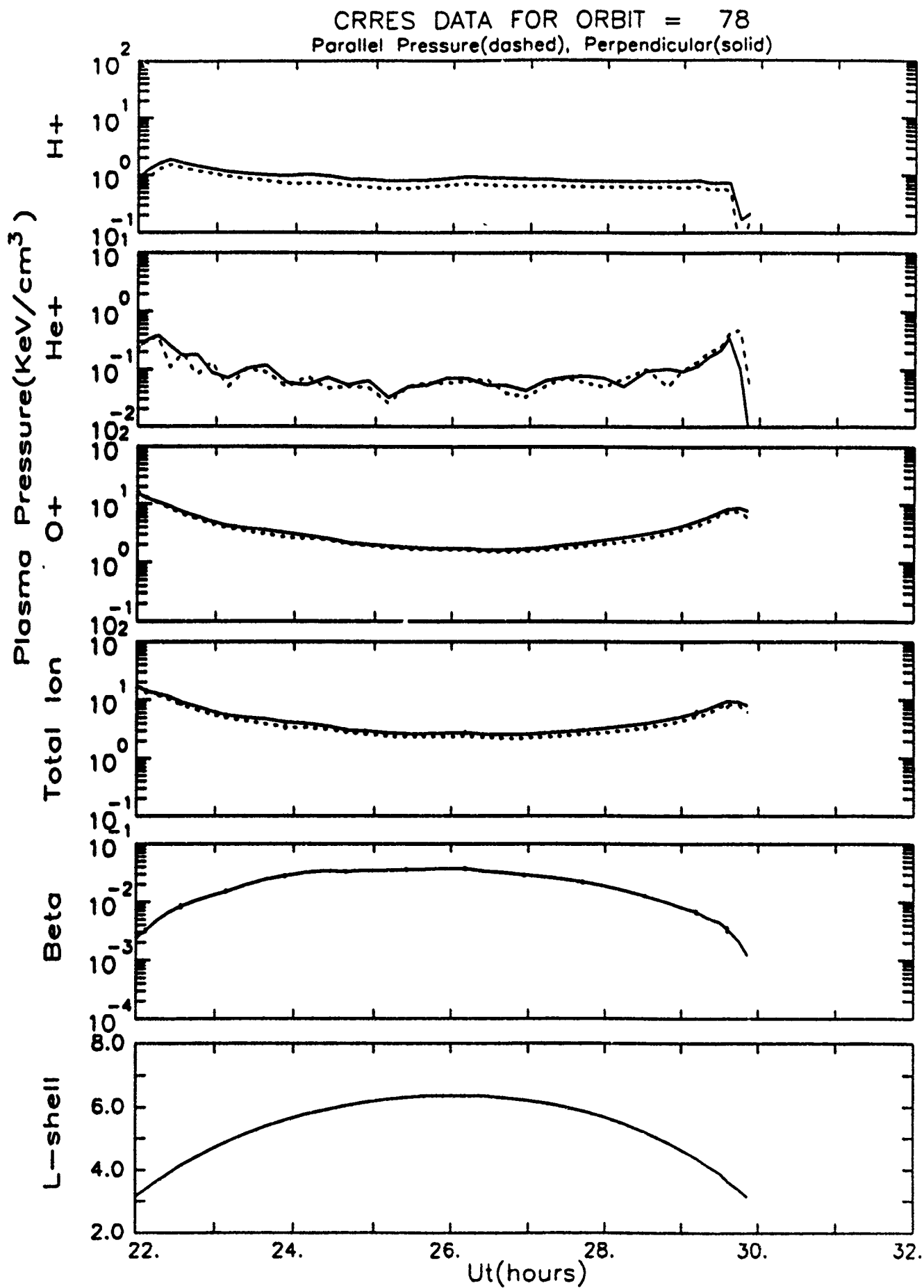


Figure 10d. Perpendicular and parallel pressures of H^+ , He^+ , and O^+ during orbit 78.

CRRES DATA FOR ORBIT = 79
Parallel Pressure(dashed), Perpendicular(solid)

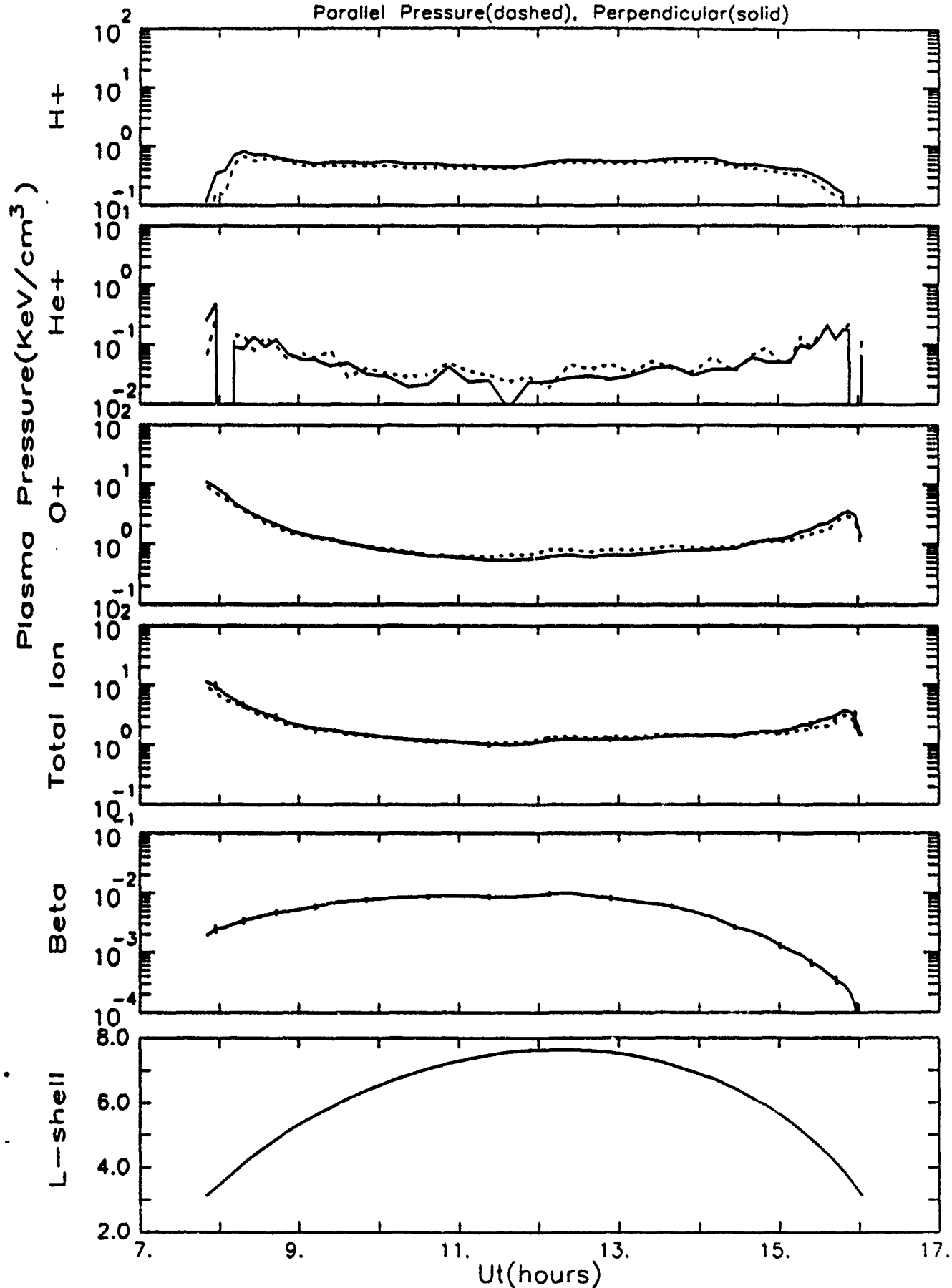


Figure 10e. Perpendicular and parallel pressures of H⁺, He⁺, and O⁺ during orbit 79.

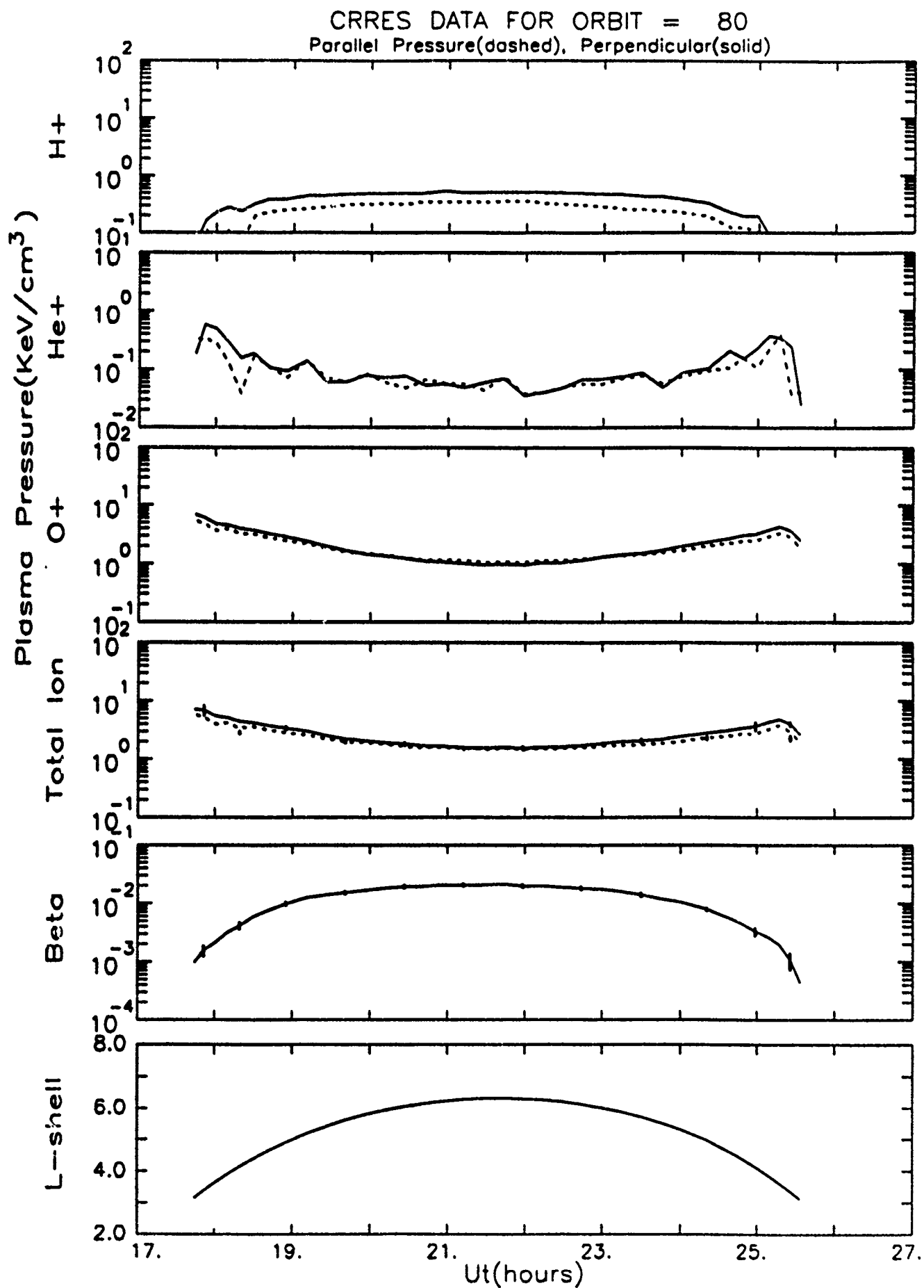


Figure 10f. Perpendicular and parallel pressures of H^+ , He^+ , and O^+ during orbit 80.

CRRES DATA FOR ORBIT = 81
Parallel Pressure(dashed), Perpendicular(solid)

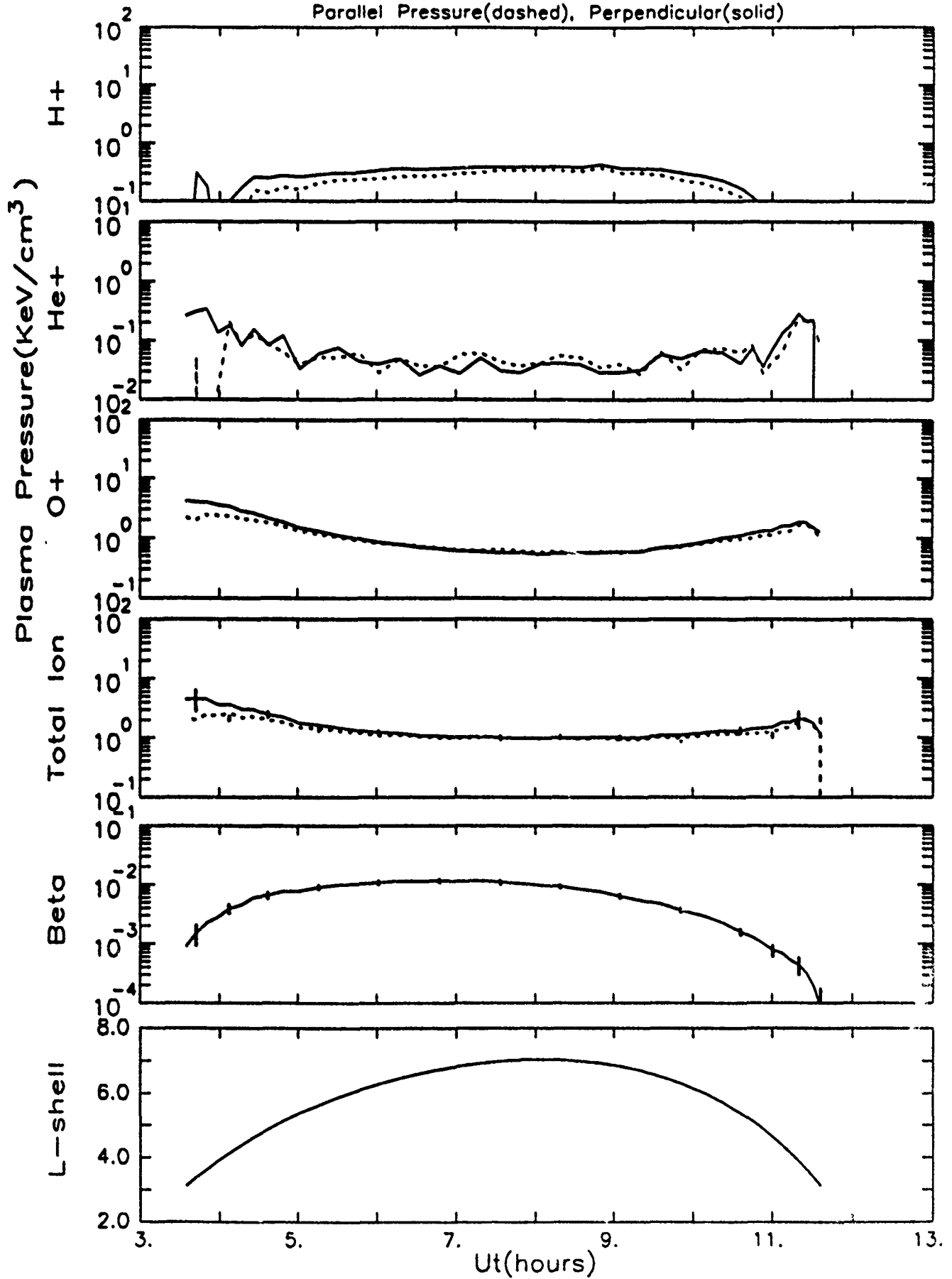


Figure 10g. Perpendicular and parallel pressures of H⁺, He⁺, and O⁺ during orbit 81.

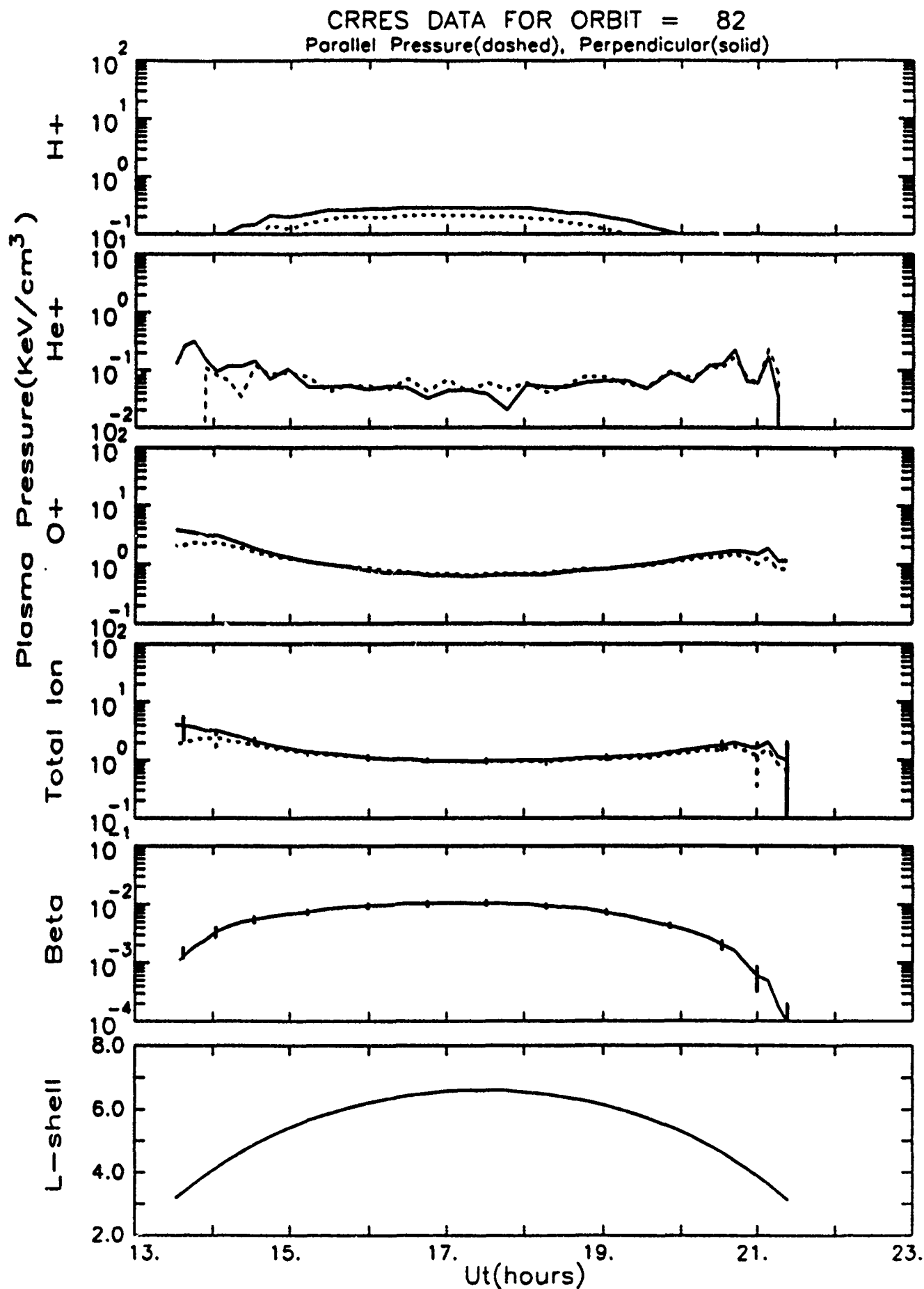


Figure 10h. Perpendicular and parallel pressures of H⁺, He⁺, and O⁺ during orbit 82.

at the lower L values. The He^+ and O^+ fluxes, however, tend to remain fairly isotropic at the higher L values, and the β value generally decreases during the recovery phase of the storm.

3.3.2.3 Interpretation of Data

A tentative interpretation of the IMS-LO data based on the observations described in Section 2.1 is given here. Improved understanding of the pertinent processes is expected after all the CRRES data have been reduced, cross-correlated with CRRES and other (DMSP and Akebono) data sets, and discussed with the various experiments and theorists.

3.3.2.3.1 Ion Sources

Both the southern turning of the IMF and the compression of the magnetosphere at 06:15 UT on orbit 75 indicate an enhancement of magnetospheric convection and the presence of high fluxes of high-density, low-energy ions moving upward along magnetic field lines connected to the cusp/cleft ionosphere. These ions are composed principally of H^+ , He^+ , and O^+ that are accelerated outward from the ionosphere, and H^+ and He^{++} from the magnetosheath that are backscattered and degraded in the upper atmosphere. Those ions with low velocities, near and above the gravitational escape velocity, are efficiently accelerated by the enhanced convection field and transported, within one to two hours, to the near-earth plasma sheet in the nightside magnetosphere [Delcourt et al., 1989; Cladis, 1988].

The increased fluxes of H^+ , He^+ , and O^+ were detected by CRRES at $L \approx 6.3$, 07:30 LT, and 08:00 UT ($1\frac{3}{4}$ hours after the southern turning of the IMF). The pitch-angle and energy distributions of the H^+ are similar to those of H^+ in the plasma sheet, but the distributions of He^+ and O^+ are typical of the ones computed for ions originating in the cusp/cleft ionosphere. Moreover, the observed ions were dispersionless within the time resolution of the flux measurements, so it appears that the ions were rapidly transported inward shortly after the He^+ and O^+ reached the plasma sheet.

The pitch-angle distributions of the O^+ measured at high L values indicate that the local ionosphere, at both ends of the field lines, is an additional source of low-energy ions

(<1 keV). Note that the lowest energy ions have extreme "butterfly" pitch-angle distributions and that the flux increases monotonically from pitch-angles of 90° toward 0° or 180° . Toward higher energies the distributions have maxima that progressively move toward 90° . Hence, it appears that low energy O^+ originate in the local ionosphere and undergo energy diffusion as they move upward along the field lines. He^+ and H^+ are also expected from this ionospheric source, but these ions do not have pronounced "butterfly" distributions at high L values. A possible explanation is that both the pitch-angle and energy distributions of upflowing ions are modified by ion-streaming instabilities.

3.3.2.3.2 Variations of Particle Pressures

As noted earlier the four humps in the pressures of H^+ , He^+ , and O^+ shown in Figure 10c, on orbit 77, are correlated. Specifically the pressures increase and decrease simultaneously, implying that the same process is affecting all the ion species in a similar way. Analysis of the data indicates that three of the pressure humps are due to changes in the compression of the magnetosphere and one is due to an additional plasma injection from the magnetotail.

The first pressure rise begins at about 12:20 UT. Near this time the solar-wind pressure increased, as indicated by the plasma data in Figure 7, such that the nose of the magnetosphere moved inward to about $6 R_E$. CRRES was in the nightside magnetosphere, $MLT \approx 3-4$ hr. Since the inward motion of the nose position causes ions in the nightside magnetosphere to drift outward and the pressure gradient was directed inward, the pressure at the satellite increased.

The next pressure rise, which begins at about 13:20 UT appears to be due to a new injection of ions from the tail. The increased fluxes were detected in the early morning, $MLT \approx 4.6-5.2$ hr, at $L \approx 5-6$, beginning about one hour after the increased compression of the magnetosphere. Such a delay of an hour is consistent with the expected transport time of ions from the dayside cusp/cleft ionosphere to the near-earth magnetosphere. Moreover, inspection of the pitch-angle and energy distributions of the species during this time period, reveals that the fluxes increased monotonically toward lower energies, resembling typical spectra of newly injected ions.

The pressure humps at 14.7 hr UT and 16.2 hr UT appear to be due to decreases in the compression of the magnetosphere. Based on the solar-wind data shown in Figure 7,

the nose of the magnetosphere moved outward to about $8.3R_E$ at 14.7 hr UT and to $10.9R_E$ at 16.35 hr UT. At these times CRRES was on the dawn side of the magnetosphere, at $MLT \approx 6-7$ hr and $L \approx 6.2-6.8$. In this region ions drift outward during a magnetospheric decompression. Hence, the pressure increases since the pressure gradient is directed toward lower L values.

The large depression of the ion pressure centered at about 15.3 hr UT is believed to be due to ion precipitation caused by an induced electric field along the magnetic field. This is a new loss mechanism, which has been identified during the study, and is discussed in the following section.

3.3.2.3.3 A New Loss Mechanism

Inspection of the pitch-angle distributions of the O^+ measured on Orbit 77 from 13:10 UT to 16:16 UT reveals that the flux of ions less than a few keV increases steadily as the pitch-angle increases from near 0° to near 180° . Perhaps the most extreme example, the one measured from 15:14 UT to 15:45 UT in the L interval 6.67-6.81, is shown in Figure 5. Such "clipped-wing butterfly" distributions are not readily explained by known processes.

In Figure 11 are shown two magnetic field lines, projected on the Y-Z plane (geomagnetic solar-magnetospheric (GMS) coordinates), that bound the field lines traversed by CRRES during these measurements. Note that the satellite, depicted by the solid sphere, was in the northern hemisphere, so the ions were principally directed toward the equator. Therefore, an explanation might be that the ions were somehow absorbed and/or scattered downward, along field lines, by instabilities or wave-particle interactions near the equator. However, the time variations of the pitch-angle distributions show that as the flux at high pitch-angles increases the flux at low pitch-angles decreases, and *visa versa*. In Figure 5, for example, the fluxes at $\alpha=150^\circ$ of ions of energy greater than about 4 keV are unusually high while the corresponding fluxes at $\alpha=30^\circ$ are unusually low. The ions behave as though an electric field, modulated in time, is present along the magnetic field line and directed from north to south.

In Figure 12 the two field lines discussed above are projected in the X-Y plane, still in GSM coordinates. the field lines appear as they do in this plane because the dipole tilt angle was equal to about 20.5° at the times of these measurements. Now, note in Figure 8b that the B_z (actually B_H) component of the magnetic field measured on CRRES during

FIELD LINE TRACE (TSYGANENKO) 1987 LONG MODEL
 TIME=08:50:40, DATE=17-MAY-91
 THE X,Y,Z COORDINATE SYSTEM IS: MAGNETOSPHERIC
 KP= > 5 , EPOCH(Y:M:D:H:M:S)=90: 8:26:15:22:40:
 FIELD LINE IN (Y,Z) PLANE, DIPOLE TILT= 20.5 DEG.

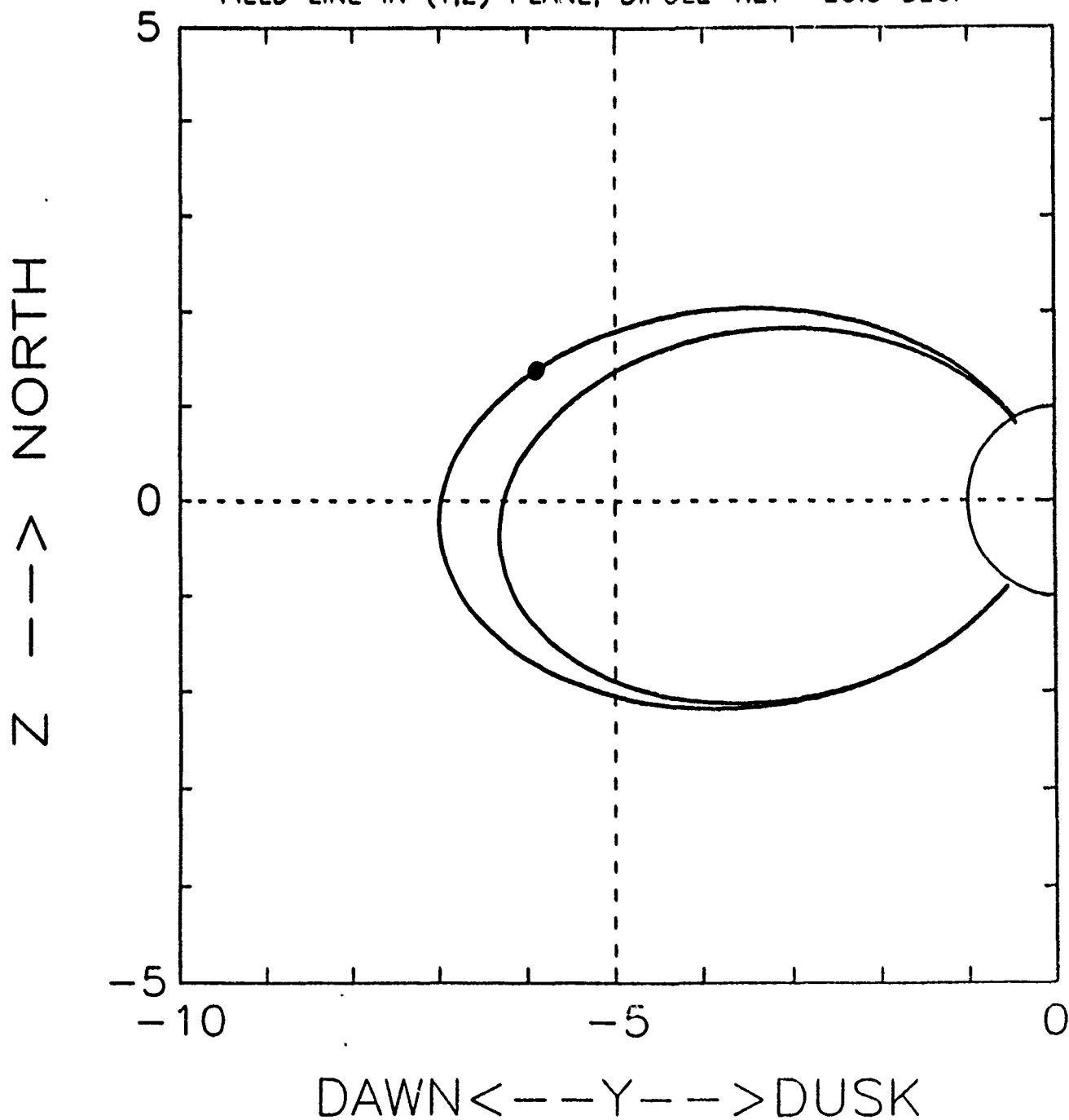


Figure 11. Magnetic field lines on which "Clipped-wing butterfly" distributions were observed. In GMS coordinates.

FIELD LINE TRACE (TSYGANENKO) 1987 LONG MODEL
 TIME=08:50:40, DATE=17-MAY-91
 THE X,Y,Z COORDINATE SYSTEM IS: MAGNETOSPHERIC
 KP= > 5 , EPOCH(Y:M:D:H:M:S)=90: 8:26:15:22:40:
 FIELD LINE IN (X,Y) PLANE, DIPOLE TILT= 20.5 DEG.

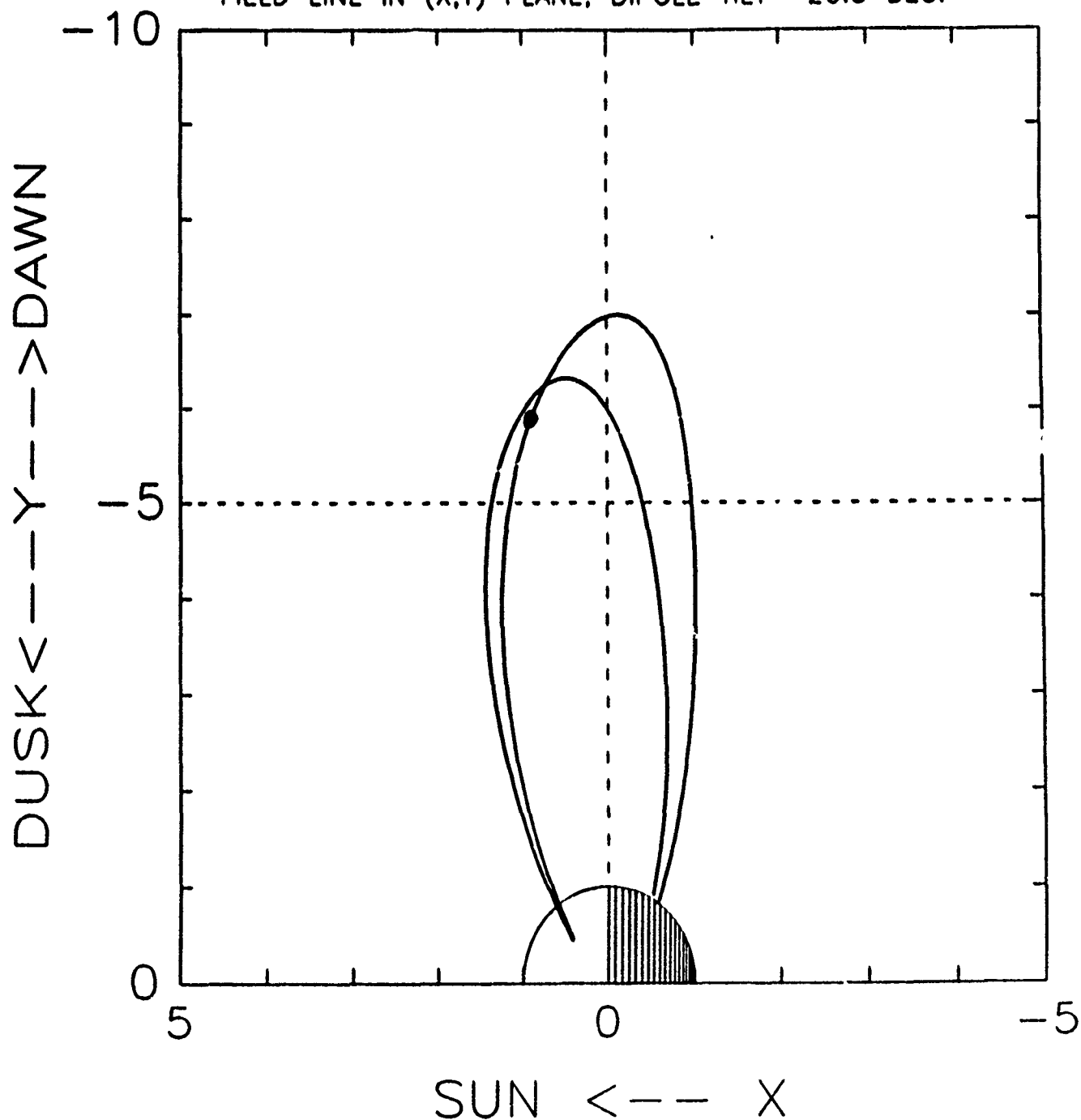


Figure 12. The magnetic field lines of Figure 11 projected into the X,Y plane.
 In GMS coordinates.

this period, from about 13.2 hr UT to about 16 hr UT, was fluctuating appreciably but also generally increasing with time over the modeled magnetic field strength. After converting the magnetic field to GSM coordinates and assuming B_z to increase linearly from 13.5 hr to 15.7 hr UT, then $dB_z/dt \approx 7.6 \times 10^{-3}$ nT/s over this time period. If this rate is taken to be uniform over a volume extended along the Z_{GSM} axis and enclosed by the field line on which the solid sphere (CRRES) is located in Figure 12, then the induced electric potential over that field line, neglecting the presence of the earth, would be $\psi = |AdB_z/dt|$, where A is the area enclosed by the field line projected on the X-Y plane. The area A may be taken to be elliptical with semiaxis a and b equal to 1.1 and $3.5R_E$, respectively. Then $A = \pi ab$, and ψ is about 3.7 keV. The potential drop in the ionosphere between the ends of the field line may be neglected. So the potential drop along the field line from the northern to the southern hemisphere would be of the order of 4kV. On the average, the observations are consistent with a potential difference of about 1kV.

The pitch-angle distributions of the H^+ and He^+ do not exhibit such pronounced "clipped-wing" distributions. In this respect the pitch-angle distributions are similar to those of ions of different species that flow upward from the ionosphere. So here too the pitch-angle distributions of all the "field aligned" ion species may be affected by ion streaming instabilities.

Although the proposed mechanism is promising, based on the analysis of this single event, additional events of this type must be examined to verify the mechanism. The data imply ion precipitation in the southern hemisphere, so we have been seeking measurements to test this feature. Using the Akebono ephemeris, which we acquired from NSSDC, we found that that satellite was very near an appropriate location and time to detect the precipitating ions. It was moving toward the south pole on Day 238 1990, and at 16.5 hr UT, it was at $L=6.58$, $MLT=6.77$ hr, and altitude=1868 km. We have written to Mukai, inquiring whether he obtained measurements at that time, but he has not yet replied. If this explanation of the "clipped-wing" distributions is correct, such distributions should occur near dawn or dusk whenever the magnetosphere is being compressed or decompressed while the dipole tilt angle is appreciable. During the first compression of this magnetic storm, the dipole tilt angle was about zero and "clipped-wing" distributions were not observed.

4 Future plans

Agency tape processing, the generation of the high resolution data base, the survey plot library, and the summary data base will be continued on the SUN on a routine basis.

Cross calibration of IMS-LO with other plasma instruments will continue. The unexpected revival of LOMICS has made it possible follow our original intention to cross calibrate with that low energy mass spectrometer. However we will continue to cross calibrate with LEPA. Since LEPA does not separate ion species it will be necessary to select data from periods which are dominated by a single ion species as well as meeting other necessary criteria. We will also attempt to cross calibrate with MICS since there is sufficient overlap between the energy ranges of IMS-LO and MICS.

The preliminary version of the empirical model of ring current ion composition will be constructed.

The distribution functions of low-energy ions (<35 keV) measured during quiet times will be used to estimate the quiet-time electric field in the magnetosphere, using Liouville's theorem to test electric field models along ion drift paths between successive CRRES passes through the trapping region. As time permits, this analysis will progress to more disturbed periods. Further examples of "clipped-wing" pitch-angle distributions will be sought and the validity of the new loss mechanism described in section 3.3.2.3.3 will be investigated.

References

- Cladis, J. B., "Transport of ionospheric ions in the magnetosphere: Theory and observations", *Adv. Space Res.*, 8, (8)165, 1988.
- Delcourt, D. C., C. R. Chaprell, T. E. Moore, and J. H. Waite, Jr., "A three-dimensional numeric model of ionospheric plasma in the magnetosphere", *J. Geophys. Res.*, 94, 11893, 1988.
- Gloeckler, G., B. Wilken, W. Studemann, F. M. Ipavitch, D. Hovestadt, D. C. Hamilton, and G. Kremser, First composition measurement of the bulk of the storm-time ring current (1 to 300) keV/e with AMPTE/CCE, *Geophys. Res. Lett.*, 12, 325, 1985.
- Kozyra, J. U., T. E. Cravens, A. F. Nagy, E. G. Fonthelm, and R. S. B. Ong, Effects of energetic heavy ions on electromagnetic ion-cyclotron wave generation in the plasma-pause region, *J. Geophys. Res.*, 89, 2217, 1984.

Williams, D, J, Ring current and radiation belts, *Rev. Geophys.*, 25, 570, 1987.

Wrenn, G. L., Persistence of the ring current, 1958-1984, *Geophys. Res. Lett.*, 16, 891, 1989.

Appendix 1

The Low Energy Ion Mass Spectrometer (ONR 307-8-1,2)

The Low Energy Ion Mass Spectrometer (ONR-307-8-1,2) on CRRES

H. L. Collin*, J. M. Quinn†, G. R. Smith‡, E. Hertzberg§, S. Roselle¶,

S. J. Battel**

*** Research Scientist, Lockheed Palo Alto Research Laboratory, Palo Alto, CA 94304.**

† Staff Scientist, Lockheed Palo Alto Research Laboratory, Palo Alto, CA 94304.

‡ Senior Scientist, Lockheed Palo Alto Research Laboratory, Palo Alto, CA 94304.

§ Staff Engineer, Lockheed Palo Alto Research Laboratory, Palo Alto, CA 94304.

¶ Senior Engineer, Lockheed Palo Alto Research Laboratory, Palo Alto, CA 94304.

**** Consultant, Member AIAA, Battel Engineering, 7601 N Calle Sin Envida #62, Tucson, AZ 85718.**

Scientific Objectives

The Low Energy Ion Mass Spectrometer (IMS-LO) is part of the SPACERAD [1] payload on the CRRES [2] satellite. IMS-LO is designed to measure the composition of plasmas which are the sources of radiation belt particles, and to provide data on the origin and acceleration processes of these plasmas. In order to achieve these objectives, the instrument measures energy and mass spectra covering the ranges of $E/q = 0.11 - 35 \text{ keV/e}$ and M/q from $1 - 32 \text{ AMU/e}$ with good coverage of pitch angles throughout the CRRES orbit.

Measurement Techniques

The IMS-LO-1,2 instruments on CRRES rely upon essentially the same design that was successfully implemented with previous Lockheed instruments on SCATHA (launched January 1979) and S3-3 (launched July 1976). Improvements have been made with each version of the instrument in range of coverage, resolution, and operating flexibility.

IMS-LO-1 and IMS-LO-2 are identical instruments which are mounted on the aft surface of the spacecraft with their look directions at 135° and 105° to the spacecraft $+Z$ axis. In the spacecraft X-Y plane they are both at 45° from the $+X$ axis, clockwise viewing in the $+Z$ direction. CRRES spins about the Z axis with $+Z$ oriented sunward. The look directions of the instruments were chosen to maximize coverage of fluxes near the magnetic field line direction throughout the mission. Each instrument performs ion composition measurements in the energy per charge range $0.11-35 \text{ keV/e}$ and the mass per charge range $1 - 32 \text{ AMU/e}$. The energy range, which is covered by 45 energy steps, is broken into three contiguous parts ($j = 0, 2$), each consisting of 15 energy steps ($i = 0, 14$). The mean energy per charge (E_{ij}) of ions on the i^{th} step of the j^{th} part is given by

$$E_{ij}(\text{keV}) = 0.109 \times (1.14008)^{(i+15j)} \quad (1)$$

The three parts of the energy coverage are sampled in parallel by three separate analyzer and sensor units ("heads"). At the completion of each 15 step sequence, the background counting rate is measured for each sensor head. The mass range ($1 - 32 \text{ AMU/e}$) is covered by 32 steps. Alternatively, the spectrometer can be commanded to a Heavy Ion Mode as described in the section on Operating Modes and Control. In addition to ion measurements, each of the two instruments monitors the background electron flux at four fixed energies. The electron channels are described in a separate section below.

Ion Optics

Each of the IMS-LO mass spectrometers consists of three analyzer heads which measure ions in a different portion of the E/q range from $0.11-35 \text{ keV/e}$. One of the analyzer heads is illustrated in Figure 1. Each analyzer consists of four sections, a collimator, a velocity filter, an energy analyzer and a channel electron multiplier detector.

Ions enter the instrument through the collimator which provides an acceptance cone of approximately 5° full width. Following collimation, the ions enter the crossed electric and magnetic field velocity filter (Wien Filter), which acts as the mass analyzer (MA). Its magnetic field is fixed while the crossed electric field is varied according to the value of E/q

and M/q being sampled. The fields are oriented so that the electric and magnetic forces on an ion are in opposition, and the electric field is chosen so that there is no net force on an ion of the desired mass and energy, allowing it to pass through the MA in a straight trajectory. The MA magnetic fields in the three heads are nominally 445, 1211, and 3304 Gauss. The electric field plates of the MA are driven symmetrically and the voltages for a given mass selection scale as the square root of the ion energy which is determined by the voltage applied to the electrostatic analyzer. The maximum MA plate potentials in the three heads, corresponding to the minimum ion mass and the maximum energy per charge sampled by head, are nominally, ± 35 , ± 253 , and ± 1850 V for the normal mass range and a factor of four lower for the heavy ion mode. All three heads are driven by a common high voltage power supply and a divider network which provides the different ranges required.

Following the velocity filter, ions are bent 180° in a hemispherical sector electrostatic analyzer (EA) which is angle focusing and energy dispersive. As with the MA, the EA plates in all three heads are driven by a common power supply and a divider network. The ratio between consecutive values of the logarithmically spaced energy steps is approximately 1.14, and there are 15 energy steps assigned to each head. Thus the energy per charge being simultaneously sampled by the three heads are spaced by a factor of approximately 1.14, with the first head covering from 0.11-0.68 keV/e, the second from 0.78-4.9 keV/e, and the third from 5.6-35 keV/e. The EA plate separation in the high energy head is reduced from that of the other two heads in order to achieve the desired energy range without the need for excessively high voltages. After exiting the EA, ions are post-accelerated by 1kV, to improve detection efficiency, and enter the channel electron multiplier detector.

The stepping of the EA and MA is coordinated under digital control in a number of modes as described in the following section. Each sample of a particular mass-energy value takes 64 ms. There is a 12 ms deadtime at the beginning of each sampling period to ensure complete settling of the analyzer power supplies, even in the worst-case transitions.

In addition to the energy steps described above, there is an additional setting in which each of the three heads measures background counts. The background measurement is performed by disabling the MA power supply and setting the EA power supply to step 4. As the MA power supply decays toward zero, the analyzers pass continually higher masses. Following the 12 ms deadtime, the background channel is sampling mass per charge values well above those of ambient ions and measures the instrument background response only.

Electron Detectors

Each of the IMS-LO instruments contains a set of four broadband, fixed-energy electron detectors, Figure 2, which are used to monitor electron fluxes between 50 eV and 25 keV. Electrons entering one of these instruments are collimated to a 5° acceptance cone and pass through an aperture which sets the geometric factor. The electrons are then bent 180° in a magnetic analyzer and pass through an exit aperture which sets $\Delta E/E$ before entering the channeltron sensor. The $\Delta E/E$ for each detector is 50% and the central energies of the electron channels on IMS-LO-1 and IMS-LO-2 are interleaved, providing a total of eight channels with central energies from 0.067 to 20 keV. The electron detectors accumulate for 512 ms, providing samples approximately every 6° of spacecraft spin.

Operating Modes and Control

There are two basic submodes of operation of the mass spectrometers; SWEEP and LOCK. Each of these submodes takes 32.768 seconds to complete, approximately one spacecraft rotation.

The LOCK submode maximizes resolution in time and pitch-angle by concentrating on selected masses. The instrument is locked on the selected mass per charge while stepping in energy. Each energy step and background are sampled for 64ms and the three sensor heads together acquire a 45 point energy spectrum in 1.024 seconds, approximately 12° of spacecraft rotation. In the LOCK submode 32 consecutive energy spectra are acquired at the selected mass before the instrument moves into the next submode.

The SWEEP submode examines the mass spectrum in more detail but with reduced resolution in time and pitch-angle. In this submode the instrument acquires a mass spectrum at each energy step by sweeping through all 32 mass steps while the energy is held steady. Each mass step is sampled for 64ms and a full mass spectrum is acquired in 2.084 seconds. The complete mass-energy spectrum, 32 mass steps at each of 45 energy steps together with 32 background measurements, is acquired in 32.768 seconds.

Eight submodes are combined to form the three basic modes of operation; LOCK-ONLY, SWEEP-ONLY, and SWEEP-LOCK. As the names imply, LOCK-ONLY consists of LOCK submodes only, SWEEP-ONLY is composed of SWEEP submodes, and SWEEP-LOCK alternates between SWEEP and LOCK. In either the LOCK-ONLY or SWEEP-LOCK modes, the mass steps used in the LOCK submode are taken sequentially from four values which are held in the instrument memory. These values may select any four of the 32 M/q steps and correspond to any four ion species; for instance, H^+ , He^+ , He^{++} , O^+ ; or H^+ , O^+ , H^+ , O^+ . IMS-LO-1 and IMS-LO-2 are commanded independently so that it is possible to have the two instruments operating in different modes simultaneously. The operating mode and LOCK mode mass steps can be selected by command. Initially, both instruments were operated in the SWEEP-SWEEP mode while their performance was assessed and on orbit measurements of mass peak shapes were made. Subsequently both instruments were commanded into the SWEEP-LOCK mode with the LOCK mode steps set for H^+ and O^+ .

In addition to the normal range of mass coverage, the instrument can be commanded into a Heavy Ion Mode for use during chemical release experiments. In this mode, the MA and EA voltages are reduced by a factor of six, scaling the M/q coverage upward and the energy downward to give an operating range of 5 - 250 AMU/e and 0.02 - 5.8 keV. During barium releases one of the instruments has been operated in the Heavy Ion SWEEP-LOCK mode to search for Ba^+ . When lithium releases were made one of the instruments was operated with the LOCK mode steps set to for Li^+ . The other instrument remained in the normal mode of operation to continue to monitor ambient plasma.

The discriminator threshold for each detector is set by command to one of four values. A special calibration cycle will be commanded periodically which locks on a selected mass step and sequentially steps through the thresholds in order to monitor the channel electron multiplier gain. In addition, the calibration command may optionally enable pulses at a known rate to monitor performance of the signal processing electronics. The channel

electron multiplier bias is command selectable to one of four values to compensate for possible channel multiplier gain degradation over the life of the mission.

Calibration

A good understanding of the characteristics of the mass spectrometers' response to ambient ions is necessary in order to correctly interpret the data it obtains, to optimize its operating modes and to determine the correct ratios for the EA and MA voltage divider networks.

Three approaches were used which provided complimentary information on the spectrometers' characteristics. During the design phase, detailed ray tracing studies provided a baseline description of the variation of the mass spectrometers' response to ions' energy, mass and approach direction.

The flight instruments were individually calibrated in the Lockheed Palo Alto Research Laboratory mass spectrometer calibration facility in which they were exposed to monoenergetic beams of selected ion species. The detailed energy-mass response of each spectrometer head was investigated at a number of representative energies. At each energy an ion beam of H^+ or Ne^+ at the selected energy was directed at the instrument and the EA and MA voltages varied in small increments to provide a dense mesh of measurements to characterize the response function.

Since the full response is dependent on approach angle and incidence position, as well as energy and mass, it was not practical to perform the huge number of individual measurements that would be needed with a monoenergetic beam in order to fully characterize all of the spectrometers' 45 energy steps. Instead, during an on orbit calibration procedure, ambient ring current ions were utilized as a multi-ion isotropic extended energy source which could be relied upon to fill the field of view of the spectrometer. With the instruments in SWEEP mode mass spectra were acquired at all energy steps. These measurements provided relative response functions for common mass species at all energy steps. Figure 3 shows peak shapes obtained in this way near the middle of the head's energy range. The dashed lines represent inferred peak shapes while the marks show on-orbit data. Mass resolution in this type of instrument is dependent on mass and energy. The $\Delta M/M$ is lowest for H^+ at the low energy of each head and increases with increasing energy and mass. At the middle of the energy range $\Delta M/M = 0.15$ for H^+ and $\Delta M/M = 0.35$ for O^+ . In the Heavy Ion Mode $\Delta M/M = 0.16$ for Li^+ and 0.47 for Ba^+ .

The acceptance angle is approximately conical with a full width at 50% sensitivity of 5° . The 30s satellite spin period results in a movement of the instrument of less than one degree during the 64ms sample time. The instrument geometric factors are $4 \times 10^{-4} \text{ cm}^2 \text{ ster}$ and $\Delta E/E$ of $\approx 10\%$ for the two lower energy heads. The narrower EA plate separation in the high energy heads results in a geometry factor of $2 \times 10^{-4} \text{ cm}^2 \text{ ster}$ and $\Delta E/E$ of $\approx 5\%$.

The characteristics of IMS-LO are similar to those of its predecessors on S3-3 and SCATHA but it differs from the ion mass spectrometers on some other magnetospheric satellites such as ISEE-1, DE-1, and AMPTE/CCE. The sensitivity of these instruments [3] is substantially constant over their energy range, but their field of view and $\Delta E/E$

increase substantially at low energies whereas the sensitivity of IMS-LO is proportional to energy and its field of view and $\Delta E/E$ are constant.

Data Reduction

The IMS-LO instruments completed their initialization sequence and began normal operations on August 4th 1990. They are operating well and returning good quality data. Figure 4 displays an example of summary plot data from one of the spectrometers. The summary plots provide an excellent overview of a whole orbit and display mass and energy spectra and pitch-angle distributions as a function of time. For these plots the data have been averaged over 262s intervals. The upper panel shows mass spectra from the highest energy analyser. This contains horizontal bands near the bottom and top which correspond to H^+ and O^+ respectively. Two faint intermittent bands corresponding to He^+ and He^{++} can also be distinguished. The next two panels show energy spectra of H^+ , and O^+ . The lower two panels display the pitch-angle distributions of H^+ and O^+ . For each of these the flux has been sorted into 10° pitch-angle bins.

Acknowledgments

The authors wish to express their appreciation to D. A. Simpson, A. L. Magoncelli, J. C. Bakke, L. A. Hooker, V. F. Waltz and T. C. Sanders for their efforts in the design, development and fabrication of this instrument. We are also deeply indebted to our co-investigators, R. G. Johnson, R. D. Sharp, A. G. Ghielmetti, R. R. Vondrak, and especially, E. G. Shelley for making this instrument (and its predecessors) possible. This effort was supported by the Office of Naval Research under contract N00014-83-C-0476, by the Lockheed Independent Research Program and part of the data analysis was supported by the USAF Phillips Laboratory under contract F19628-90-C-0119. We would like to express our appreciation to Ball Aerospace Systems Division who built CRRES; to General Dynamics whose Atlas-Centaur rocket put it into orbit; to the USAF Space Test Program and NASA Marshall Space Flight Center who together managed the project; and to the USAF Consolidated Space Test Center who operate the satellite, for their contributions to the success of the ONR 307-8-1,2 experiment.

References

- [1] Gussenhoven, S., and Mullen, E. G., "Space Radiation Effects Program," *Journal of Spacecraft and Rockets*, Vol. 28, November-December 1991, pp
- [2] Johnson, M. H., and Kierein, J., "The Combined Release and Radiation Effects Satellite (CRRES): Spacecraft and Mission," *Journal of Spacecraft and Rockets*, Vol. 28, November-December 1991, pp
- [3] Shelley, E. G., Ghielmetti, A., Hertzberg, E., Battel, S. J., Altwegg-Von Burg, K., and Balsiger, H., "The AMPTE/CCE Hot-Plasma Composition Experiment (HPCE)," *IEEE Trans. Geosci. Remote Sensing*, Vol GE-23, p. 241, 1985.

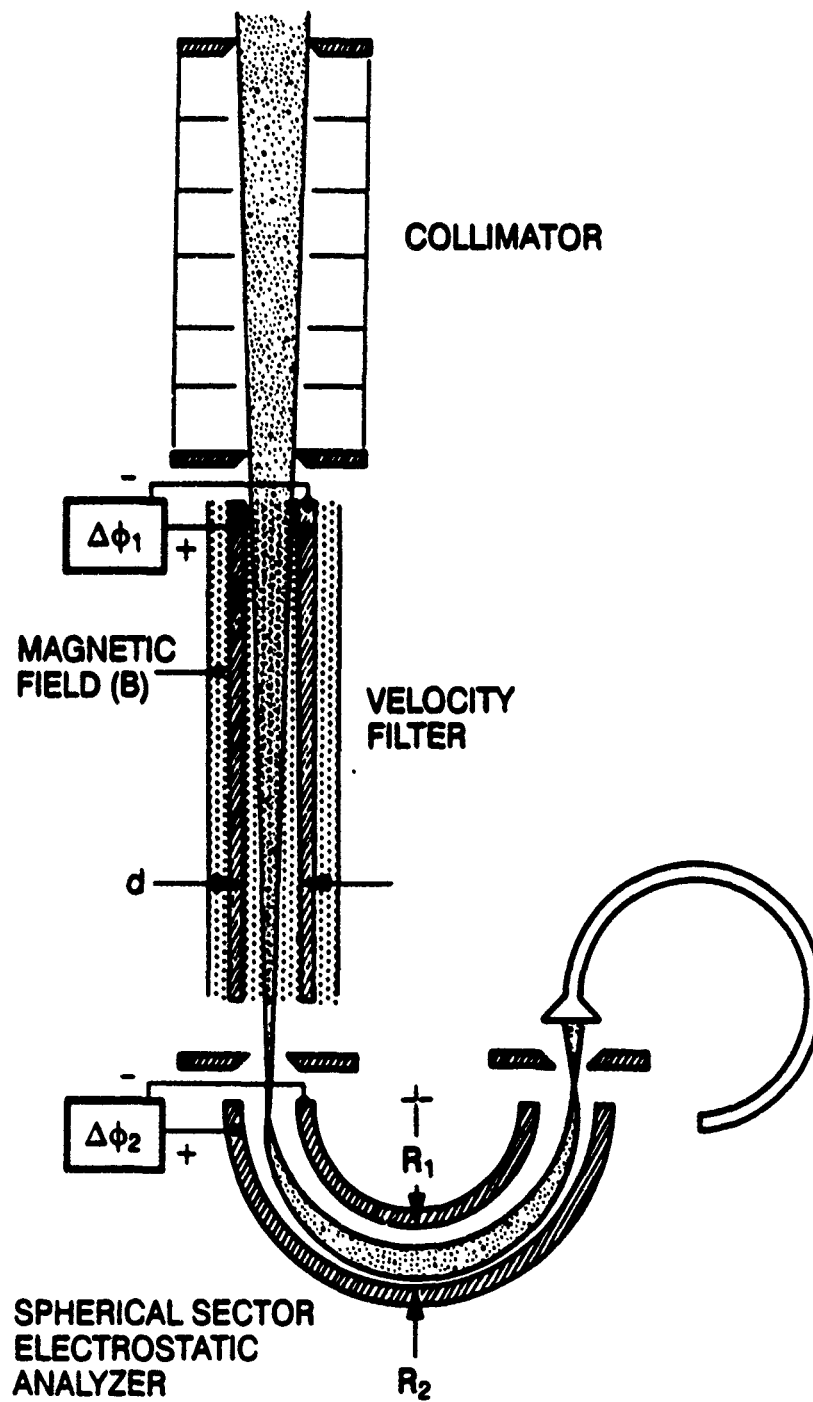


Figure. 1. Ion mass and energy analysis optics for the Low Energy Ion Mass Spectrometer.

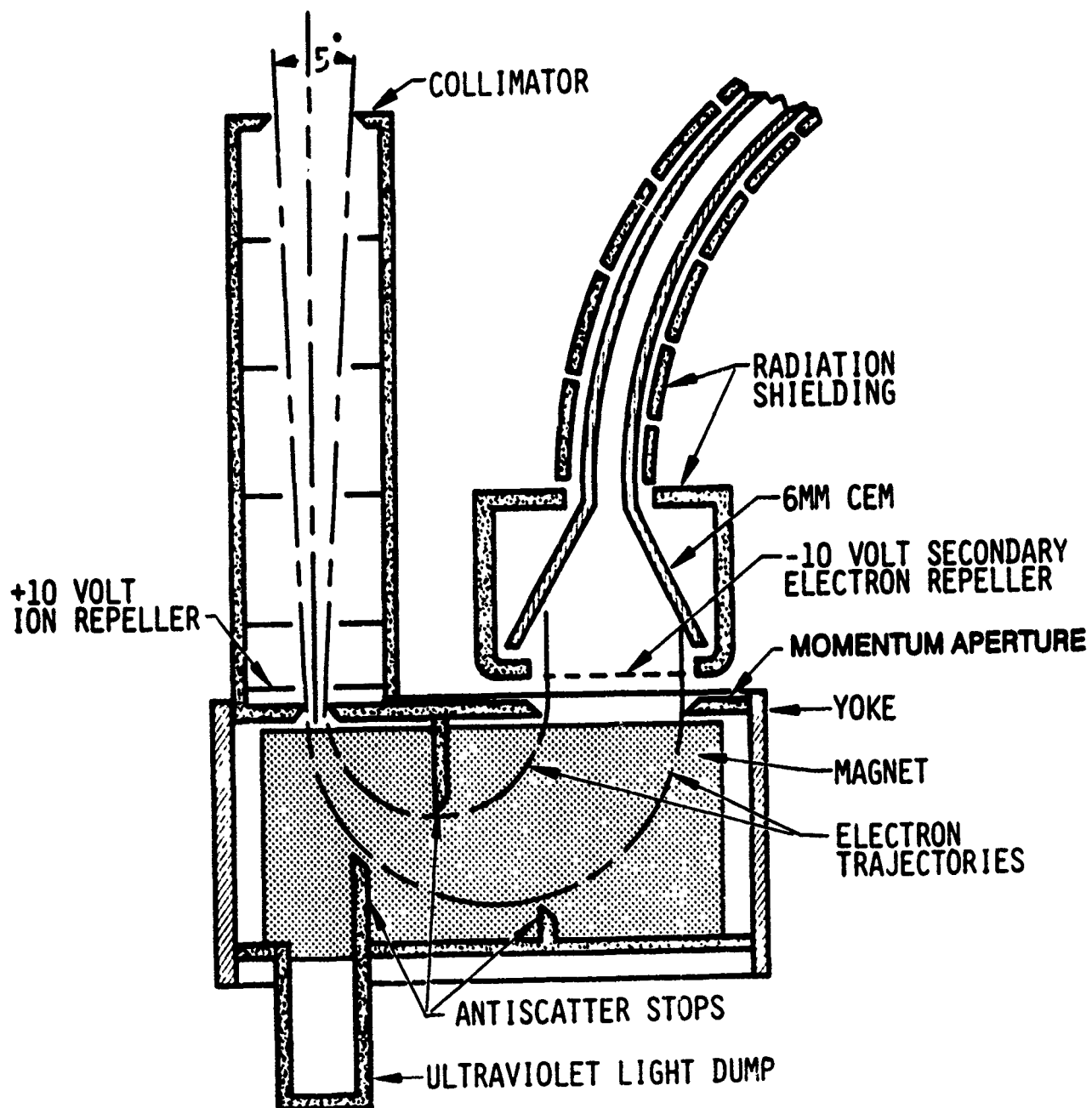


Figure. 2. Schematic of a single magnetic electron analyser.

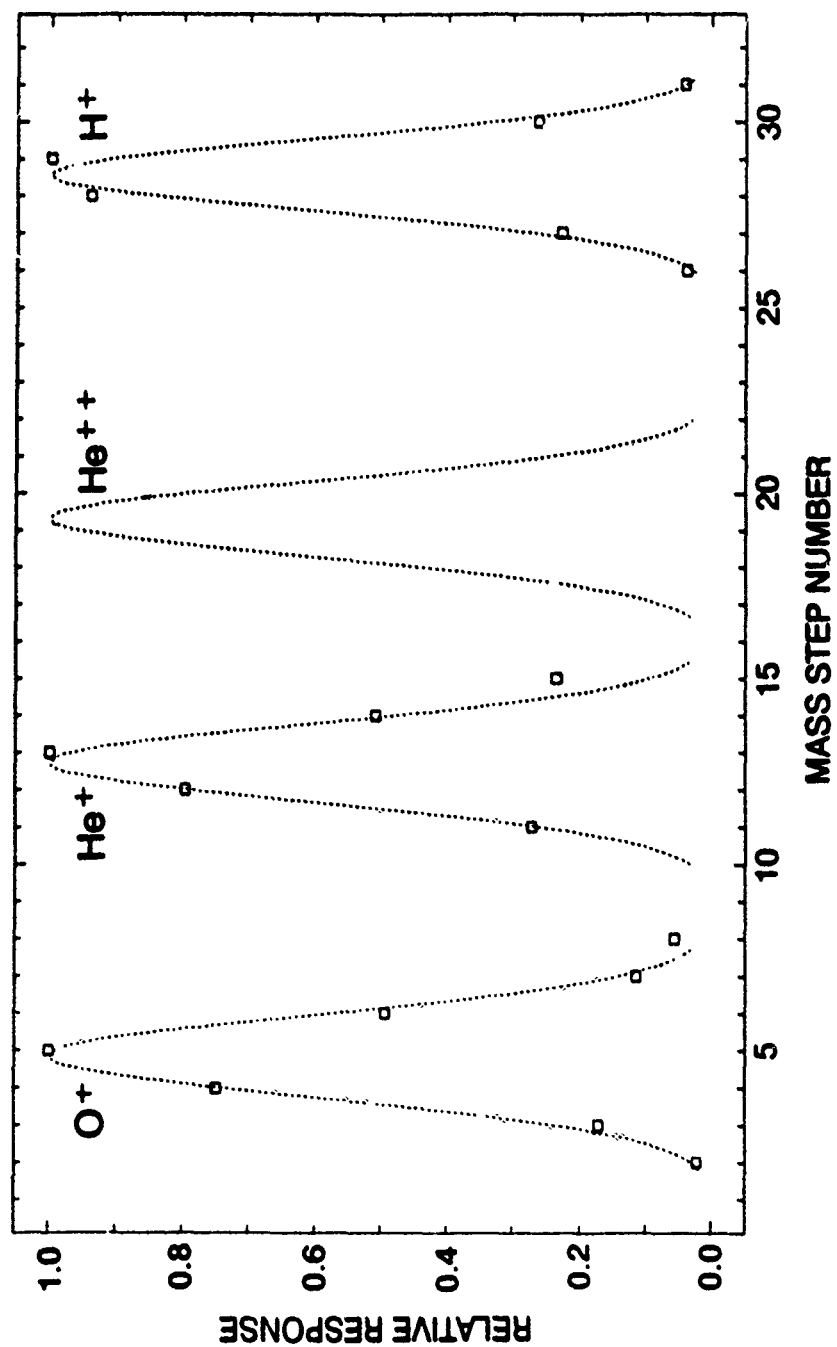


Figure. 3. Mass peak shapes at a representative energy step, from on orbit data.

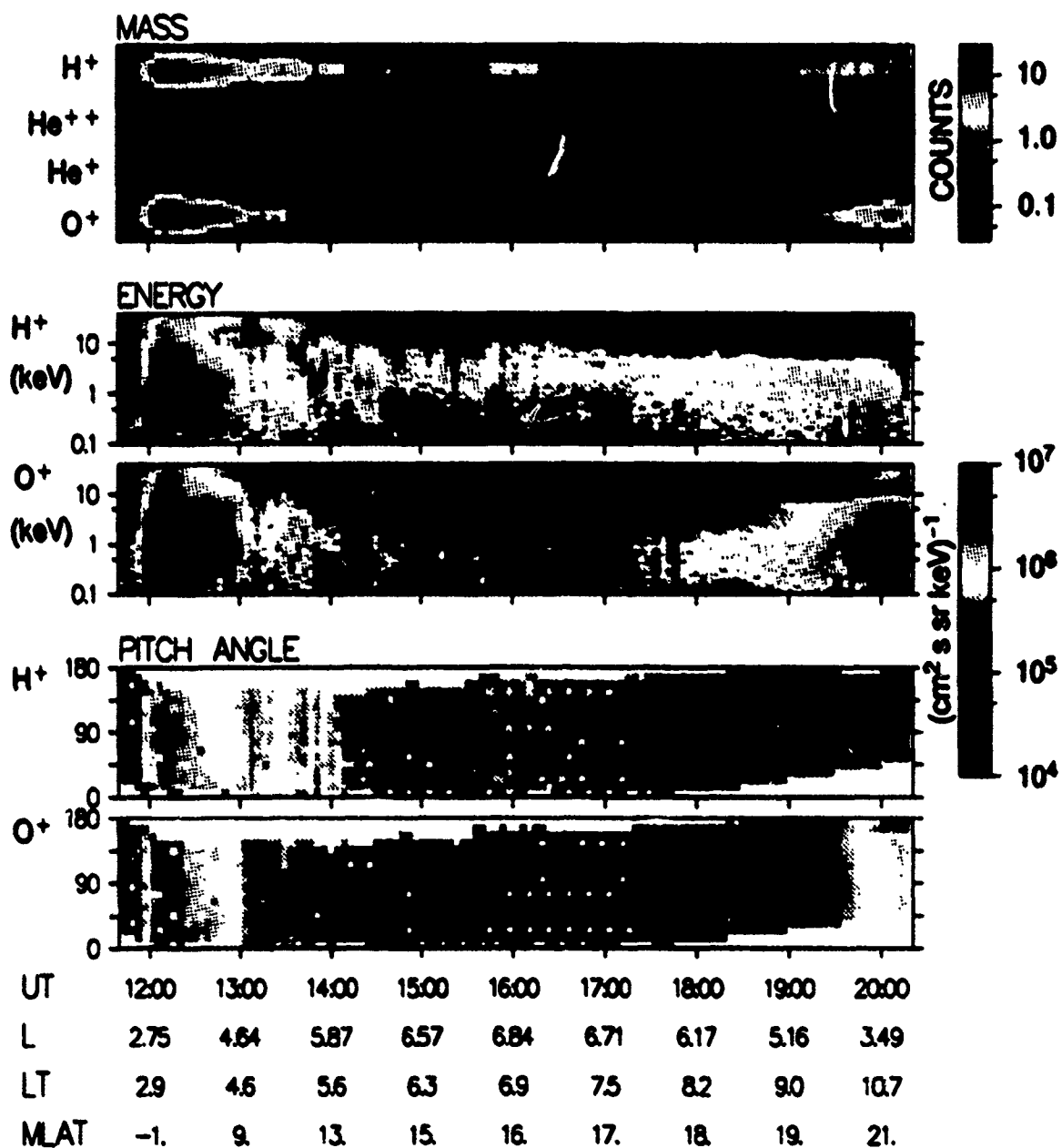


Figure. 4. Summary plots of data from one ion mass spectrometer.

Appendix 2

Abstracts of Papers Presented

**Low Energy Ring Current Ions During the Storm of 26 August
1990: Observations by IMS-LO on CRRES**

**H L Collin, J M Quinn, and J B Cladis (Lockheed Palo Alto
Research Laboratory, 3251 Hanover St., Palo Alto, CA 94304)**

During the storm of 26 August 1990, about two hours after a sudden commencement which occurred at 0547 UT, enhanced fluxes of H^+ , He^+ and O^+ at energies between 110 eV and 35 keV were detected by the Lockheed Ion Mass Spectrometer on the CRRES satellite at 0803 MLT and $L \approx 6.4$. These enhanced fluxes persisted for about three days. The orbit of CRRES enabled measurements of the ions to be made repeatedly in the region $3.0 \leq L \leq 6.5$ and $0300 \leq MLT \leq 1030$. The time sequence of ion observations shows the development and decay of the low energy ion component of the plasma in the ring current region and show evidence of multiple particle injections and ion acceleration.

Storm-Time Dynamics Implied by CRRES

Measurements of Ring-Current Ions

J.B. Cladis, H. L. Collin, and W. E. Francis, (all at Lockheed Missiles and Space Co., Palo Alto, California 94304)

On 26 August, 1990, a sudden commencement occurred at 0543 UT and sharply enhanced fluxes of H^+ , He^+ , and O^+ ions were detected with the Lockheed Ion Mass Spectrometers, IMS-LO and IMS-HI, on the CRRES satellite at 0800 UT, $L \approx 6.38$, and 0803 MLT. The enhanced fluxes were observed for several orbits in the region $3.2 \leq L \leq 6.8$ and $0300 \leq MLT \leq 1030$. Multiple particle injections, ejections, and field-aligned acceleration events are implied by the data. The distribution functions of ions that contribute importantly to the energy density of the ring current were used to compute the ion pressures parallel and perpendicular to the magnetic field, as well as the plasma β (the ratio of the perpendicular pressure to the magnetic-field energy density). These ions include H^+ , He^+ , and O^+ that were measured in the energy intervals 0.11 keV to 1.6 MeV, 0.11 to 400 keV, and 0.11 to 100 keV, respectively, over nearly the entire pitch-angle range. Graphs of the ion pressures against L for 4 CRRES orbits will be compared with pre-storm values. These results also will be correlated with available geomagnetic indices, on-board measurements of the magnetic field, and the position of the magnetopause at the subsolar point based on the measurements of the solar-wind pressure by the IMP-8 spacecraft.

Real time monitoring of the geophysical parameters in support of the CRRES chemical releases.

S. B. Mende, H. L. Collin, W. K. Peterson,
Lockheed Palo Alto Research Laboratories, Palo Alto CA, 94304
T. A. Fritz,
Los Alamos National Laboratories, Los Alamos NM 87545
G. Haerendel,
Max Planck Institut für Extraterrestrische Physik, Garching, Germany 8046
R. R. Anderson,
D. A. Hardy, H. J. Singer, U. S. Air Force Geophysics Laboratory, Hanscom
AFB, MA 01731,
J. C. Foster, MIT Haystack Observatory, Westford MA 01886
D. L. Reasoner, NASA George C. Marshall Spaceflight Center, Huntsville, AL
35812.

The high altitude releases of the CRRES program were active experiments whose success depended strongly on the ambient magnetospheric geophysical conditions. During the January and February campaign the magnetospheric conditions were monitored in real time prior to release in an attempt to predict conditions for each release. The small barium releases were designed to test the interaction of the ion clouds with the ambient magnetospheric environment during conditions of widely varying ambient cold plasma densities. For these releases the in situ cold plasma density was monitored through the real time observation of the wave receiver on the CRRES satellite. The large barium clouds were intended to produce auroral enhancements at the foot of the magnetic field line. In addition to the knowledge of the cold plasma density at the satellite these experiments required the observation of the auroras at the foot of the field line, measurements of the ionospheric electric fields in the conjugate ionosphere and reading of the magnetic field and energetic particle data at the satellite. The auroral conditions were observed by the instrumented aircrafts and the ionospheric fields were measured by the Millstone Hill incoherent scatter radar. During these releases the required geophysical conditions were met which contributed to the success of the experiments. The large Li releases were intended to precipitate local fluxes of energetic electrons by pitch angle diffusion in the presence of the artificially injected cold lithium ions. This experiment dictated the toughest conditions because it required low cold plasma density, high electron fluxes at the satellite and uniform dim auroras at the conjugate region. During the campaigns excellent sets of data were gathered which characterized the aurora, the simultaneous particle and field measurement at the satellite and the accompanying convection in the ionosphere during various conditions.

Appendix 3

Distribution in Magnetotail of O^+ Ions

Distribution in Magnetotail of O^+ Ions from Cusp/Cleft Ionosphere: A Possible Substorm Trigger

J. B. Cladis and W. E. Francis

Lockheed Palo Alto Research Laboratory, Palo Alto, CA 94304

ABSTRACT

The transport of O^+ ions from the cusp/cleft ionosphere to the magnetotail during highly disturbed times was determined by computing the guiding-center trajectories of the ions to a distance of $6 R_E$ from the ionosphere and the full-motion trajectories at later times. Case histories were tallied in 3 planes perpendicular to the X_{GSM} axis, 3 planes perpendicular to the Y_{GSM} axis, and in the center plane of the tail. At various times relative to the enhancement of the convection electric field, the following ion properties were constructed from the case histories: number density, mean energy, energy and pitch-angle distributions of the flux, and the ion pressure components parallel and perpendicular to the magnetic field. It was found that after about 1.7 hours the ion flux in the near-earth magnetotail increased dramatically, and the spectrum hardened — much as observed during periods just preceding substorms. This increase is attributed to (i) the increase in the O^+ outflux from the ionosphere, (ii) the increased energization of the ions by the convection electric field, and (iii) ion trapping, which generally occurs because the ion magnetic moments generally increase after the ions first cross the geotail center plane. Moreover, the parallel pressure of the ions exceeds the energy density of the magnetic field at $X_{GSM} < -8 R_E$. Based on the expected alterations of the magnetic and electric fields in response to this O^+ pressure, a substorm trigger mechanism is suggested.

INTRODUCTION

During times of enhanced magnetospheric convection, the upward flow of high-density low-velocity O^+ ions from the dayside cusp/cleft ionosphere increases significantly, as discussed by Yau et al., [1986]. Those ions with energies greater than about the gravitational escape energy flow along tailward-convecting polar field lines and are highly accelerated along the magnetic field by the convection electric field, especially in regions where the curvature of their guiding-center trajectories in the earth frame is large [Cladis, 1986]. In the nightside magnetosphere, the ions cross the center plane of the magnetotail at various positions, depending principally on their initial positions and velocities as well as on the magnetic and electric field configurations [Cladis, 1988].

Delcourt et al. [1989] computed the three-dimensional distribution of these ions in the lobes and nightside magnetosphere using the magnetic field model of Mead and Fairfield [1975] and the initial convection pattern of Volland [1978]. Their results, while representative of typical distributions during quiet to moderately active conditions, seriously understate the O^+ flux in the midnight sector during disturbed times. The difficulty lies in their assumption of the conservation of the magnetic moment of the ions in the magnetotail. Indeed, this assumption may be justified for some trajectories computed in the convection electric field model of Volland [1978], which is uniform over the polar cap. But more realistic convection models reveal that the electric field is intensified appreciably in just the region where the cusp/cleft ions are convected [e.g., Heppner and Maynard, 1987]. Therefore, when the potential across the polar cap is high, ions with initial energies so high that they usually move far tailward along lobe field lines are now convected more rapidly toward the central plasma sheet. Hence, they cross the center plane, where the field-line curvature is large, with much higher energies. Under these conditions the magnetic moment generally is not conserved. The ions, prior to crossing the center plane, are highly aligned with the magnetic field. Hence, the "scattering" associated with the magnetic-moment breakdown about the center plane generally causes the ions to be trapped as shown below (in Figure 2). Ion trapping greatly increases the flux, not only in the region of the breakdown, but especially in regions along the inward drift paths of the ions, where the ion confinement space decreases and velocity space expands due to the continued acceleration of the ions by the convection electric field.

Here, we compute the time-dependent characteristics of the O^+ ions in the nightside magnetosphere as a function of time measured from the commencement of an enhanced convection event. We use the Heppner-Maynard [1987] convection pattern for $(B_y)_{IMF} > 0$ in the northern hemisphere and the Tsyganenko [1987] "short-tail", active-time ($Kp \geq 5^-$), magnetic field model, which is considered to be appropriate to $30 R_E$. The guiding-center equations of motion are integrated in calculating the ion trajectories to a distance of about $6 R_E$ from the earth. Beyond $6 R_E$, full-motion trajectories are computed. The results indicate that, within 1.7 hours following an enhanced-convection event, the spectrum of the O^+ flux in the near-earth magnetotail becomes quite hard, being comparable to the flux measured just prior to substorm onsets [Daglis, 1990; Kistler et al., 1990; Möbius et al., 1987]. Moreover, the pressure of the O^+ ions in the region $-13 < X_{GMS} < -8 R_E$, $0.5 < Y_{GMS} < 2 R_E$, and $-2 < Z_{GMS} < +2 R_E$, becomes very large, with the O^+ pressure component parallel to the magnetic field exceeding the energy density of the magnetic field at $X_{GMS} < -8 R_E$. The accelerated ions therefore affect the dynamics of the magnetotail. In fact, correlation of the timing and location of the O^+ pressure in the magnetotail with observed features of substorms indicate that the O^+ ions may play a dominant role in the triggering of the substorm. From the changes of the magnetic and electric fields implied by the O^+ pressure, a possible triggering mechanism is suggested.

TRANSPORT CALCULATIONS

The model of the O^+ source is based on measurements of the upflowing ions made with the Energetic Ion Composition Spectrometer (EICS) and the Retarding Ion Mass Spectrometer (RIMS) on the DE-1 spacecraft over the dayside cusp/cleft ionosphere. The statistical study by Yan et al. [1986] of the EICS data obtained during the period September 1981 to January 1983, normalized to the reference altitude of 1000 km, reveals that the outflux of O^+ in the energy range .01 to 1 keV peaks near the invariant latitude of 78° in the noon sector (09 to 15 hr MLT), with the principal outflux lying between about 72 to 80° . From their graph of the O^+ outflux versus invariant latitude for disturbed times, we estimate the mean outflux in the invariant-latitude interval 72 to 80° to be about $5 \times 10^8 \text{ cm}^{-2} \text{ s}^{-1}$. The energies of O^+ from this region of the polar ionosphere are low, ranging from about 2 eV to > 100 eV, with the transverse distribution characterized by a temperature of about 10 eV [Shelley et al., 1982; Waite et al. 1985; Moore et al,

1986]. Accordingly, the source was taken to be Maxwellian in the upper hemisphere with a temperature of 10 eV, normalized to an outward flux, F_s , along the magnetic field of $5 \times 10^8 \text{ cm}^{-2} \text{ s}^{-1}$ for energies higher than $w_1 = 7.5 \text{ eV}$ at the altitude of 1000 km. That is,

$$F_s = \frac{2}{m^2} \int_{w_1}^{\infty} w dw \int_0^{\pi/2} f(w, \alpha) 2\pi \sin \alpha \cos \alpha d\alpha \quad (1)$$

where $f(w, \alpha)$ is the distribution function and m, w , and α are the O^+ mass, energy, and pitch angle, respectively. The ion source was taken to be constant from 09 to 15 hr MLT and from 72 to 80° invariant latitude.

The statistical study of Yau et al. [1986] also revealed that the O^+ outflow rate increases exponentially with the Kp index, with the rate at $Kp \geq 6$ being a factor of 30 larger than at $Kp = 0$. It is therefore expected that the O^+ outflux will be at its statistical active-times value during an enhanced convection event.

MAGNETOSPHERIC MODELS

The magnetosphere was modeled by (1) the "short-tail" version of the magnetic field model of Tsyanenko [1987], as improved and coded by David Stern of NASA/Goddard, with the model parameters set for $Kp \geq 5^-$ and tilt angle $= 0^\circ$, and (2) the convection electric field model of Heppner and Maynard [1987] that is generally appropriate in the northern hemisphere for $(B_y)_{IMF} > 0$. The polar-cap potential drop, $\Delta\Psi$, was taken to be 100 kV, which is appropriate for $Kp \approx 5^\circ$ and $AE \approx 600$ according to Table 1 of Heppner and Maynard [1987]. This correlation of Kp and AE , based on the polar-cap potential drop, is consistent with the data presented by Rostoker [1991] on the general correlation of these indices. According to Caan et al. [1978] the AE index, averaged over 1777 substorm periods, had a maximum value of about 440. Therefore, the models used here are appropriate for more highly disturbed times. Both a more relaxed magnetic-field configuration and a lower polar-cap potential drop would lead to lower O^+ pressures in the magnetotail. The conditions adopted here, as discussed under Results, are similar to the conditions under which the substorm data on O^+ ions were taken that were used to test the computed fluxes.

The equi-potential contours of the Heppner-Maynard model for $\Delta\Psi = 76 \text{ kV}$ are shown in Figure 1 (Fig. 3 of Heppner and Maynard [1987]). An efficient routine, which

is described in the Appendix, was developed to map the electric field from the reference plane in the ionosphere, where the convection potentials are specified, to the ion positions in the magnetosphere.

An example of the ion motion in these magnetic and electric field models, which also demonstrates the importance of the full-motion calculation, is shown in Figure 2. Panel 2a shows the guiding-center motion of an O^+ ion under the conditions $Kp=4^-$, 4 , 4^+ and $\Delta\Psi = 76$ kV, projected in the X_{GSM}, Z_{GSM} plane). The initial position of the ion was at 79° MLAT, 15 hr MLT, and altitude of 1000 km, and its initial energy and pitch angle were 10.4 eV and 92.5° , respectively. As shown in the figure the ion crosses the center plane at about $X_{GSM} = -14.5 R_E$ and directly enters the earth's atmosphere in the southern hemisphere. In Panel 2b the full motion (broken line curve) of this ion is shown, starting at the radial distance of $6 R_E$. The solid line is the locus of the center of curvature determined from the instantaneous positions and velocities of the ion. Note that this trajectory is the almost identical to the guiding-center trajectory until the ion first crosses the center plane. Afterwards, the ion becomes trapped as discussed in the introduction.

ANALYSIS

The running time on the VAX 11/785 required to compute the full motion of the ions was appreciable, even though the routine used to map the electric field is more efficient than the ones used previously [e.g., Cladis and Francis, 1989; Delcourt et al., 1989]. Therefore, the number of trajectories was highly restricted. The source region was divided into 24 sections, each 1 hr MLT by 2° MLAT at the 1000-km altitude, and 6 ions trajectories were computed from each section. Because the case history of an ion is affected much more by its initial speed than its pitch angle, the initial pitch angle of each ion was taken to be the same, viz. 105° . The six initial speeds were taken to be at the centers of constant portions, ΔF_s , of the parallel flux given by the distribution function. That is, each initial speed, v_i was determined by integrating Eq. (1) from $\frac{1}{2}mv_{i-\frac{1}{2}}^2$ to $\frac{1}{2}mv_{i+\frac{1}{2}}^2$, with $\frac{1}{2}mv_{1-\frac{1}{2}}^2 = 7.5$ eV and $\frac{1}{2}mv_{6+\frac{1}{2}}^2 = \infty$, and setting $\Delta F_s = \frac{1}{6}(5 \times 10^8) \text{ cm}^{-2} \text{ s}^{-1}$.

The ion case histories were tallied in six planes perpendicular to the X_{GSM} axis, at $X_{GSM} = -5, -6.5, -8, -10, -13$, and $-20 R_E$; three planes perpendicular to the Y_{GSM} axis, at $Y_{GSM} = -1, .5$, and $2 R_E$; and in the center plane, $Z_{GMS} = 0$. The listing for each ion, j ,

in the plane included the index, s , identifying the source element, the plane crossing point (x_j, y_j, z_j) , time (T_j) , velocity (v_{xj}, v_{yj}, v_{zj}) , pitch angle (α_j) , total energy (w_j) , magnetic field $(B_{xj}, B_{yj}, B_{zj}, B_j)$, electric field (E_j) , and $|\vec{E}_j \times \vec{B}_j / B_j^2| = v_{Ej}$. Contributions from the ion source in the southern hemisphere were taken into account, assuming symmetry about the center plane, by adding an identical listing, but with $z_{j^*} = -z_j$, $v_{xj^*} = -v_{xj}$, and $B_{xj^*} = -B_{xj}$, for the conjugate ion j^* . The bulk properties of the ions were averaged in certain areas A_k that were selected on the basis of the distribution of the crossing points in the planes. The areas A_k were about equal to $(B_s/B_k)A_s$, where B_s is the field intensity at the center of the source area, A_s , and B_k is the field intensity at the center of A_k .

The mean ion flux normal to A_k , summed over both directions, at the time T_n is, approximately,

$$F_k(T_n) = \Delta F_s \sum_i \frac{A_i}{A_k} \sum_j \frac{v_{\perp ij}}{v_{ij}} \quad (2)$$

where $v_{\perp ij}$ is the velocity component, perpendicular to the plane, of the ion that originates from the source element i and crosses A_k at $T \leq T_n$, and v_{ij} is the total velocity of that ion. This equation is not strictly correct because the number of ions per second, viz. $\Delta F_s A_i$, represented by a single ion crossing within A_k , may not all fall within A_k if A_i does not map entirely into A_k . This situation certainly occurs when ions cross A_k near its boundary. However, this effect tends to be offset by ions that cross the plane at corresponding points at the other side of that boundary. The error in the flux - and in the additional ion properties listed below - is negligible if the area A_k is located within a region in which the density of ion-crossing points is uniform, but it becomes appreciable, about a factor of two, if A_k is located in a region where the density of the ion-crossing points is high and drops-off abruptly to zero beyond one of its boundaries. In general, the gradients of the ion properties, as depicted by averaged values in adjacent areas (histograms), are too high by amounts that increase with the magnitudes of the gradients.

The additional ion properties averaged in A_k are the following:

The number density,

$$n_k(T_n) = \Delta F_s \sum_i \frac{A_i}{A_k} \sum_j \frac{1}{v_{ij}}$$

The energy,

$$w_k(T_n) = \frac{1}{J} \sum_1^J w_j$$

where the summation is over the ions from all the source elements that cross A_k at $T \leq T_n$.

The energy spectrum of the omnidirectional flux,

$$J_k(w_l, T_n) = \frac{\Delta F_s}{\Delta w_l} \sum_i \frac{A_i}{A_k} N_{il}$$

where N_{il} is the number of ions from source element i that cross A_k with energies within Δw_l at $T \leq T_n$.

The ion pressure parallel to the magnetic field,

$$P_{\parallel k}(T_n) = 2\Delta F_s \sum_i \frac{A_i}{A_k} \sum_j \frac{w_{\parallel ij}}{v_{ij}}$$

where w_{\parallel} is the ion energy component parallel to the magnetic field ($w_{\parallel} = \frac{1}{2}m(\vec{v} \cdot \vec{B}/B)^2$).

The ion pressure perpendicular to the magnetic field

$$P_{\perp k}(T_n) = \Delta F_s \sum_i \frac{A_i}{A_k} \sum_j \frac{w_{\perp ij}}{v_{ij}}$$

where w_{\perp} is the ion energy component perpendicular to the magnetic field in the $\vec{E} \times \vec{B}$ frame.

And the parallel and perpendicular ion pressures divided by the energy density of the magnetic field ($B^2/2\mu_o$),

$$\beta_{\parallel k}(T_n) = 2\mu_o \Delta F_s \sum_i \frac{A_i}{A_k} \sum_j \frac{w_{\parallel ij}}{v_{ij}} \frac{1}{B_{ij}^2}$$

and

$$\beta_{\perp k}(T_n) = 2\mu_o \Delta F_s \sum_i \frac{A_i}{A_k} \sum_j \frac{w_{\perp ij}}{v_{ij}} \frac{1}{B_{ij}^2}$$

where B is the magnetic field intensity at the ion-crossing point.

RESULTS

The crossing points of the O^+ ions in the planes $X_{GSM}=-6$, $Y_{GSM}=0.5$, and $Z_{GSM}=0$ are shown in Figure 3. As discussed previously, the distributions are symmetrical about the plane $Z_{GSM}=0$. In panels (a) and (b) the crossing points at $Z_{GSM} \geq 5$ are due to the ions in the lobes. The points at the lower values of Z_{GSM} are due to trapped ions that repeatedly cross the planes as they bounce along field lines and drift toward the west. Panel (c) exhibits the most unexpected feature of the distribution: nearly all the crossing points in the center plane, $Z_{GSM}=0$, occur at $Y_{GSM} > 0$ and the O^+ ions gain so much energy that they all drift toward the west. This feature is due to both the displacement of the ions along the convection electric field during the acceleration process and the large Y_{GSM} component of the $\vec{E} \times \vec{B}$ drift, as shown by the potential contours of Figure 1. Note in panel (a) that the ions in the lobes cross the $X_{GSM} = -6$ plane at increasing values of Y_{GSM} toward decreasing values of Z_{GSM} . Our previous calculations, as well as those of Delcourt et al.[1989] and others, performed with convection models in which the equipotential contours in the polar ionosphere were parallel to the X_{GSM} axis, the center-plane crossing points were more nearly symmetrical about the Y_{GSM} plane.

Histograms of the number density of the O^+ ions in the center plane at the times 1.7, 2.0, 2.3, and 2.6 hours after the commencement of an enhanced convection event are shown in Figure 4. These densities were averaged over the ΔX_{GSM} intervals of the histograms and $0 \leq Y_{GSM} \leq +2$. At $T = 1.7$ hr the number density is already fairly high, being about 0.1 cm^{-3} , and nearly constant at $X_{GSM} < -6.5$. Toward later times the number density increases everywhere in the tail, but especially in regions toward the earth, owing to the inward drift of the trapped ions. In the plane $X_{GSM}=-10$, the density averaged in ΔZ_{GSM} bins, with $0 \leq Y_{GSM} \leq +2$, decreases to half the center-plane value in the bin $2 \leq Z_{GSM} \leq 3$. A statistical study of the ion properties in the plasma sheet in the region $(-10 > X_{GSM} > -23)$, measured with ion spectrometers on the ISEE-1 spacecraft in the range .1 to 16 keV/e, was performed by Lennartsson and Shelley [1986]. According to this study, the average O^+ density in this region is about $.2 \text{ cm}^{-3}$ during highly disturbed times. The densities shown in Figure 4 are in agreement with this value in the region ($X_{GSM} < -10$) where they can be compared.

Histograms of the O^+ energy, displayed at the same times and averaged in the same

bins of the center plane, are shown in Figure 5. Since the faster ions arrive earlier in the tail, the mean ion energies are high at $T = 1.7$ hr. The distribution does not change appreciably at later times, especially at $X_{GSM} < -10$. The mean O^+ energies reported by Lennartsson and Shelley [1986], which were averaged over ΔX_{GSM} intervals of $5 R_E$, $|Y_{GSM}| < 10$, and $|Z_{GSM}| < 10$, were approximately constant, near 5 keV, from $X_{GSM} = -23$ all the way to $X_{GSM} < -6$. So, while the computed energies are in agreement with these measurements at $X_{GSM} < -13$, they are appreciably higher at $X_{GSM} > -13$. Surely some of this discrepancy can be attributed to the high localization of these cusp/cleft ions in space and time, as well as to the limited energy response (< 16 keV) of the spectrometer. However, as discussed in the following section, the computed energy, averaged in the interval .1 to 16 keV, is expected to be lower because of the changes in the magnetic and electric fields that occur when the O^+ pressure is applied. The only other measurements of O^+ ions in the tail were made with the Suprathermal Energetic Ion Charge Analyzer (SULEICA) on the AMPTE/IRM spacecraft at $X_{GSM} > -19$ and the Charge Energy Mass Spectrometer (CHEM) on the AMPTE/CCE spacecraft at $X_{GSM} > -9$. High fluxes of O^+ ions with energies exceeding 50 keV were measured by both spacecraft just before- and after- the expansion phase of substorms [Kistler et al., 1990; Daglis et al., 1990; Möbius et al., 1987].

The energy spectrum of the omnidirectional flux in the center plane, averaged over $-5 \geq X_{GSM} \geq -13$ and $0 \leq Y_{GSM} \leq +2$, at $T = 3.0$ hr is shown in Figure 6. Measurements of ion distributions in the central plasma sheet generally indicate that the distributions are approximately isotropic, and approximately Maxwellian at energies lower than that at the "knee", which is the energy above which the directional flux decreases sharply toward a nonthermal power-law tail [see, e.g. Christon et al., 1991]. Although this computed O^+ distribution is not the usual one present in the central plasma sheet, the energy spectrum of a Maxwellian with a "temperature" of 7.3 keV (broken-line curve) is drawn in Figure 6 for comparison. Surely, the calculated flux is not sufficiently detailed to assess such a feature of the spectrum. However, the pitch-angle distribution of the ions is clearly anisotropic. It is a butterfly distribution with maxima at 30 and 150° that are higher than the 90° level by more than a factor of 4. This distribution is similar to the one measured with the AMPTE/CCE spacecraft near $X_{GSM} = -6.9$ about 23 minutes prior to the occurrence of a substorm [Daglis et al., 1990]. Moreover, after dividing the flux shown in Figure

6 by a reasonable value of the solid angle, ≈ 10 steradians, it is in satisfactory agreement, over the entire energy range (1 to 50 keV), with the pre-substorm flux at energies > 1 keV reported by Daglis et al. [1990], and with the pre- and post-substorm fluxes reported by Kistler et al. [1990] at energies above 35 keV. The Kp and AE indices at the times of these measurements were similar to those used for the selection of magnetospheric models. The three-hourly Kp index at the time of the measurements of Daglis et al. [1990] was 5^+ compared to the model parameter 5° ; and the AE index, averaged over the pre- and post-substorm AE values of the 12 substorms included in the study of Kistler et al. [1990], was 633 compared to the model parameter 600.

In Figure 7 histograms of the parallel and perpendicular ion pressures in the center plane, in units of keV/cm^3 , are shown at the same time and locations as those of the density and energy in Figures 4 and 5. Note that the parallel pressure (solid lines) exceeds the perpendicular pressure (broken lines) at all times, especially at $X_{GSM} < -13$. From 1.7 to 2.0 hours, the pressures increase rapidly at $X_{GSM} < -6.5$; as time progresses the pressures increase more rapidly in successively inward bins. Figure 8 shows these pressures divided by the energy density of the magnetic field. Note that at $T > 2$ hr both of these pressure ratios exceed 1 at $X_{GSM} < -8$. Since, as discussed below, the perpendicular current implied by these ion pressures is very high, these O^+ ions may indeed be the current carriers sought by Kaufmann [1987] to explain the pre-substorm reduction of the magnetic field intensity near geosynchronous altitudes.

DISCUSSION

The O^+ pressure shown in Figure 8 is so high that it must affect the dynamics of the near-earth magnetotail. Do these ions trigger substorms? Phenomenologically, it appears that they do:

- (1) They are injected into the central plasma sheet in the region where a near-earth neutral line is expected to form [e.g., Nishida, 1984].
- (2) They arrive in the magnetotail at an appropriate time (≈ 1.7 hours) following the commencement of an enhanced magnetospheric-convection event, considering that substorms often occur after a delay of 1 to 2 hours after the southern turning of the interplanetary magnetic field [e.g., Baker, 1986]. And,

(3) Their flux is consistent with the pre-substorm O^+ flux measured in the near-earth magnetotail [Daglis et al. 1990; Kistler et al., 1990].

How do these ions trigger a substorm? Baker et al. [1982] suggest that the presence of O^+ ions in the magnetotail, owing to their large gyroradius ρ , may trigger a substorm by increasing the growth rate of the ion tearing mode instability. Their suggestion is based on the derivation by Schindler [1974] of the linear growth rate of the instability, which is proportional to $\rho^{3/2}$. Here, another mechanism is suggested based on the changes of the electric and magnetic fields resulting from the arrival of the ions.

Clearly, the magnetic field configuration must begin to change much before the O^+ pressure exceeds the energy density of the magnetic field. The change of the magnetic field in response to the particle pressure can be estimate by computing the perpendicular current density \vec{j}_\perp in the center plane implied by the O^+ pressure. The current density is related to the particle pressure by the equation [Parker, 1957],

$$\vec{j}_\perp = \frac{\hat{e}_1}{B} \times \left[\nabla P_\perp + (P_\parallel - P_\perp) \frac{\hat{x}}{R_c} \right] \quad (3)$$

where \hat{e}_1 is a unit vector along the magnetic field, \hat{x} is a unit vector in the X_{GSM} direction, B is the magnetic-field intensity, and R_c is the radius of curvature of the magnetic field. As shown in Figure 7 at $T \geq 2$ hr, P_\parallel exceeds P_\perp by more than a factor of two at $X_{GSM} < -5$. Moreover, R_c , which is less than about $1 R_E$ at $X_{GSM} < -8$, is much less than the scale length of ∇P_\perp . Hence, the second term in (3), which gives a current density that is directed from dawn-to-dusk, is dominant. Taking $P_\parallel - P_\perp = 2.5 \text{ keV/cm}^3$, $R_c = 1 R_E$, and $B = 9 \text{ nT}$ at $X_{GSM} = -9$ where $\nabla P_\perp \approx 0$, then $j_\perp \approx 70 \times 10^{-10} \text{ Amp/cm}^2$. (The dawn-to-dusk current density at this point in the magnetic field model used for these transport calculations is about $50 \times 10^{-10} \text{ Amp/cm}^2$ [Tsyganenko, 1987]. Such a current density, therefore, causes an appreciable elongation of the local magnetic field.

As the local magnetic field elongates under the pressure of the ions, an electric field, directed from dusk-to-dawn in the center plane, is induced by the change of the magnetic field. Hence, by opposing the convection electric field, this induced field reduces the O^+ pressure, as expected, from the values described above. The induced field, which is highly structured along the Y_{GSM} coordinate, also produces velocity shears in the earthward-convecting flow near the dawn and dusk "boundaries" of the injected

O^+ population. Short of a full computer simulation of the dynamical interactions of the plasma and the magnetic and electric fields, it is difficult to assess the magnitudes of these effects. However, an estimate of the maximum change of the magnetic field during the pressure build-up time indicates that these shears may be very large. A substorm may, therefore, be triggered by velocity-shear instabilities that produce short-scale electric and magnetic turbulence. Such turbulence, by impeding the dawn-to-dusk current flow across the injected O^+ region, may divert current to the ionosphere, forming the current wedge [e.g., McPherron et al., 1973]. According to the substorm-simulation results of Kaufmann [1987] and Robinson and Rinaldi [1991], the current diversion alone could trigger a substorm. Additionally, however, the turbulence may enhance field-line merging, which ultimately provides the substorm energy [Stern, 1990; Kan, 1990]. Velocity-shear instabilities in the auroral ionosphere are discussed by Kintner [1976] and Kelley and Carlson [1977]. Also, the Kelvin-Helmholtz instability has been applied in the magnetosheath by Southwood [1979] and in the magnetotail by Rostoker [1987].

CONCLUSIONS

The results listed below strongly indicate that, during times of enhanced convection, the O^+ ions, which originate from the cusp/cleft ionosphere, may trigger substorms:

1. In the near-earth plasma sheet, the flux of O^+ increases dramatically, and the spectrum becomes hardened, resembling the O^+ fluxes measured with the AMPTE-IRM/CCE spacecraft at periods preceeding substorms. This increased flux at disturbed times is due to (i) the increased outflux of the ions from the ionosphere, (ii) the increased energization of the ions by the convection electric field, and (iii) the trapping of the ions resulting from breakdown of their magnetic moments during their first crossing of the center plane.
2. The increased O^+ flux and pressure occur after a delay of 1.7 hrs following the enhancement of the convection field. Such a time delay is consistent with the observed delay (1 to 2 hrs) of the general occurrence of substorms following the southern turning of the interplanetary magnetic field.
3. The ion pressure is applied in the region of the magnetotail where the near-earth neutral line is expected to form.

Estimates of the magnetic and electric field changes in response to the O^+ pressure in the tail indicates that shears in the convection velocity will develop near the flanks (dawn and dusk) of the O^+ injection region. It is suggested that the substorm may be triggered by velocity-shear instabilities that effectively create anomalous resistivity in the near midnight region of the neutral sheet.

APPENDIX

A brief description is given here of the routine developed to map the electric field from the ionosphere to the ion positions in the magnetosphere. Piecewise mathematical expressions of the convection electric field distribution given by the potentials are pre-determined as a function of polar coordinates in the reference plane, and the corotation electric field is added vectorially, giving the total electric field (magnitude and direction) as a function of position. The routine computes two mutually perpendicular electric field components, $\hat{e}_2 E_{2p}$ and $\hat{e}_3 E_{3p}$, at the ion position by tracing only two magnetic field lines as follows: (i) The magnetic field line through the ion position is traced to its intersection (point 1) of the reference plane; at this point the total electric field $\vec{E} = \vec{E}_{\text{convection}} + \vec{E}_{\text{corotation}}$ is computed from the mathematical expressions. (ii) A second magnetic field line, displaced from the particle position by the distance $\hat{e}_2 \delta \xi_2$ is traced to the reference plane (point 2), and the displacement, $\hat{\eta} \delta \eta_2$, of point 2 from point 1 is determined. Here, $\hat{\eta}$ is a unit vector directed from point 1 to point 2, and the unit vectors \hat{e}_1 , \hat{e}_2 , and \hat{e}_3 are in the directions of the magnetic field intensity \vec{B} , the direction $\vec{B} \times \nabla B$, and the direction $\hat{e}_1 \times \hat{e}_2$, respectively. The desired components are then obtained from the equations,

$$E_{2p} = (\vec{E} \cdot \hat{\eta}) \cdot \frac{\delta \eta_2}{\delta \xi_2}$$

and

$$E_{3p} = |\vec{E} - \vec{E} \cdot \hat{\eta} \hat{\eta}| \frac{\delta \eta_3}{\delta \xi_3}$$

where, from the conservation of magnetic flux,

$$\frac{\delta \eta_3}{\delta \xi_3} = \frac{B_p}{B_1} \cdot \frac{\delta \xi_2}{\delta \eta_2}$$

B_p and B_1 are the magnetic field intensities at the ion position and at point 1, respectively.

Computational efficiency is further improved by projecting the electric field forward for several time steps using the equations,

$$E_{i,n} = E_{i,n-1} \left(\frac{B_n}{B_{n-1}} \right)^{k_i}$$

where $i = 1, 2$ denotes the electric field components, and n denotes the current particle position. The exponents k_i are determined from the values of E_i and B at the two previous points at which the E_i components are computed by tracing field lines. The final projected values of E_i are compared with the computed values. If the error in either component is excessive, the particle is returned to the position of the previously computed values of E_i and the number of projected values is reduced by fraction depending on the magnitude of the error.

Acknowledgements. We wish to thank D. P. Stern of NASA/Goddard for improving and coding the Tsyganenko magnetic field model that we used in our calculations. We also thank G. T. Davidson, R. M. Robinson, Y. T. Chiu, and W. Lennartsson of the Lockheed Research Laboratory for helpful discussions. This work was supported by NASA under contract NASW 4407 and the Lockheed Independent Research Program.

REFERENCES

- Baker, D.N., Statistical analysis in the study of solar wind-magnetosphere coupling, pp. 17-38, in *Solar Wind-Magnetosphere Coupling*, edited by Y. Kamide and J. A. Slavin, Terra Sci. Publ. Co., Tokyo, Japan, 1986.
- Baker, D.M., E.W. Hones, Jr., D.T. Young, and J. Birn, The possible role of ionospheric oxygen in the initiation and development of plasma sheet instabilities, *Geophys. Res. Lett.*, **9**, 1337, 1982.
- Caan, M. N., R. L. McPherron, and C. T. Russell, The statistical magnetic signature of magnetospheric substorms, *Planet. Space Sci.*, **26**, 269, 1978.
- Christon, S.P., D.J. Williams, and D. G. Mitchell, C.Y. Huang and L. A. Frank, Spectral characteristics of plasma sheet ion and electron populations during disturbed geomagnetic conditions, *J. Geophys. Res.*, **96**, 1, 1991.
- Cladis, J.B., Parallel acceleration and transport of ions from polar ionosphere to plasma sheet, *Geophys. Res. Lett.*, **13**, 893, 1986.
- Cladis, J.B., Transport of ionospheric ions in the magnetosphere: Theory and observations, *Adv. Space Res.*, Vol. 8, No. 8, pp. (8)165-(8)173, 1988.
- Cladis, J.B., and W.E. Francis, The polar ionosphere as a source of the storm time ring current, *J. Geophys. Res.* **90**, 3465, 1985.
- Cladis, J.B., and W.E. Francis, Transport of ions injected by AMPTE magnetotail releases, *J. Geophys. Res.*, **94**, 5497, 1989.
- Daglis, I.A., E.T. Sarris, and G. Kremser, Indications for ionospheric participation in the substorm process from AMPTE/CCE observations, *Geophys. Res. Lett.*, **17**, 57, 1990.
- Delcourt, D.C., C.R. Chappell, T.E. Moore, and J.H. Waite, Jr., A three-dimensional numerical model of ionospheric plasma in the magnetosphere, *J. Geophys. Res.*, **94**, 11,893, 1989.
- Heppner, J. P., and N. C. Maynard, Empirical high-latitude electric field models, *J. Geophys. Res.* **92**, 4467, 1987.
- Kaufmann, R. L., Substorm currents: Growth phase and onset, *J. Geophys. Res.* **92**, 7471, 1987.
- Kan, J.R., Tail-like reconfiguration of the plasma sheet during the substorm growth phase, *Geophys. Res. Lett.*, **17**, 2309, 1990.

- Kelley, M.C., and C.W. Carlson, Observations of intense velocity shear and associated electrostatic waves near an auroral arc, *J. Geophys. Res.*, 82, 2343, 1977.
- Kintner Jr., P.M., Observations of velocity shear driven plasma turbulence, *J. Geophys. Res.*, 81, 5114, 1976.
- Kistler, L.M., E. Möbius, B. Klecker, G. Gloeckler, F.M. Ipavich, and D.C. Hamilton, Spatial variations in the suprathermal ion distributions during substorms in the plasma sheet, *J. Geophys. Res.* 95, 18,871, 1990.
- Lennartsson, W., and E. G. Shelley, Survey of 0.1 to 16 keV/e plasma sheet ion composition, *J. Geophys. Res.*, 84, 4405, 1986.
- Mcpherron, R.L., C.T. Russell, and M.P. Aubry, Satellite studies of magnetospheric substorms on August 15, 1968, 9. Phenomenological model for substorms, *J. Geophys. Res.* 78, 3131, 1973.
- Mead, G.D., and D.H. Fairfield, A quantitative magnetospheric model derived from spacecraft magnetometer data, *J. Geophys. Res.*, 80, 523, 1985.
- Möbius, E., M. Scholer, B. Klecker, D. Hovestadt, and G. Gloeckler, and F.M. Ipavich, Acceleration of ions of ionospheric origin in the plasma sheet during substorm activity, pp. 231-234, in *Magnetotail Physics*, edited by A.T.Y. Lui, The John Hopkins University Press, Baltimore, Md., 1987.
- Moore, T.E., M. Lockwood, M.O. Chandler, J.H. Waite, Jr., C.R. Chappell, A. Persoon, and M. Sugiura, Upwelling O⁺ ion source characteristics, *J. Geophys. Res.*, 91, 7019, 1986.
- Nishida, A., Reconnection in the Earth's magnetotail: An overview, pp. 159-167, in *Magnetic Reconnection in Space and Laboratory Plasmas*, Geophys. Monogram, Vol. 30, edited by E.W. Hones, Jr., AGU, Washington, D. C., 1984.
- Parker, E.N., Newtonian development of the dynamical properties of ionized gases at low density, *Phys. Rev.* 107, 923, 1957.
- Robinson, R.M., and M.A. Rinaldi, Modeling auroral arc morphology and dynamics during substorms, *J. Geophys. Res.*, Submitted, 1991.
- Rostoker, G., The Kelvin-Helmholtz instability and its role in the generation of electric currents associated with Ps 6 and westward traveling surges, pp. 169-173, in *Magnetotail Physics*, edited by A.T.Y. Lui, The John Hopkins University Press, Baltimore, Md., 1987.

- Rostoker, G., A quantitative relationship between AE and Kp, *J. Geophys. Res.* 96, 5853, 1991.
- Schindler, K., A theory of the substorm mechanism, *J. Geophys. Res.*, 79 2803, 1974.
- Shelley, E.G., W.K. Peterson, A. G. Ghielmetti, and J. Geiss, The polar ionosphere as a source of energetic magnetospheric plasma, *Geophys. Res. Lett.*, 9, 941, 1982.
- Southwood, D.J., Magnetopause Kelvin-Helmholtz instability, p. 357, in *Magnetospheric Boundary Layers*, edited by B. Battrock and J. Mort, ESA Sci. Tech. Publ. Branch, Noordwijk, The Netherlands, 1979.
- Stern, D.P., Substorm electrodynamics, *J. Geophys. Res.*, 95, 12,057, 1990.
- Tsyganenko, N. A., Global quantitative models of the geomagnetic field in the cislunar magnetosphere for different disturbance levels, *Planet. Space Sci.*, 35, 1347, 1987.
- Volland, H., A model of the magnetospheric electric convection, *J. Geophys. Res.*, 83,2695, 1978.
- Waite, J. H., T. E. Moore, M.O. Chandler, M. Lockwood, and M. Suguira, Ion energization in upwelling ion events, pp.61-66, in *Ion Acceleration in the Magnetosphere and Ionosphere*, edited by T. Chang, Geophysical Monograph, 38, 1986.
- Yau, A.W., E.G. Shelley, and W.K. Peterson, Accelerated auroral and polar-cap ions: Outflow at DE-1 altitudes, pp. 72-76, in *Ion Acceleration in the Magnetosphere and Ionosphere*, edited by T. Chang, Geophysical Monograph, 38, 1986.

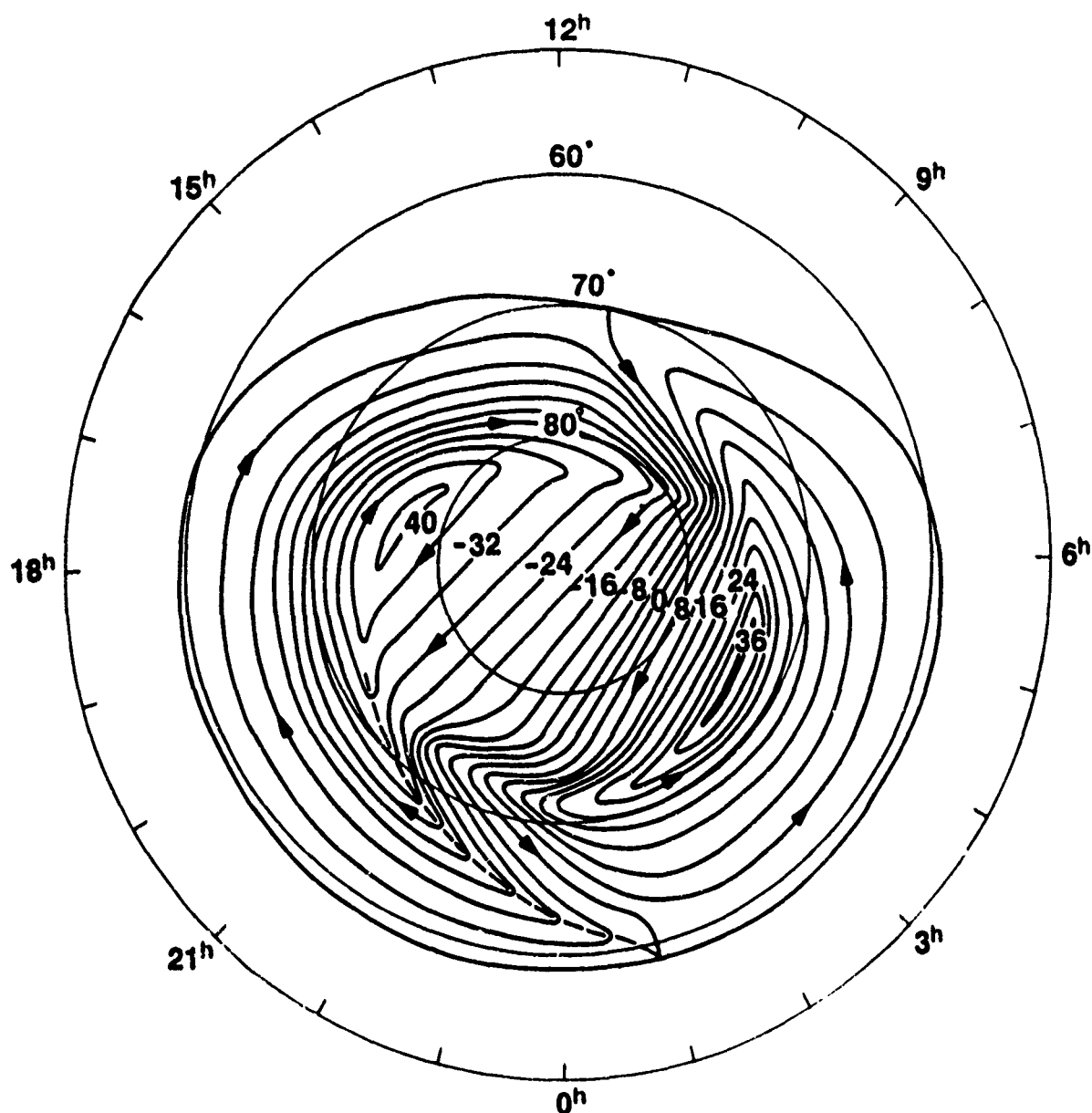


Figure 1. Convection electric field model BC, representing the most typical pattern distribution encountered in the northern hemisphere under +Y IMF conditions and in the southern hemisphere under -Y IMF conditions ($3^+ \leq Kp \leq 4^-$). Fig. 3 of Heppner and Maynard [1987].

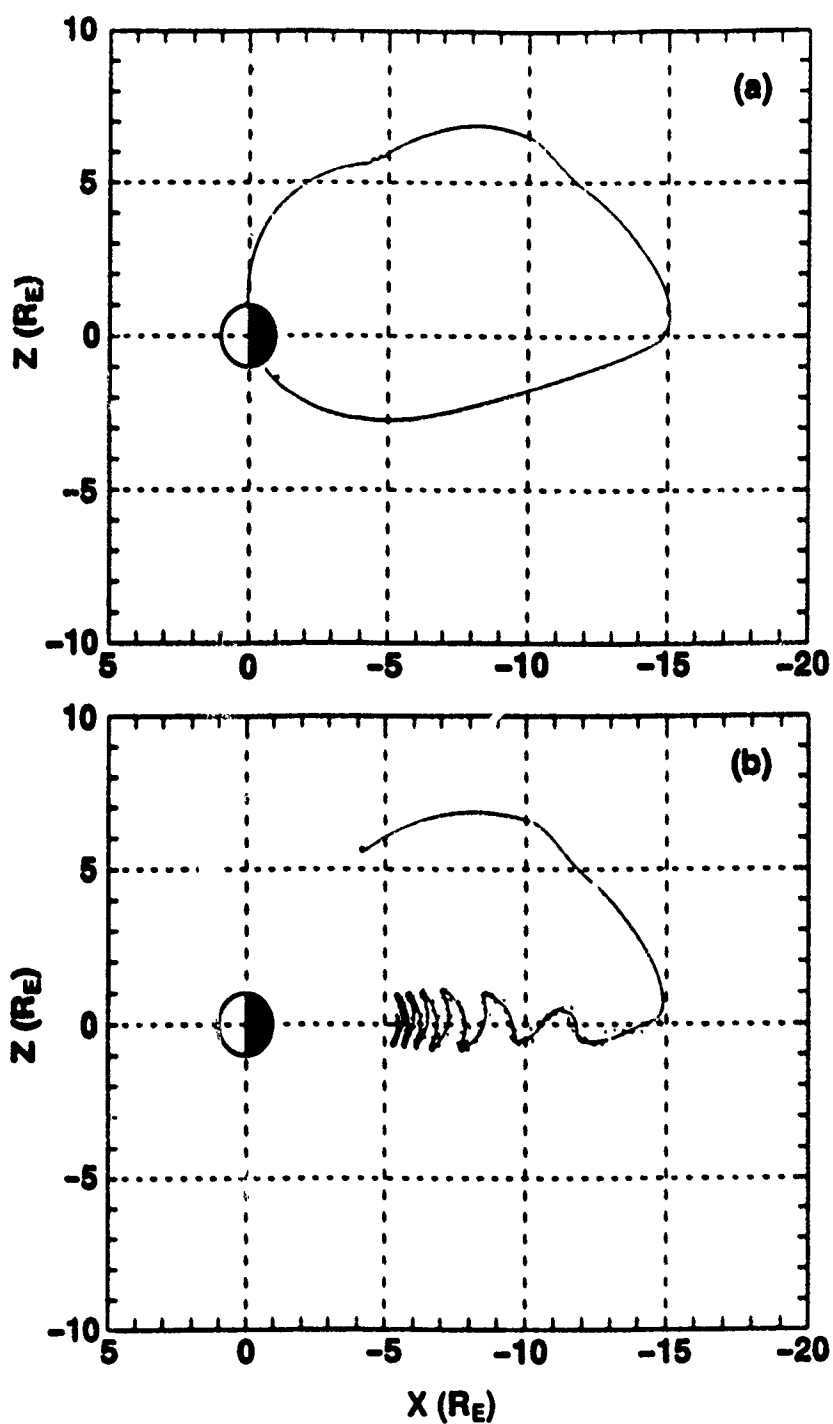


Figure 2. Guiding-center trajectory (panel a.) and outer-magnetosphere portion of full-motion trajectory (panel b.) of O^+ ion projected in X_{GSM}, Z_{GSM} plane. Initial conditions: energy = 10.4 eV, pitch angle = 92.5° ; position = 79° MLAT, 1500 MLT, and 1000 km altitude.

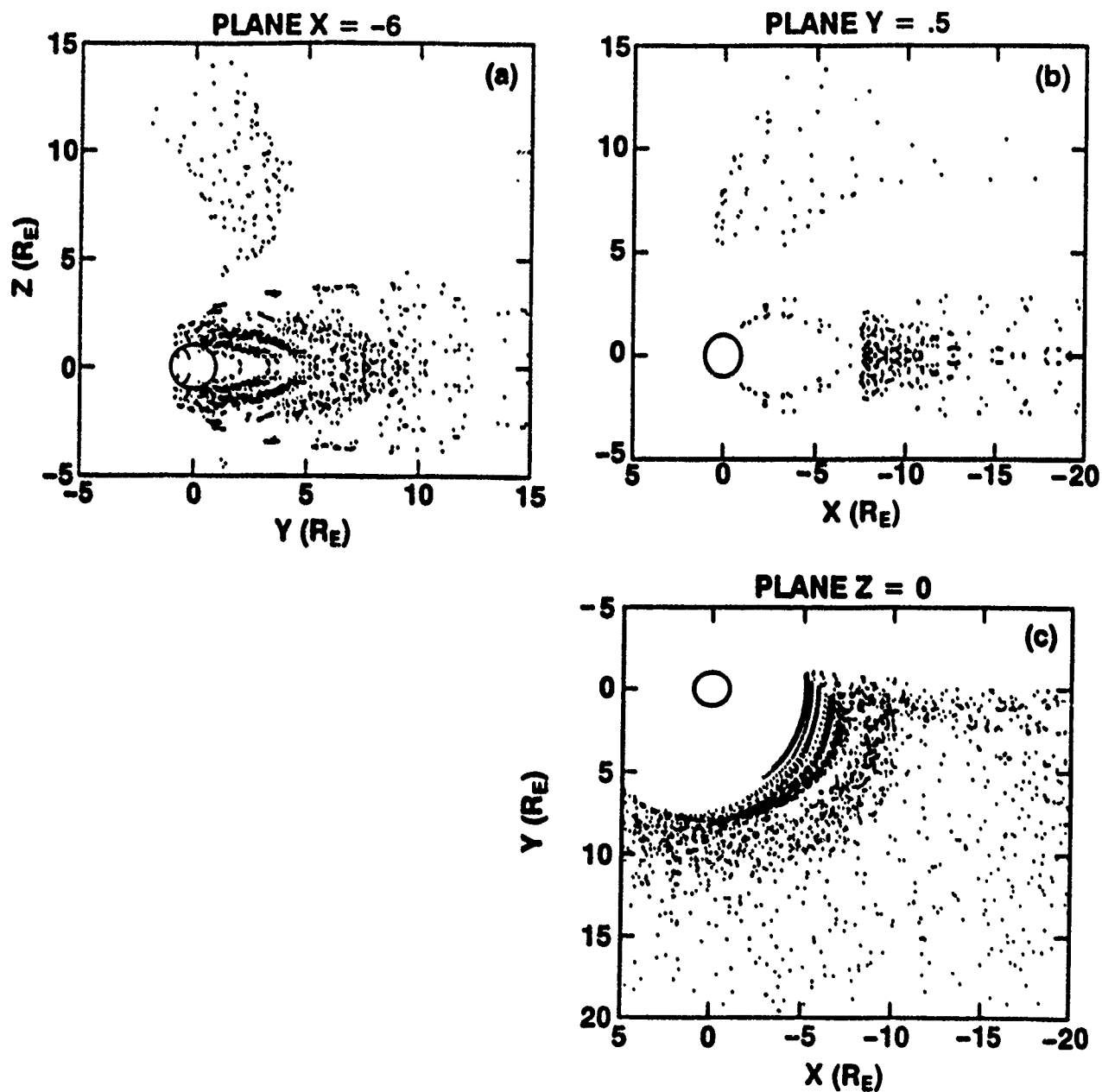


Figure 3. Crossing points of O^+ ions in planes $X_{GSM} = -6$ (panel a.), $Y_{GSM} = 0.5$ (panel b.), and $Z_{GSM} = 0$ (panel c.).

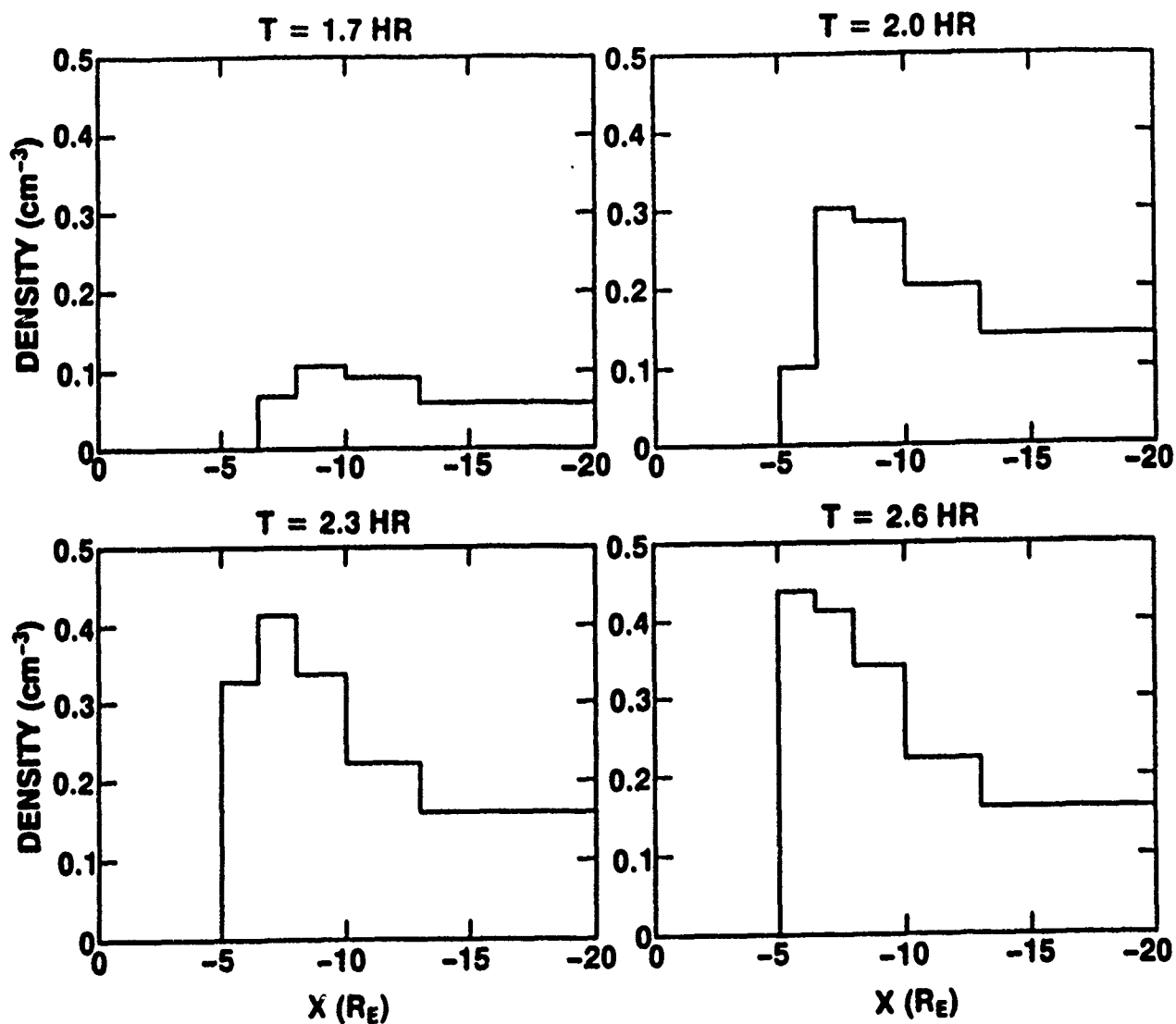


Figure 4. Number density of O^+ ions in interval $0 \leq Y_{GSM} \leq 2$ of center plane versus X_{GSM} at times shown at tops of graphs.

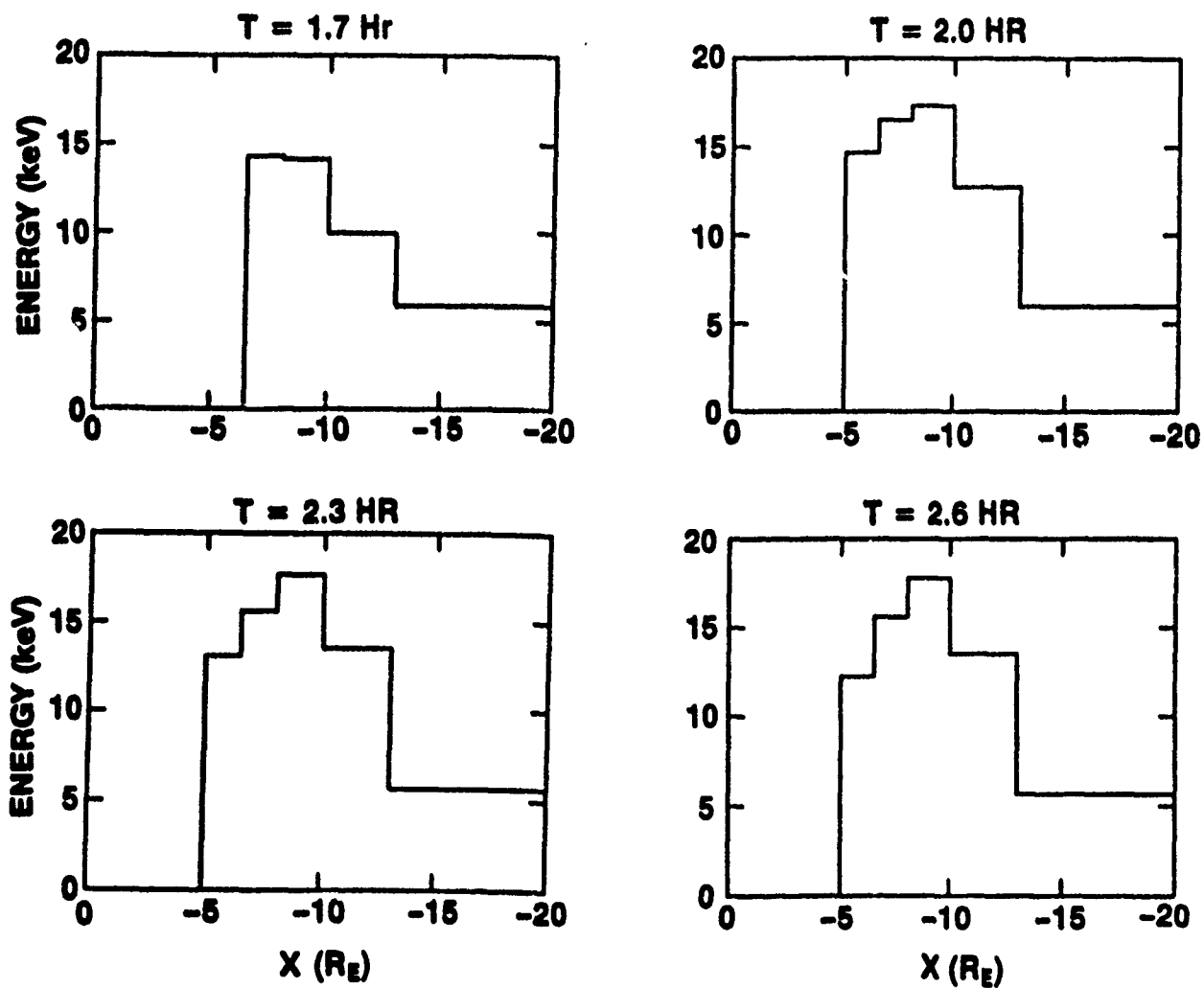


Figure 5. Mean energy of O^+ ions in interval $0 \leq Y_{GSM} \leq 2$ of center plane versus X_{GSM} at times shown at tops of graphs.

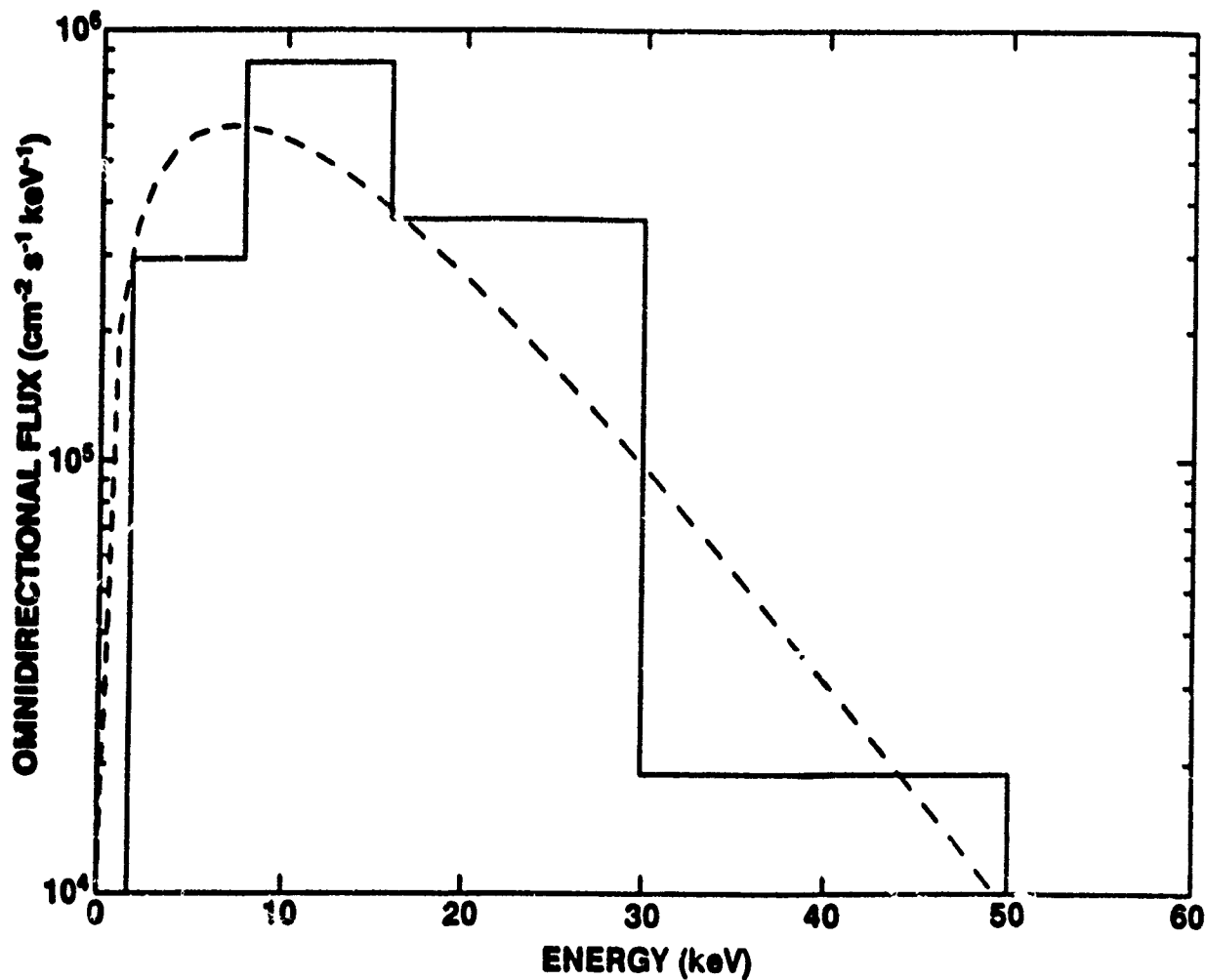


Figure 6. Energy spectrum of O^+ omnidirectional flux in center plane averaged over $-5 \geq X_{GSM} \geq -1^{\circ}$ and $0 \leq Y_{GSM} \leq 2$ at $T = 3.0$ hr. The broken-line curve is the spectrum of a Maxwellian with a "temperature" of 7.3 keV.

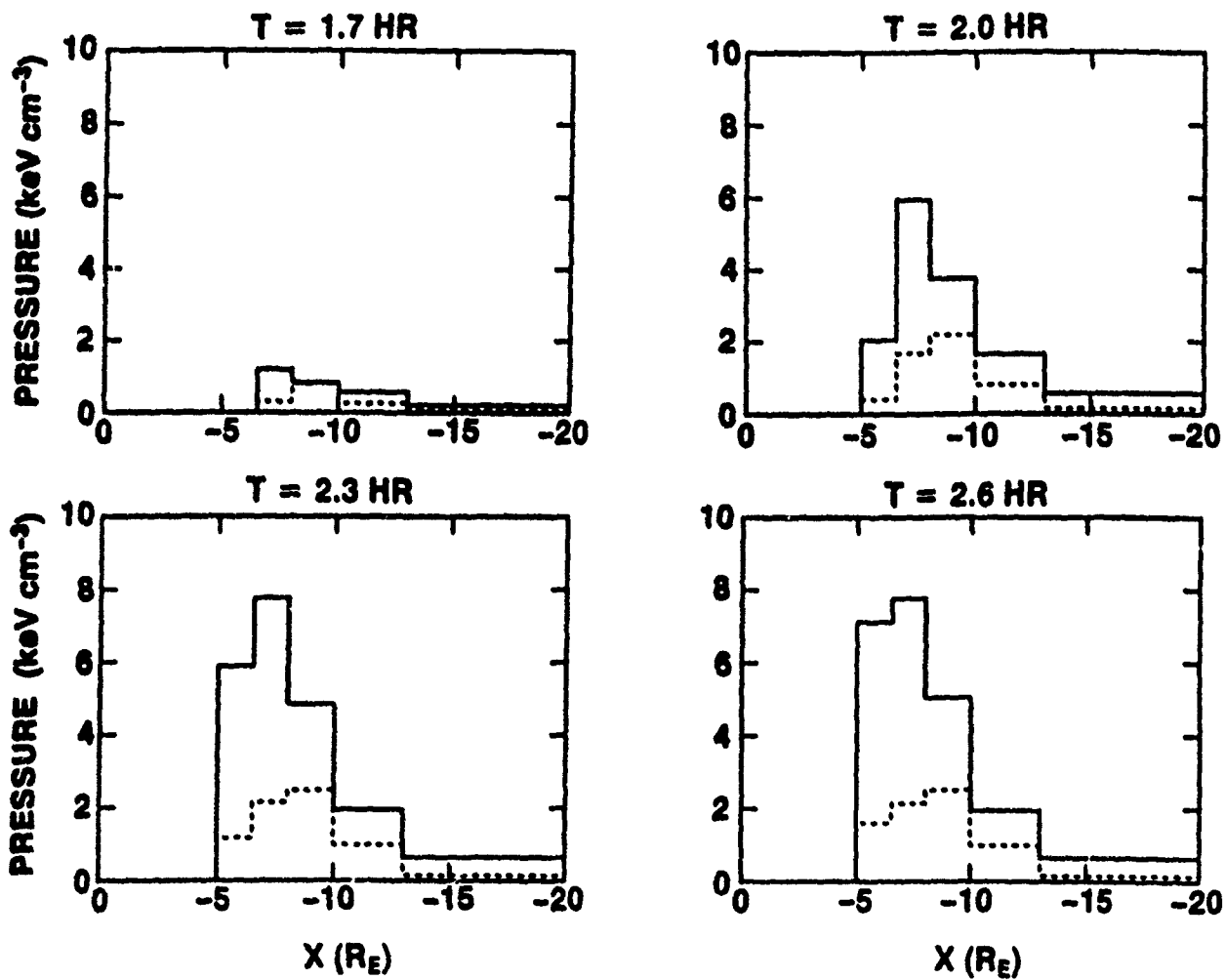


Figure 7. Parallel (solid lines) and perpendicular (broken lines) pressure components of O^+ ions in interval $0 \leq Y_{GSM} \leq 2$ of center plane versus X_{GSM} at times shown at tops of graphs.

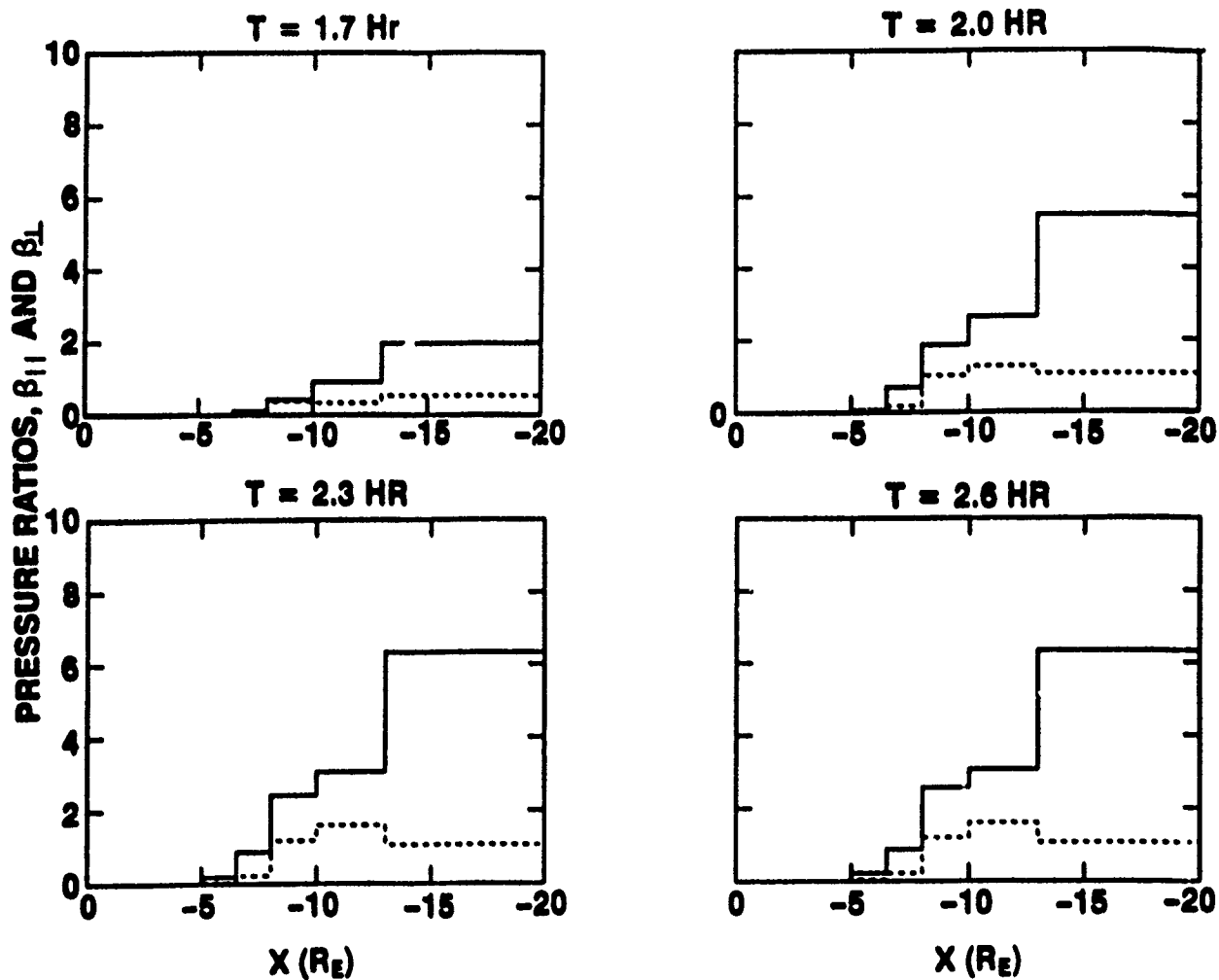


Figure 8. Ratios of O⁺ parallel (solid lines) and perpendicular (broken lines) pressures divided by energy density of magnetic field in interval $0 \leq Y_{GSM} \leq 2$ of center plane versus X_{GSM} at times shown at tops of graphs.